UAB

Universitat Autònoma de Barcelona

Multifunctional N,O-type Carborane-Based Materials: from Molecular Complexes to Three Dimensional Metal-Organic Frameworks

Min Ying Tsang

TESI DOCTORAL

Programa de Doctorat en Química

Director: Dr. José Giner Planas

Tutor: Prof. Agustí Lledós

Department de Química

Facultat de Ciències

2015

Results and Discussion

3.1 N,O-Type Carborane-Based Ligands

A whole series of mono- and disubstituted carborane-based pyridylalcohol ligands (**CB-L** and **CB-(L)₂**, respectively) have been synthesized and fully characterized. In this chapter, the syntheses and characterization of the pyridylalcohol ligands with *ortho-*, *meta-* and *para-*carborane moieties will be described first. In the second part of the chapter, additional crystallographic analyses on the molecular and supramolecular structures for most of the ligands have been conducted. A crystal engineering approach has been used to study the chirality, and homochiral versus heterochiral recognition of these ligands in the solid state.

3.1.1   Syntheses and Characterization

3.1.1.1   Monosubstituted *ortho-*, *meta-* and *para-* Carborane-Based Ligands

The synthetic procedure for the synthesis of monosubstituted *ortho*-carborane-based pyridylalcohol ligands (**oCB-L**) have been previously established in the Laboratory of Inorganic Materials and Catalysis (LMI) in the last few years.[1] An extended synthesis to a new series of monosubstituted *meta-* and *para*-carborane-based pyridylalcohol ligands (**mCB-L** and **pCB-L**) were carried out during this PhD project by using a slightly modified procedure to that previously reported (Scheme 3.1-1).[1]

Scheme 3.1-1: General synthetic scheme of mono-substituted *ortho-*, *meta-* and *para*-carborane pyridylalcohols.
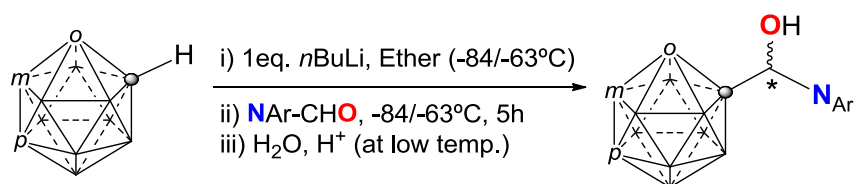
o: ortho- ; m: meta- ; p: para- ; $C_2B_{10}H_{10}$; ● = CH; rest of vertexs = BH
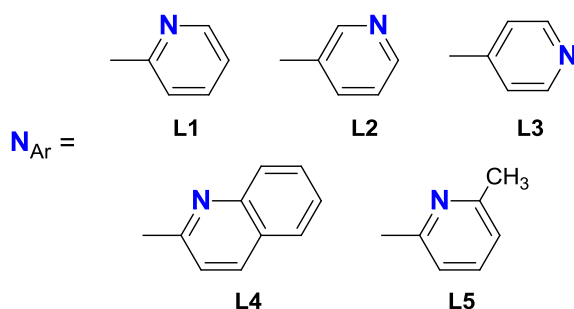
The monosubstitution reaction is initiated by the commonly used lithiation method at one of the carbon atoms of the cluster, followed by the nucleophilic addition to an electrophile, in this case, pyridylaldehydes. As mentioned in the introduction, this reaction is not trivial due to the tendency of the monolithiated *o*-carborane to disproportionate to *o*-carborane and its dianion.[1d] Several methodologies were applied in the LMI group previously and the optimal condition for the monosubstitution of *o*-carborane was found by using ethereal solvents as media and keeping the

reaction temperature low during the whole reaction time(< -70 ^{o}C) to avoid reversible reaction.[1d,2] This reaction procedure has been followed, although with slight modifications, during this PhD work for the synthesis of new monosubstituted ligands of *mCB* and *pCB*. Low yields were often obtained initially for the monosubstitutions of *mCB* and *pCB* at temperatures lower than -70 ^{o}C. It was reasoned that as the C-H vertex of *mCB* and *pCB* are relatively less acidic than that for *oCB* (details in Chapter 1.1), a very low reaction temperature might slow down or prevent the deprotonation reaction and the following reaction with the electrophile. Indeed, high yields were obtained by increasing the reaction temperature that was found to be aptimal at -63 ^{o}C for *mCB* and *pCB* monosubstitution reactions. Therefore, a range of monosubstituted carborane based ligands with different pyridylalcohol substituents have been obtained in 63 to 73 % (Table 3.1-1).

Table 3.1-1: Summary of mono-substituted carborane based ligands

*o*CB[a]	*m*CB [b]	*p*CB [b]
L1, L2, L3, L4, L5	**L1, L2, L3**	**L1**
a: ligands reported previously [1]; b: ligands synthesized during this PhD work		

As previously mentioned, different than organic compounds such as phenyl ring, one of the advantages of carborane cluster is the tuneable feature of the C-H or B-H vertexes without varying the bulkiness, which provides an alternative platform to study the influence of the electronic properties of the corresponding ligand excluding the steric hindrance effect.[3] Hence, for comparison purposes, two iodinated *meta*-carborane-based ligands were synthesized by substituting the hydride (H$^-$) at B(9) or/and B(10) positionby iodide (I$^-$). The iodination reaction of the B-H vertexes was performed under strong acidic conditions.[3c] The desired iodinated *mCB*-ligands were then obtained by litiation and nucleophlic addition of the appropriate pyridylaldehyde (Scheme 3.1-2).

Scheme 3.1-2: Synthetic scheme of iodinated monosubstituted *meta*- carborane 2-pyridylalcohol **I-*m*CB-L1** and **I$_2$-*m*CB-L1**.
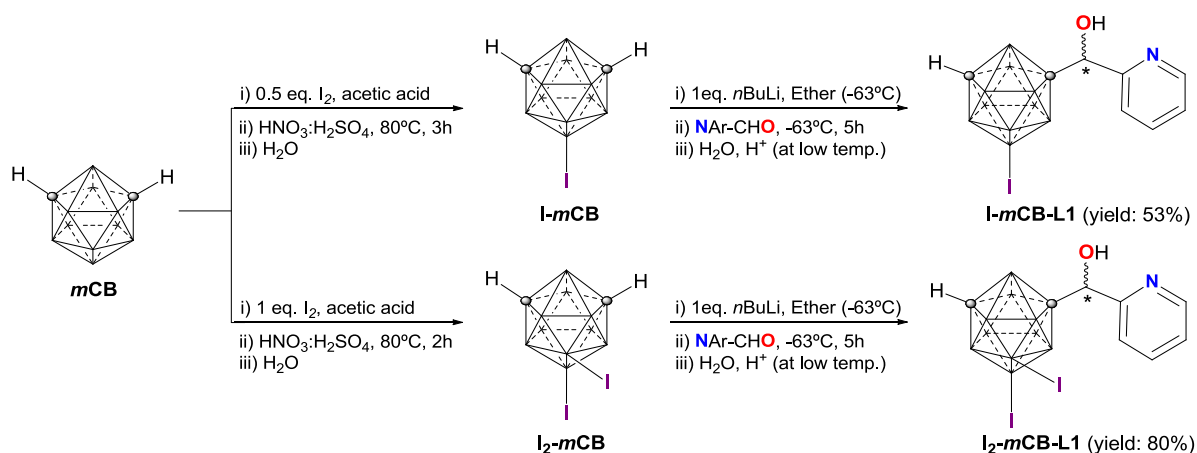
$C_2B_{10}H_{10}$; ◉ = CH; rest of vertexs = BH

All compounds (**oCB-L, mCB-L and pCB-L**) are fully characterized by ATR-FTIR, NMR (^{1}H, ^{11}B, ^{13}C), elemental analysis, MALDI-TOF-MS and XRD (see the following section 3.1.2.1). Characterization for a selected example, **I$_2$-mCB-L1**, is shown bellow.

Infrared spectroscopy is a very useful technique to identify the presence of boron species containing B-H vertex such as carborane since the B-H stretching in the spectrum is located at around 2600 – 2400 cm^{-1}. As shown in Figure 3.1-1, the broad band at 2542 cm^{-1} corresponds to the B-H stretching in the *meta*-carborane cluster **I$_2$-mCB-L1**.

Figure 3.1-1: Infrared spectrum of **I$_2$-mCB-L1**. Selected O-H stretching, C-H stretching and the B-H stretching are indicated.

MALDI-TOF-MS has been used to measure the molecular ions of the ligands by ionization. Besides, a unique isotopic pattern can be obtained from the corresponding spectrum. Therefore, the chemical formula of the ligand can be confirmed by comparison to the simulated pattern. Spectrum of **I$_2$-mCB-L1** and the simulated patterns are shown in Figure 3.1-2. The isotope distribution and the molecular weight fit to the simulation as [**I$_2$-mCB-L1**+H]$^+$.
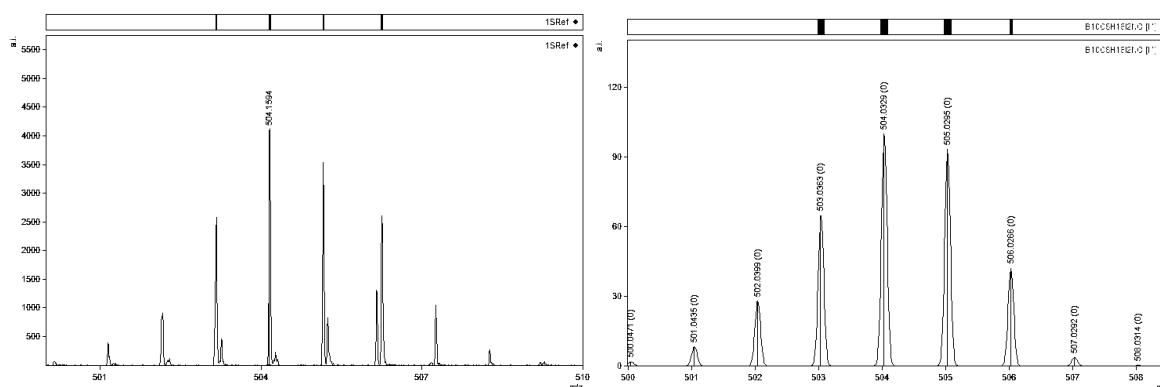

Figure 3.1-2: MALDI-TOF spectrum of **I$_2$-mCB-L1**(left), and the corresponding isotope simulation pattern (right).

NMR (^{1}H, ^{11}B{^{1}H}, ^{11}B and ^{13}C) spectra of the **I$_2$-mCB-L1** are shown in Figure 3.1-3 as a general example for the chemical shifts of the monosubstituted ligands. The proton resonances for this compound correlated well with the other related carboranylalcohols.[1] As can be seen in Figure 3.1-3,

^{1}H and ^{13}C NMR spectra show characteristic peaks for the cage-carbon C-H vertex of the carborane cluster, pyridine ring and CHOH moiety. In the[1]H NMR spectrum, compound **I₂-mCB-L1** shows a broad resonance for the *Cc*H (Cc = cage carbon) proton at δ 4.0, which is in agreement with the monosubstitution of the cage. Proton resonances for the O*H* and *CH*OH groups in **I₂-mCB-L1** appear as two doublets with coupling constant *J* = 6.0 Hz at δ 5.90 and 5.10, respectively. In this type of compounds, proton resonances for the O*H* and *CH*OH appear always in the same range and have been unambiguously confirmed previously.[1] The high chemical shift for the OH signal in this and all the other related alcohols is due to a solution persistent intra- and/or inter-molecular OH···A hydrogen bond (A = Nitrogen or Oxygen).
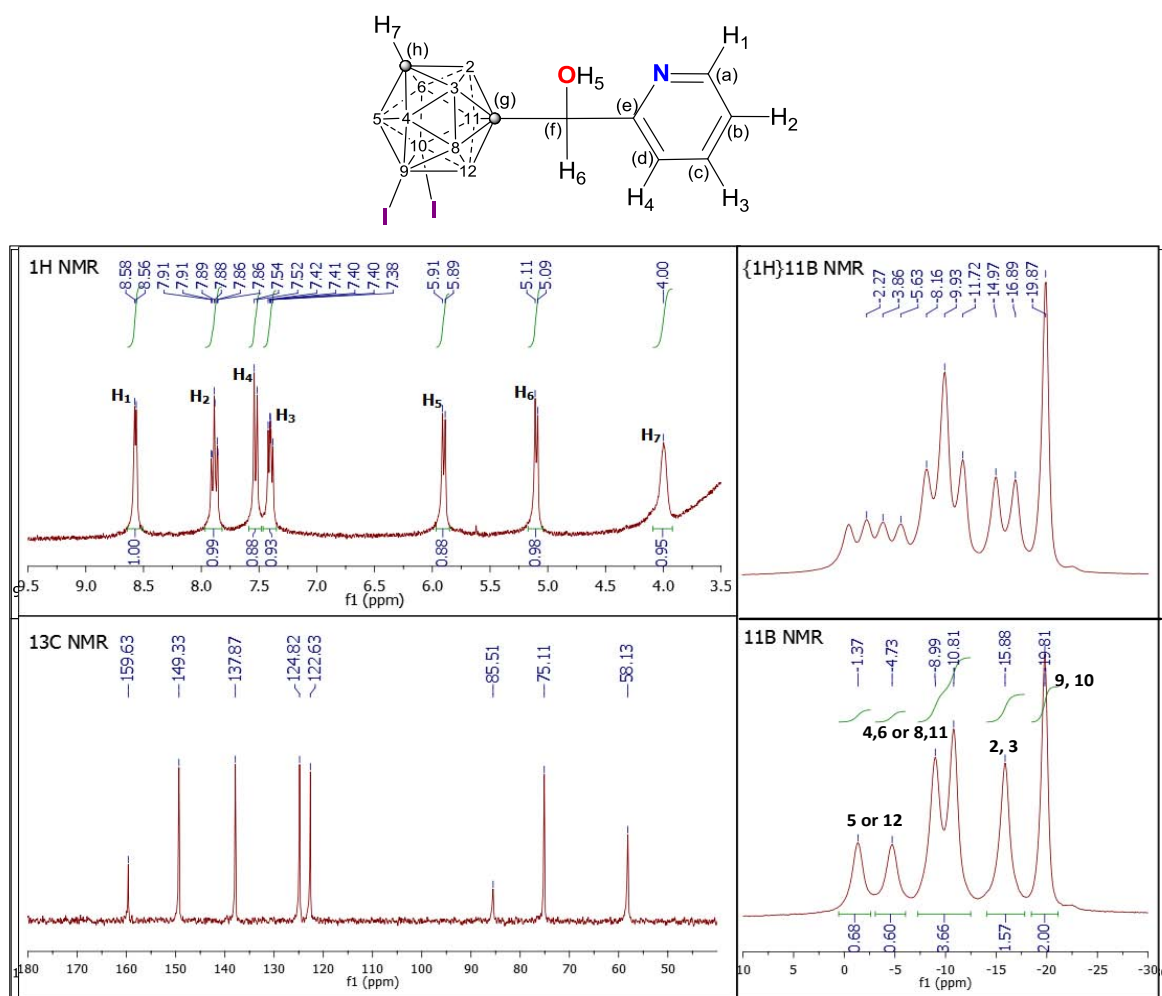

Figure 3.1-3: NMR (^{1}H, [11]B{[1]H}, [11]B and ^{13}C) sepctra of **I₂-mCB-L1** in Ac-D₆. Integrations and chemical shifts are shown.

^{11}B{^{1}H} NMR spectra for these series of compounds are consistent with a *closo*-icosahedral geometry for the boron cage. ^{11}B{^{1}H} NMR spectrum of the selected example **I₂-mCB-L1** shows six resonances in the range of δ -1.4 to -19.8 for ten boron atoms in a 1:1:2:2:2 ratio (Figure 3.1-3). The fully coupled ^{11}B NMR spectrum for this compound shows a singlet at δ -19.8 for the B-I vertex whereas the rest of the boron atoms appear as doublets due to [11]B-^{1}H coupling (170.4 to 184.8 Hz). Complete assignment

of all BH signals can be done by comparison with related carborane derivatives.[1] ^{11}B chemical shifts of basic borane skeletons do not correspond generally to the electron densities of individual vertexes as in organic compounds, but rather to various effects (*e.g.* antipodal effect and neighbour effect) influencing their electron anisotropy.[3d] Thus, the boron atoms that are closest to the carbon atoms are most shielded than those far away from the carbons. Addition of substituents changes the symmetry and electron density with the corresponding changes in chemical shifts. Following all these, we can tentatively assign all BH signals as shown in Figure 3.1-3.[4]

It is important to note that all the ligands in this thesis are chiral due to the presence of asymmetric carbon centres. Only one asymmetric carbon centre is present in these mono-substituted carborane-based ligands, and so two possible enantiomers can be obtained, *R* and *S* (Figure 3.1-4).
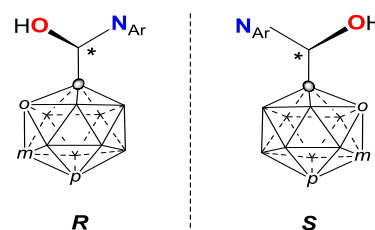
Figure 3.1-4: Enantiomers of carborane-based ligands and their absolute configurations.

3.1.1.2 Disubstituted *ortho*- and *meta*-Carborane-Based Ligands

Disubstituted *ortho*- and *meta*-carborane-based ligands (**oCB-(L)₂** and **mCB-(L)₂**) have been synthesized by following a similar synthetic procedure to that of the monosubstituted ligands (Scheme 3.1-3).

Scheme 3.1-3: Synthetic scheme for the di-substituted *ortho*- and *meta*- carborane and pyridylalcohols.
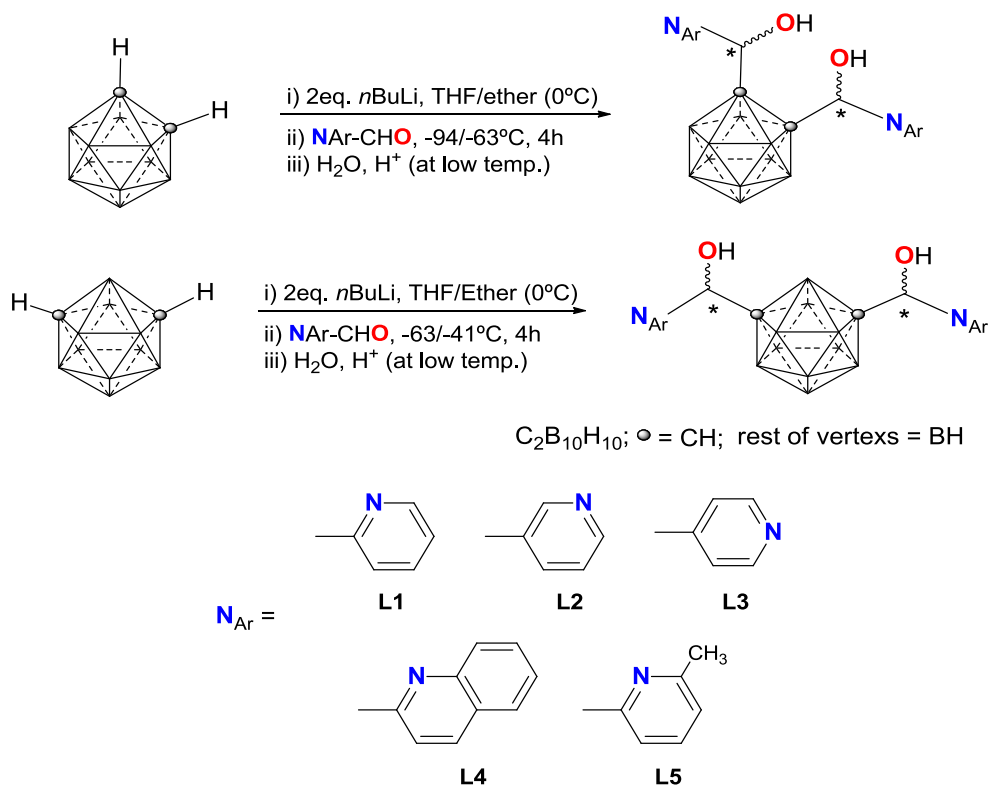
In this case, two equivalents of *n*-BuLi are used to generate di-lithiated anions, followed by addition of 2 equivalents of corresponding aldehyde to give the desired disubstituted ligands. Lithiation has been done at 0 ^{o}C to facilitate the complete formation of di-lithiated salts, although the nucleophilic additions have been done at low temperatures, as in case of the monosubstitutions explained in the previous section. Similarly, the conversion and final yields are affected by the temperature of the reaction media. In agreement with the monosubstitution reactions (previous section), it was found that the disubstitution of *meta*-carborane was achieved in higher yields at higher temperatures than the related *ortho*-carborane ones. For example, it was found that for obtaining yields higher than 80%, a temperature of -94 ^{o}C needed to be used for the **oCB-(L2)$_2$**, whereas a temperature of -63 ^{o}C is required in case of the **mCB-(L2)$_2$**. It was also found that a higher temperature (-41 ^{o}C) had to be used for a different isomer of the later **mCB-(L3)$_2$**. Table 3.1-2 summarized the family of disubstitution ligands that have been synthesized.

Table 3.1-2: Summary of disubstituted carborane based ligands

*o*CB	*m*CB [b]
(L1)$_2$ [a,b], (L2)$_2$ [b], (L3)$_2$ [b], (L4)$_2$ [a,b], (L5)$_2$ [b]	(L1)$_2$, (L2)$_2$, (L3)$_2$, (L5)$_2$
a: ligands synthesized in the group previously; b: ligands synthesized during this PhD work	

Additionally, a B-methylated *ortho*-carborane-based ligand by substituting the hydride (H$^-$) to methyl (CH$_3$) at B(9) position and a B-methylated *meta*-carborane-based ligand at B(9) and B(10) positions were synthesized for comparison purposes. The methylation reaction of the B-I vertexes was performed by a modified Grignard reaction from the literature.[5] The disubstituted ligands were then prepared by dilithiation and addition of the corresponding pyridylaldehydes (Scheme 3.1-4).

Scheme 3.1-4: Synthetic procedure of mono-methylated di-substituted *ortho*- carborane 3-pyridylalcohol ligand **Me-oCB-(L2)$_2$** (top) anddi-methylated di-substituted *meta*- carborane 4-pyridylalcohol ligand **Me$_2$-mCB-(L3)$_2$** (bottom).

$C_2B_{10}H_{10}$; ○ = CH; rest of vertexs = BH
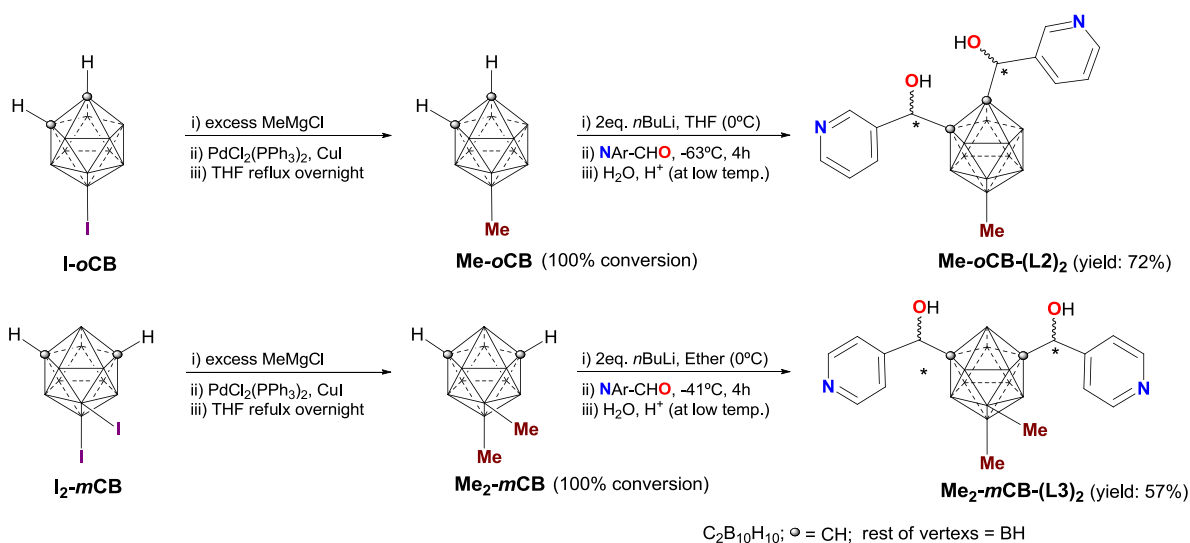
All disubstituted compounds have been fully characterized by ATR-FTIR, NMR (^{1}H, ^{11}B{^{1}H}, ^{11}B, ^{13}C), elemental analysis, MALDI-TOF-MS and XRD in some of them (see section 3.1.2.2). The characterization details for a selected example **_o_CB-(L1)$_2$** is shown for demonstration purposes. Similar to the monosubstituted ligands, Infrared spectrum shows the B-H stretching band at 2564 cm^{-1} (Figure 3.1-5).

Figure 3.1-5: Infrared spectrum of **_o_CB-(L1)$_2$**. Selected O-H stretching and the B-H stretching are indicated.

The MALDI-TOF mass spectrum of **_o_CB-(L1)$_2$** and the simulated patterns are shown in Figure 3.1-6. As it can be seen, a good agreement is found between the experimental and the calculated spectra.
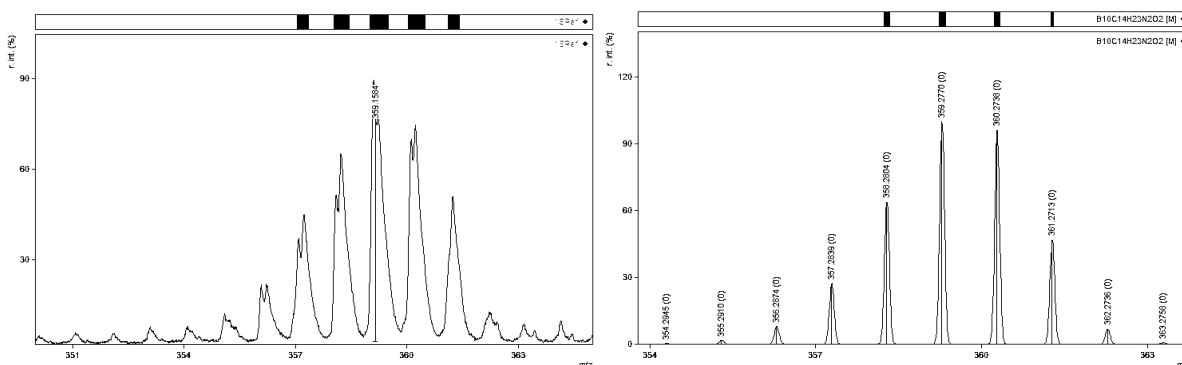

Figure 3.1-6: MALDI-TOF spectrum of **_o_CB-(L1)$_2$** (left), and the corresponding isotope simulation pattern (right).

NMR (^{1}H, ^{11}B and ^{11}B{^{1}H}) spectra of the **_o_CB-(L1)$_2$** are shown as a general example for the chemical shifts of the disubstituted ligands. The peaks assignment for the chemical shifts in these ligands is similar to the monosubstituted ligands. However a higher number of signals are observed in the ^{1}H NMR for the disubstituted ligands, which is due to the presence of diastereoisomers (*syn-* and *anti-*).

Since all the ligands contain two chiral carbon centres that can adopt the *R* or *S* configuration, two diastereoisomers: meso compound (*RS*; OH groups in a *syn*-orientation; non chiral) and racemic compound (mixture of *SS* and *RR*; OH groups in an *anti*-orientation, chiral) are formed (Scheme 3.1-5).

Scheme 3.1-5: Stereoisomers for disubstituted compounds for both *ortho-* and *meta-* carborane moieties.

RR **SS**	**SR**
Racemate	Meso

N_{Ar} = Aromatic Ring
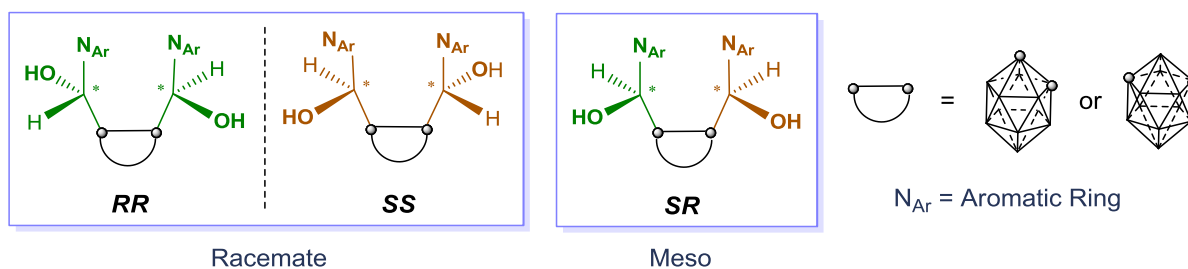
^{1}H NMR spectra for the diastereomers mixture shows *anti-* to *syn-* ratio of 1 : 0.65. Although there is no direct proof for the stereo-selectivity of the reaction, the lower ratio of the *syn*-isomer formation is most probably because of the higher steric interaction of the OH groups. Due to the different solubility of the diasteroisomers, separation by preparative TLC is possible in some cases. The assignment of the *syn-* and *anti*-isomer signals in the mixture is confirmed by the ^{1}H NMR spectra of the separated diasteroisomers (Figure 3.1-7, left) and their corresponding single crystal XRD structures (section 3.1.2.2). Moreover, in ^{11}B NMR spectra, two broad signals in 2:8 ratios are observed probably due to the combination of fluxional behaviour and extensive overlapping of the both diastereoisomer signals (Figure 3.1-7, right).
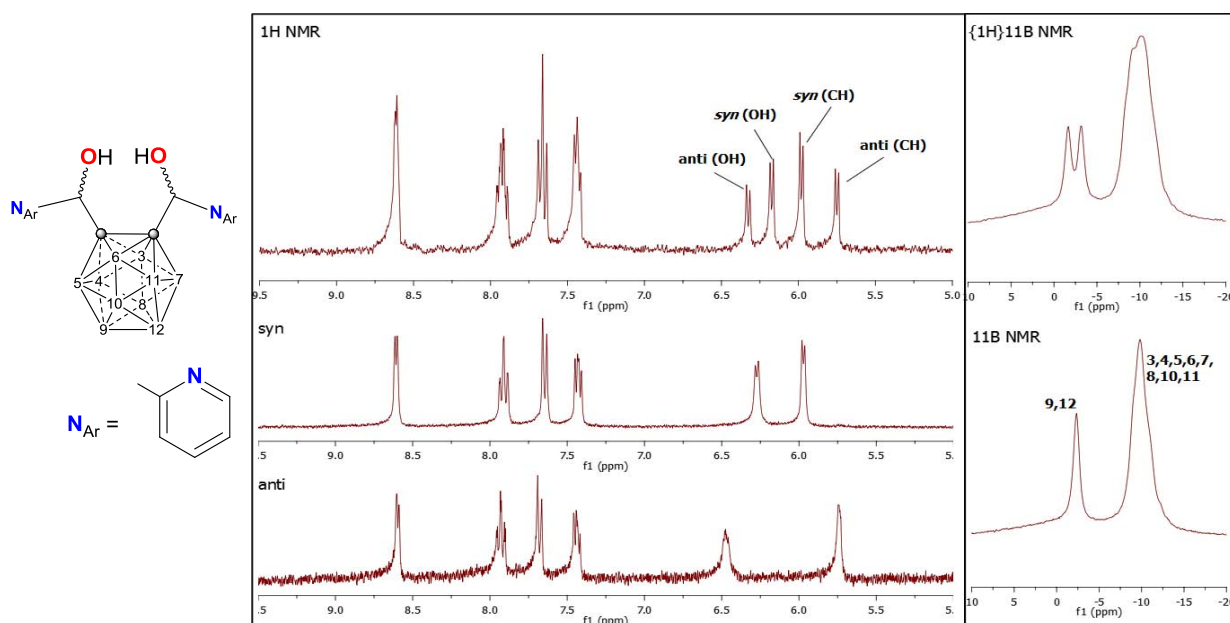

Figure 3.1-7: ^{1}HNMR (left) and [11]B {[1]H} and [11]B (right) spectra of ***o*CB-(L1)₂** in Ac-D₆. In ^{1}HNMR spectra, upper spectrum is the mixture of *syn-* and *anti-* diastereoisomers. The middle and the lower spectra correspond to *syn*-isomer and a*nti*-isomer respectively.

As it has been shown above (Figure 3.1-7), the diastereoisomers of ***o*CB-(L)₂** can be observed in ^{1}H NMR spectra. Differently, this is not the case in the related ***m*CB-(L)₂** derivatives as it shown in Figure 3.1-8. This can be explained by the restricted rotation of the pyridylalcohol arms from the ***o*CB-(L)₂** due to the steric hindrance of the pyridylalcohols. Free rotation of the pyridylalcohol arms from ***m*CB-(L)₂** is possible in the *meta*-carborane derivatives due to the larger distance between the two

cluster carbons as compared with those in the *ortho*-carborane derivatives. Selected ^{1}H NMR spectra of ***o*CB-(L1)₂** and ***m*CB-(L1)₂** are shown (Figure 3.1-8).
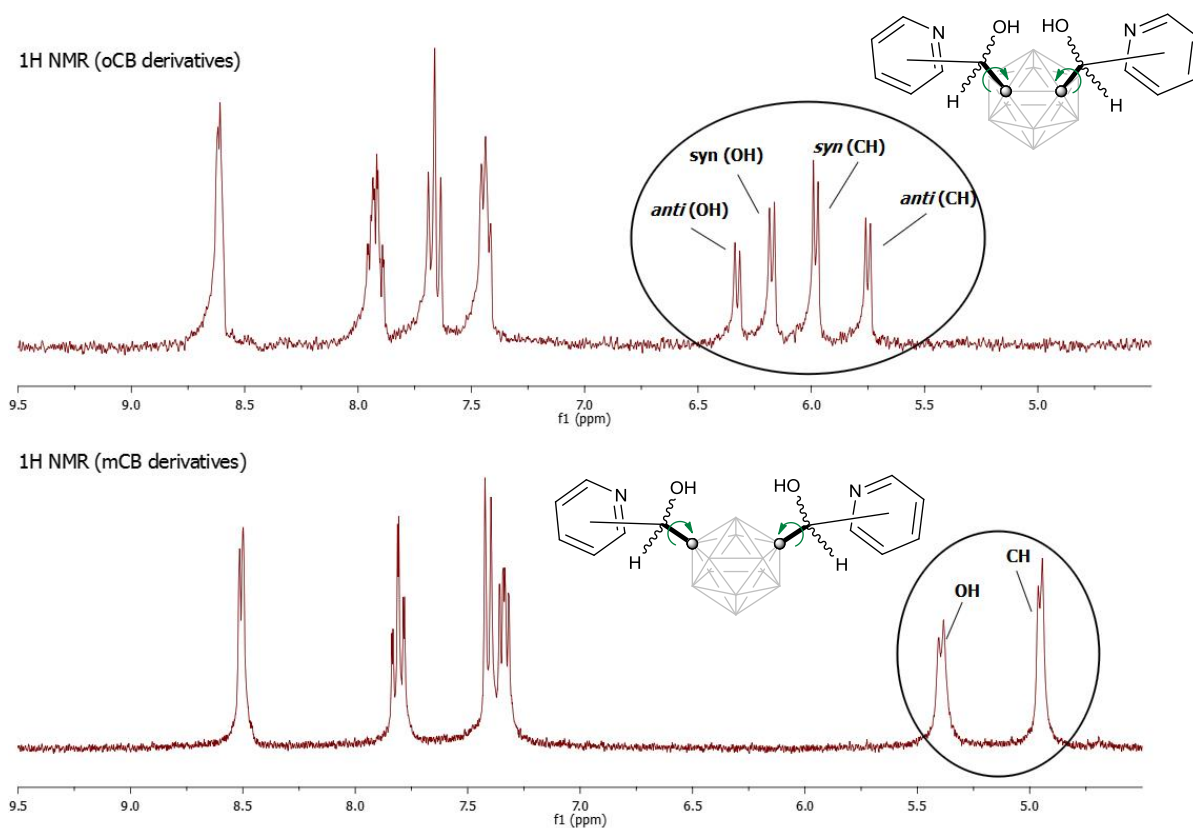

Figure 3.1-8: ^{1}H NMR sepctra of ***o*CB-(L1)₂**(top) and ***m*CB-(L1)₂**(bottom) in Ac-D$_6$.

In summary, a whole series of mono- and disubstituted carborane-based pyridylalcohol ligands have been successfully synthesized in high yields, by one pot reaction and have been completely characterized. The high stabilities of the carborane moieties and the expected coordination abilities of these N,O-type donor compounds make them attractive candidates as ligands for further studies to develop multifunctional materials. The later will be extensively described in Chapter 3.2 – 3.5. The remaining part of the present chapter will deal with the analysis of the molecular and supramolecular structures for most of the mono- and disubstituted compounds.

3.1.2   Crystal Engineering: Molecular and Supramolecular Studies

3.1.2.1   Molecular versus Supramolecular Chirality of Monosubstituted Carborane-Based 2-Pyridylalcohol –A Case Study

In supramolecular chemistry and crystal engineering, one of the key researches is the design and molecular self-assembly of molecules by using hydrogen bonds (HBs).[6,7] However, the understanding of the self-assembly mechanism remains as one of the major challenges for design and synthetically control of the self-assemble construction. The self-assembly of the biological molecules are often inspiring, especially the influence of the chirality from molecular level to two- or three-dimensional motifs.[8] One of the example is the chiral α-amino acids and their supramolecular handedness helical structures.[6,7,9] Recently, Miyata and co-workers developed a method (supramolecular-tilt-chrirality, STC) to define the handedness of 2-fold helical assemblies. Using this method, Miyata found a possible correlation between the handedness of chiral amines and the handedness of the 2_1-helical charge-assisted HB networks.[10] The findings are schematically represented in Figure 3.1-9. Four diastereomers can be formed (*R*- or *S*-^{sup}P, ^{sup}P denotes supramolecular right-handed helix; *R*- or *S*-^{sup}M, ^{sup}M denotes supramolecular left-handed helix) when self-assembled to form helical supramolecular structures. It is the first time to show a possible connection from the molecular chirality (MC) to the supramolecular chirality (SMC) by relatively strong non-covalent interactions. However,
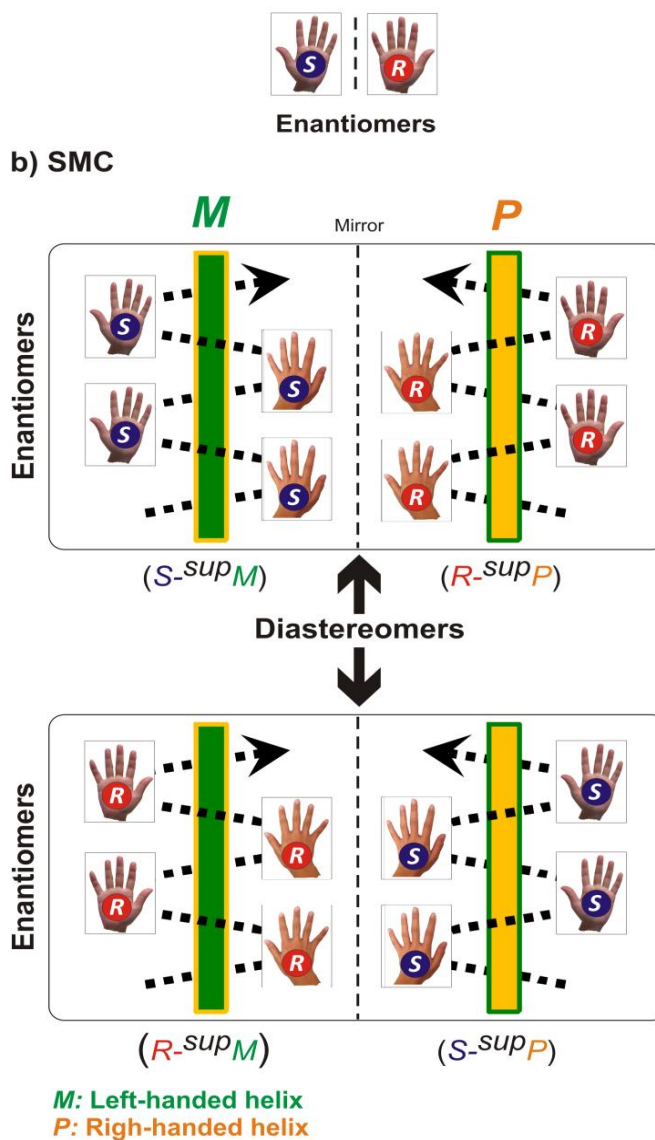

Figure 3.1-9: Relational diagram between a) molecular chirality (*R* or *S*) and b) supramolecular chirality (*M* or *P*) of 2_1-helical hydrogen-bonded networks. Dashed lines represent intermolecular interactions such as *e.g.*, hydrogen bonding. (Modified from reference 10) Copyright 2013 Nature Publishing Group.

it is still a challenge for those systems with weaker intermolecular interactions or the extension to other chiral molecular compounds.

O-H···N hydrogen bonded homochiral chains are found to be formed in the racemic *o*-carborane 2-pyridylalcohol ligands (Figure 3.1-10).[1d] In order to get more insight into the impact of carborane isomers to the solid structures and the relations of the MC and SMC, a complete series of racemic and the corresponding enantiopure chiral monosubstituted carborane-based 2-pyridylalcohols (Scheme 3.1-6)
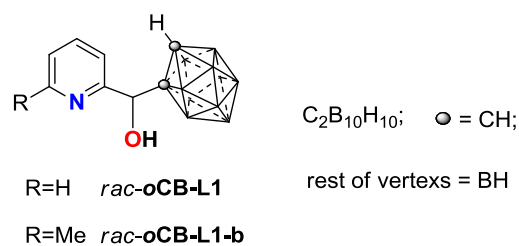
$C_2B_{10}H_{10}$;   ● = CH;

rest of vertexs = BH

R=H   *rac-oCB-L1*

R=Me   *rac-oCB-L1-b*

Figure 3.1-10: Previously characterized carboranyl alcohols. [1d]

have been studied. The structures of those ligands have been resolved, and the correlation between the handedness of 2_1-helical HB networks and the torsion angles in the molecules will be shown in this section.

Scheme 3.1-6: Graphical representation of the molecular structures for the carborane isomers analyzed in this work. The rotamer found in each X-ray structure is illustrated.

$C_2B_{10}H_{10}$;   ● = CH;

rest of vertexs = BH
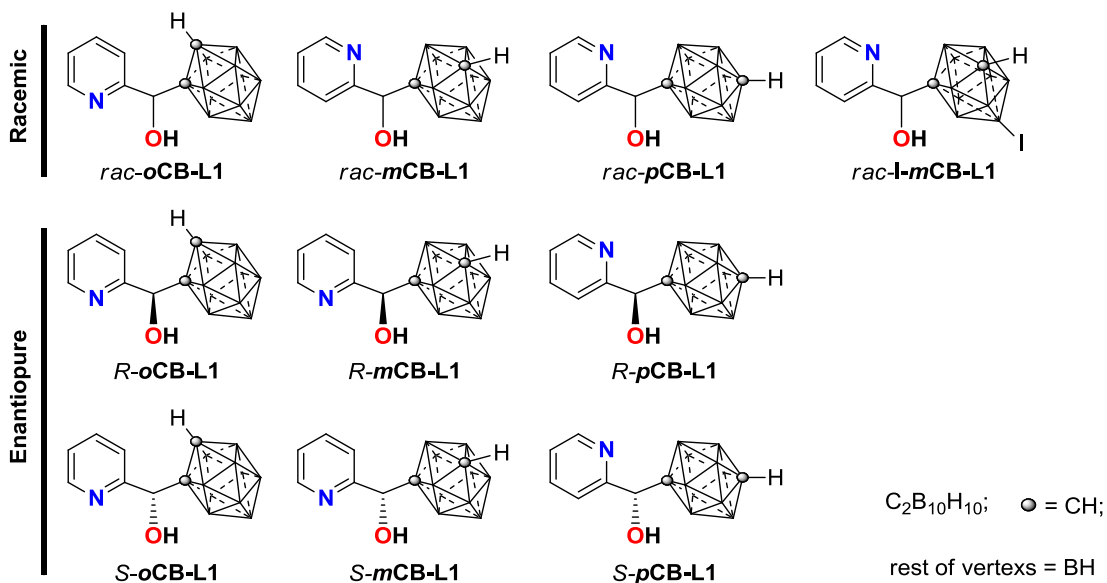
All the structures were confirmed by single-crystal XRD and the location of the OH hydrogen positions are clear from the examination of different map. In addition, powder X-ray diffraction (PXRD) pattern of each compound fits to the calculated patterns from the single-crystal X-ray data and therefore confirms the phase purity and the absence of the concomitant polymorphism.

Molecular Structures Conformations

Rotation of the pyridine rings through the (H)(OH)C-C(pyridine) bond allows two main rotamers in the solid state: the pyridine nitrogen *syn-clinal* (*-sc*~ -40° and *+sc*~ +40°) to the alcohol oxygen, or

anti-periplanar (-*app*~> -150° and +*app*~> +150°) to it (Scheme 3.1-7). In the following discussion, *syn-* or *anti-* will be used to refer to the *syn-clinal* or *anti-periplanar*, respectively.

Scheme 3.1-7: Newman projections for rotamers found in the solid structures for chiral 2-pyridylalcohols **CB-L1**. The chirality at the carbon is indicated.
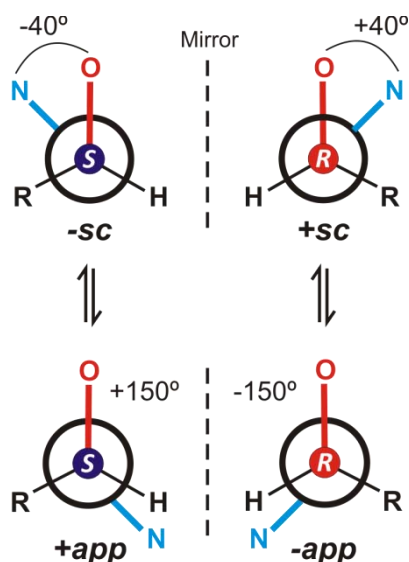
The torsion angles of all enantiomers in the racemic and enantiopure structures were analyzed and summarized in Table 3.1-3. All the *o*-carborane pyridylalcohols (*o***CB-L1**) crystallize in *syn*-conformations and the *p*-carborane pyridylalcohols (*p***CB-L1**) crystallize in *anti*-conformations. However, *m*-carborane pyridylalcohols crystallize in *anti*-conformations for the racemic structures (*rac-m***CB-L1** and *rac-***I***-m***CB-L1**) but in *syn*-conformations for the enantiopure structures (*R-m***CB-L1** and *S-m***CB-L1**). The presence of different rotamers of *m*-carborane pyridylalcohols (*m***CB-L1**) indicates the small differences of their lattice energies, which is confirmed by the preliminary gas phase calculations for *rac-o***CB-L1** and *rac-m***CB-L1** (the *syn*- conformers are more stable than the *anti*- conformers due to the intramolecular O-H···N HBs, but vice versa for the corresponding deprotonated molecules). The different conformations can be related to their relative stability during crystallization due to the intermolecular hydrogen bonding between the compounds and the solvent molecules. Besides, as mentioned previously, the acidity of the carborane decreases in the order of *o*- to *m*- to *p*-carborane moieties (Chapter 1.1). Therefore, the possible influence of the acidity of the OH group from the intra- versus intermolecular hydrogen bonding to the conformations cannot be ruled out.

Table 3.1-3: Selected molecular, supramolecular and crystal parameters for racemic and/or enantiopure carborane-based 2-pyridylalcohols **CB-L1** from Scheme 3.1-7.

Compounds	SG^a	Z'	OCCN torsion (º)		SMC^b	P (Å)^c	ON (Å)	OHN (º)
			R-isomer	*S*-isomer				
*rac-o***CB-L1**^{d}	P2$_1$/c	1	+39.73	-	R-^{sup}P	6.703	2.748	167.49

Compound	SG[a]				Chirality[b]	Pitch[c]		
			-	−39.73	S-^{sup}M			
R- **oCB-L1**	$C2$	1	+41.72	-	R-^{sup}P	6.696	2.751	166.23
S- **oCB-L1**	$C2$	1	-	−42.89	S-^{sup}M	6.681	2.744	164.51
rac-**mCB-L1**	$Pna2_1$	2	−151.50 −146.72	-	R-^{sup}M	7.049	2.808	175.20
			-	+151.50 +146.72	S-^{sup}P		2.708	172.67
R- **mCB-L1**	$P2_1$	1	+43.50	-	R-^{sup}P	6.708	2.780	177.30
S- **mCB-L1**	$P2_1$	1	-	−43.44	S-^{sup}M	6.709	2.783	173.50
rac- **pCB-L1**	$P2_1/c$	3	±150.77 ±147.38 ±136.97		-	-	2.736 2.751 2.879	166.65 171.93 156.51
R- **pCB-L1**	$P2_12_12_1$	1	−149.82	-	R-^{sup}M	8.962	2.836	160.19
S- **pCB-L1**	$P2_12_12_1$	1	-	+149.99	S-^{sup}P	8.963	2.842	169.03
rac-**I-mCB-L1**	$P2_1/n$	1	−151.57	-	R-^{sup}M	7.088	2.742	172.64
			-	+151.57	S-^{sup}P			
rac- **oCB-L1-b**[d]	$C2/c$	1	−156.72	-	R-^{sup}M	7.138	2.713	158.19
			-	+156.72	S-^{sup}P			

[a] Space groups. [b] Supramolecular chirality of the OH···N hydrogen bonding network. [c] Pitches of the 2_1 supramolecular helices. [d] See reference 1d.

Supramolecular Structures

As mentioned earlier, the supramolecular structures of all those compounds are dominated by HBs of the OH groups and the nitrogen of the pyridine rings. The observed distance of the intermolecular O-H···N HBs from the structures are shorter than 2.75 Å with respect to the sum of the van der Waals radii (∑vdW) of hydrogen and nitrogen atoms and therefore qualify as moderate hydrogen bonds.[6,7] The handedness of the 2_1 helicity for all structures is described using the supramolecular-tilt-chirality method (STC) as illustrated in Figure 3.1-9,[10,11] whereas, the molecules in front of the 2_1 screw axis inclines to the right define as right-handed (^{sup}P), or left-handed (^{sup}M) if inclines to the left. The handedness of the 2_1-helicity for all compounds are summarized in Table 3.1-3.

In the enantiopure carborane pyridylalcohols, as illustrated in Figure 3.1-11a, R-**oCB-L1** affords right-handed P-helices and therefore gives R-^{sup}P (Table 3.1-3). For the opposite enantiomer S-**oCB-L1**, the supramolecular structure shows left-handed M-helices therefore S-^{sup}M. The same observation appears for the enantiopure m-carborane based pyridylalcohols R-**mCB-L1** and S-**mCB-L1** (Figure 3.1-11, c and d) as well, where R enantiomers afford O-H··N supramolecular P-helix and S enantiomers afford M-helix. This result suggests a certain enantiomeric relation of the handedness between the MC and the supramolecular helices/SMC in the solid state.
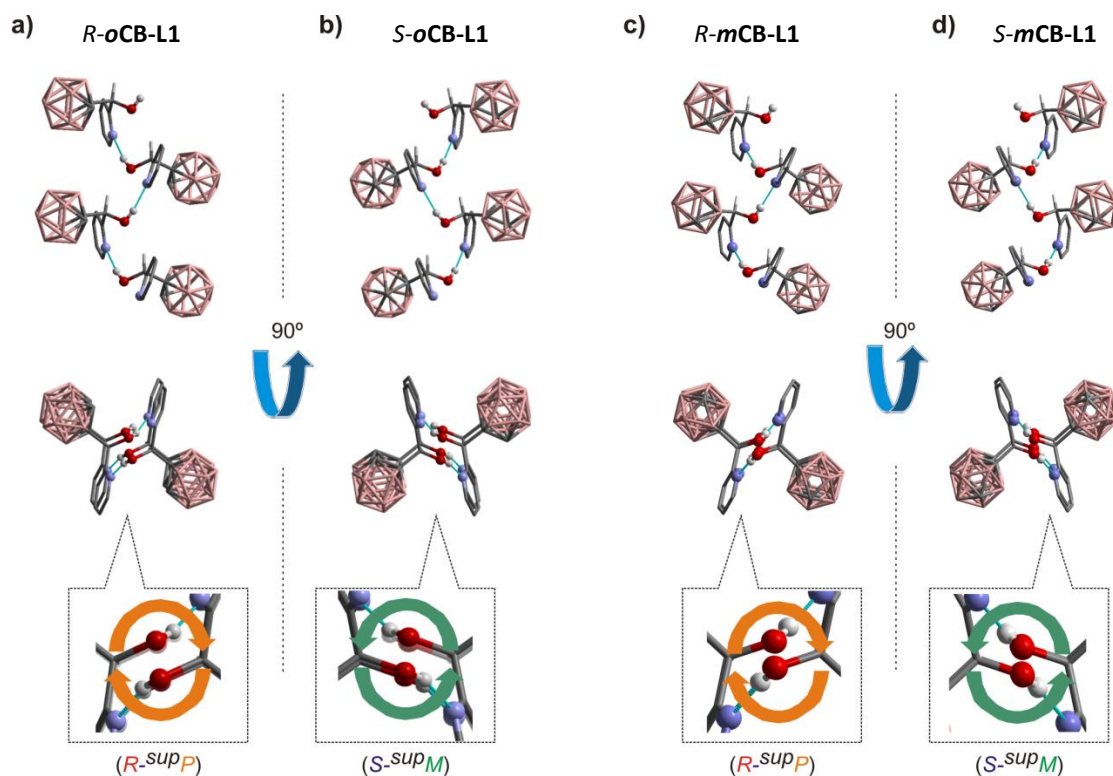
a) *R-o*CB-L1 b) *S-o*CB-L1 c) *R-m*CB-L1 d) *S-m*CB-L1

90° 90°

(R-^{sup}P) (S-^{sup}M) (R-^{sup}P) (S-^{sup}M)

Figure 3.1-11: Supramolecular assemblies of enantiopure *R-o*CB-L1 (a), *S- o*CB-L1 (b), *R-m*CB-L1 (c) and *S-m*CB-L1(d). Top: Projections showing four molecules of each enantiomer forming 1-D 2_1 helical hydrogen bonding columns. Bottom: a magnification of the helical hydrogen bonding networks where handedness is indicated, as determined by the supramolecular tilt chirality method.[10, 11]All hydrogen atoms, except the hydrogen bonded, are omitted for clarity. Color code: B pink; C grey; H white; O red; N blue.

As summarized before in Table 3.1-3, the enantiopure *R-o*CB-L1/ *S-o*CB-L1 and *R-m*CB-L1/ *S-m*CB-L1 have *syn*-conformations with OCCN torsion angles ~±42-44°. Differently, the enantiopure *p*-carborane-based pyridylalcohols *R-p*CB-L1 and *S-p*CB-L1 show *anti*-conformations with OCCN torsion angles ~±150-157°. As shown in Figure 3.1-12, although the O-H···N hydrogen bonded supramolecular helices are formed (*R-p*CB-L1 gives *R*-^{sup}M and *S-p*CB-L1 gives *S*-^{sup}P), the absolute configuration of the molecules and the handedness of the supramolecular helices in solid state are in contrast to the enantiopure *o*- and *m*-carborane derivatives (*R-o*CB-L1/*S-o*CB-L1 and *R-m*CB-L1 / *S-m*CB-L1). This observation suggests that the handedness of the 2_1 supramolecular HB networks is not dependent to the chiral

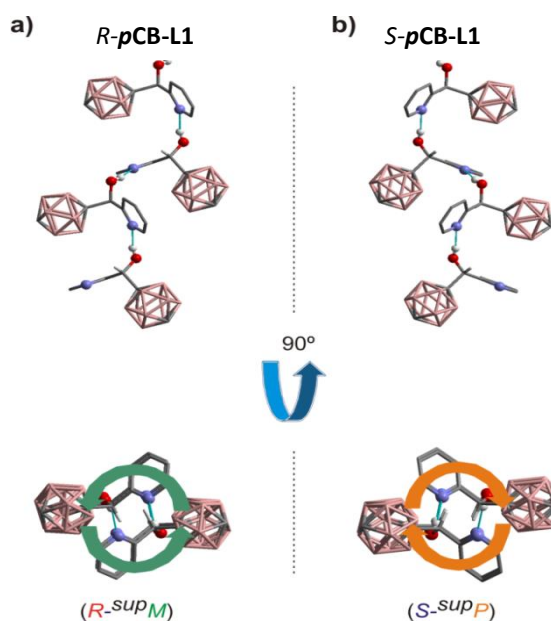a) *R-p*CB-L1 b) *S-p*CB-L1

90°

(R-^{sup}M) (S-^{sup}P)

Figure 3.1-12: Supramolecular assemblies of *R-p*CB-L1 and *S-p*CB-L1 (top) and the projections of helices (bottom).

configuration, but more likely to be dictated by the OCCN torsion angles, which is illustrated in Figure 3.1-13.
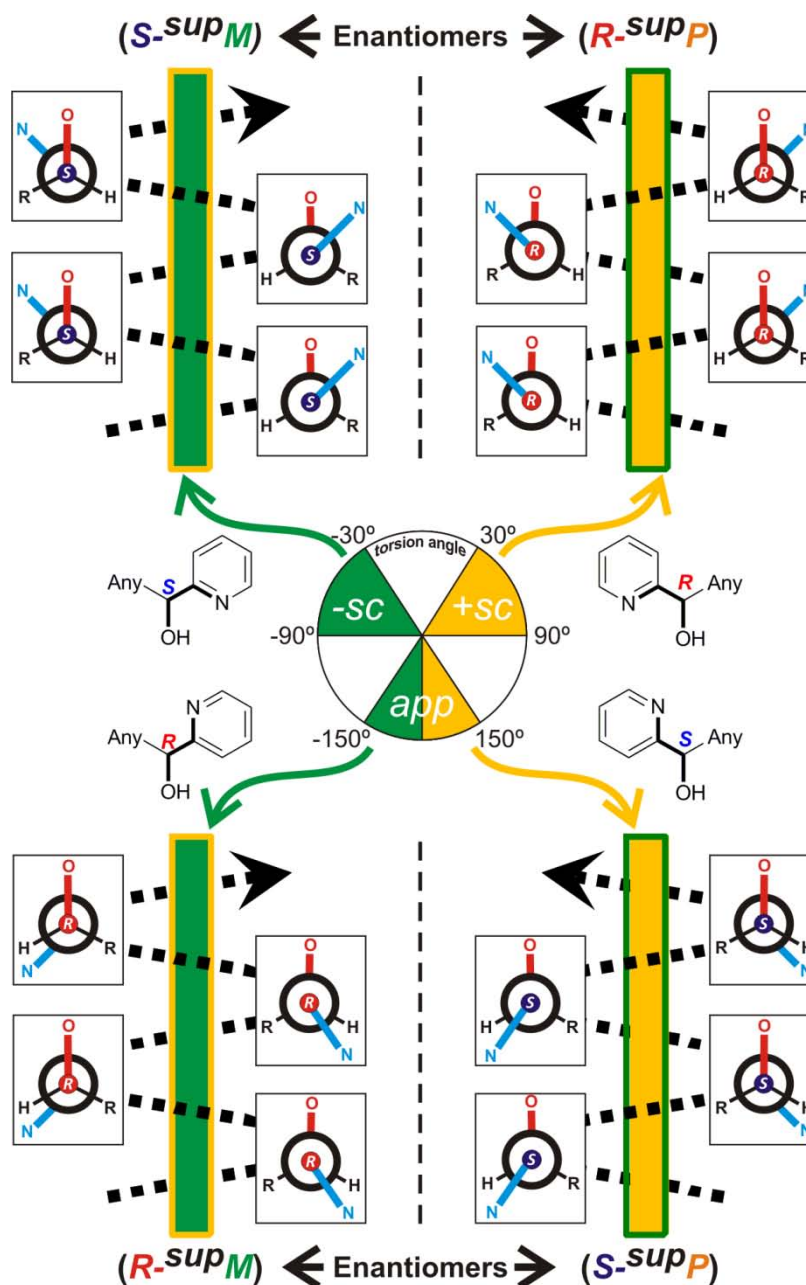

Figure 3.1-13: Pictorial representation of relationship between chirality-torsion angle (center) and handedness of helicity (top and bottom) of the resultant 2_1 supramolecular hydrogen bonding network found in this work. Specification of torsion angles is shown in Klyne-Prelog system (middle, center), in chemical drawing (middle, right and left) and Newman representation (top and bottom) each representing a molecule. Chirality at carbon (*R* or *S*) is indicated and supramolecular chirality (right -^{sup}*P*-or left –^{sup}*M*- handedness) is determined by the supramolecular tilt chirality method.[10,11]

In the racemic carborane pyridylalcohols, for *o*-carborane moiety *rac*-*o*CB-L1, the same relation as the enantiomers *R*-*o*CB-L1 and *S*-*o*CB-L1 is found (*syn*-conformation), that is, *R*-isomers give *R*-^{sup}*P* and *S*-isomers give *S*-^{sup}*M* and the OCCN torsion angles are in the range of ~ 40 (±*sc*). On the contrary, the *m*-carborane derivatives *rac*-*m*CB-L1 crystallized as the *anti*-conformation, which is opposite to its enantiomers *R*-*m*CB-L1 and *S*-*m*CB-L1 (*syn*-conformation). Therefore, *R*-isomers resulting in *R*-^{sup}*M* and *S*-isomers give *S*-^{sup}*P*. Same *anti*-conformation as *rac*-*m*CB-L1 is also found in *rac*-**I**-*m*CB-L1 (Figure 3.1-14).

a) *R*-isomer in*rac*-*m*CB-L1   **b)** *S*-isomer in*rac*-*m*CB-L1   **c)** *R*-isomer in*rac*-**I**-*m*CB-L1   **d)** *S*-isomer in*rac*-**I**-*m*CB-L1

90°   90°

(*R*-^{sup}*M*)   (*S*-^{sup}*P*)   (*R*-^{sup}*M*)   (*S*-^{sup}*P*)
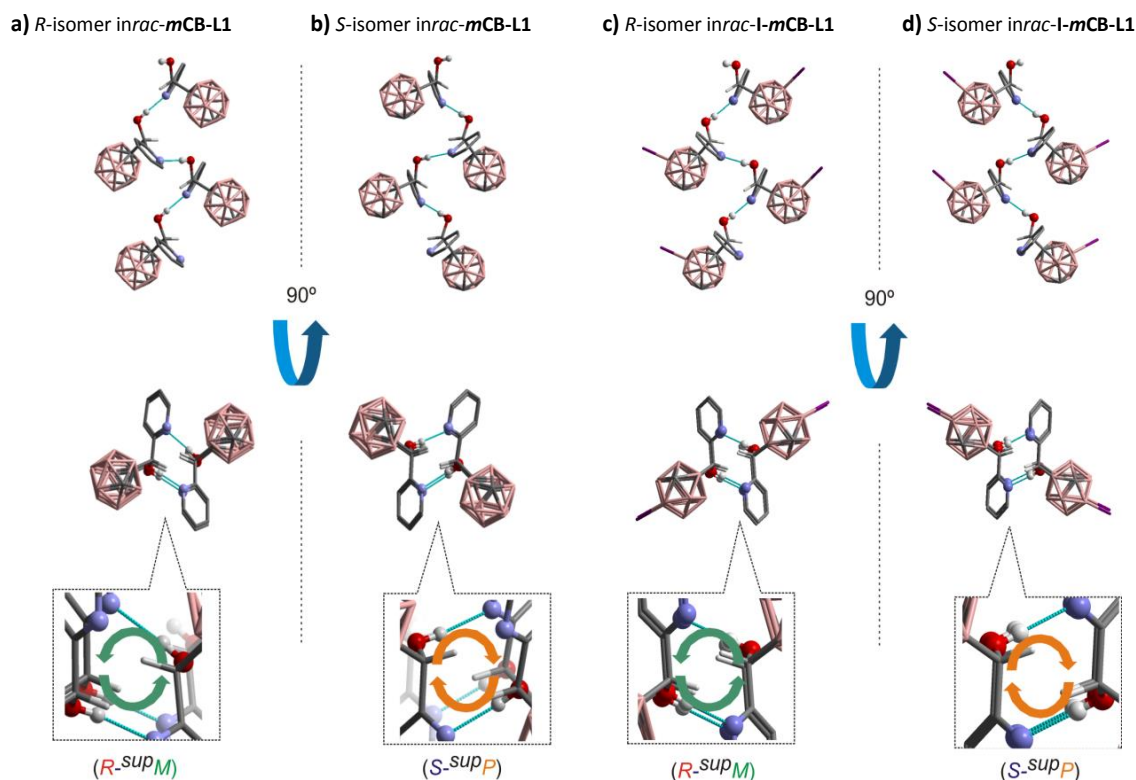
Figure 3.1-14: Supramolecular assemblies of 2_1 helical hydrogen bonding for each enantiomer *R*-*m*CB-L1(a) and *S*-*m*CB-L1(b) in the racemic structure of *m*CB-L1 as well as *R*-**I**-*m*CB-L1 (c) and *S*-*m*CB-L1(d) in the racemic structure of **I**-*m*CB-L1. Top: Two projections showing four molecules of each enantiomer forming 1-D 2_1 helical hydrogen bonding columns. Bottom: a magnification of the helical hydrogen bonding networks where handedness is indicated, as determined by the supramolecular tilt chirality method.[10, 11] See Table 3.1-3 for metric parameters. All hydrogen atoms, except the hydrogen bonded, are omitted for clarity. Color code: B pink; C grey; H white; O red; N blue.

The results of the racemic *o*- and *m*-carborane derivatives (*o*CB-L1 and *m*CB-L1) are in good agreement as the relation shown in Figure 3.1-13. That is, by measuring the sign and the value of the OCCN torsion angle, combine with the absolute configuration of the molecules, the handedness of the supramolecular helices can be predicted. For example, a molecule like *rac*-*o*CB-L1 that has a *syn*-conformation and positive OCCN torsion angle less than 90°, in principlewill be expected to give *R*-^{sup}*P* supramolecular structure based on this hypothesis.

However, unexpectedly, the *p*-carborane derivative *rac-pCB-L1* does not form the O-H···N hydrogen bonded helices. Instead, a hydrogen bonded trimer in *RRS* and *SSR* configurations is formed (Figure 3.1-15). Recrystallization of *rac-pCB-L1* with different solvents (hexane, ethanol/hexane or acetone) result in the same trimer as it might due to the significantly lower packing density for *rac-pCB-L1* (1.123 gcm^{-3}) than the enantiomers *R-pCB-L1* and *S-pCB-L1* (1.238 gcm^{-3}).
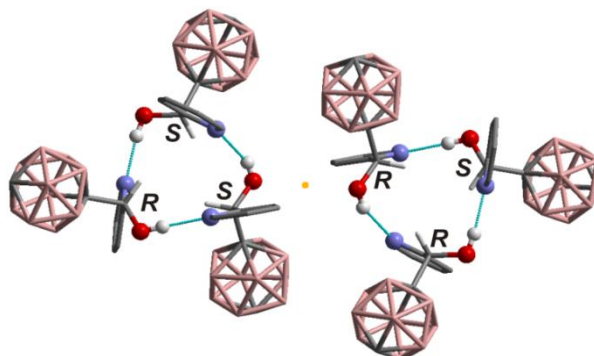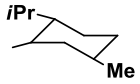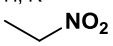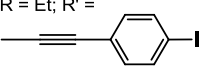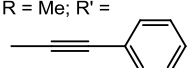

Figure 3.1-15: Supramolecular assembly of *rac-pCB-L1* showing 6 molecules forming two pairs of hydrogen bonded trimers. Configurations of stereogenic centers are indi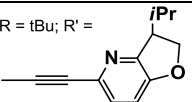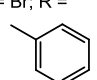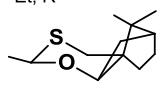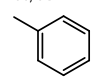cated and inversion center is shown as an orange dot. All hydrogen atoms, except those for the CHOH group, are omitted for clarity. Colour code: B pink; C gray; H white; O red; N blue.

In order to further investigate the correlation between the moderate O-H···N hydrogen bonds versus the supramolecular helicity as proposed for pyridylalcohol ligands. Two extra molecules *rac-oCB-L1-b* and *rac-Ph-L1* were re-examined, and a total of 10 extra different crystal structures were found in the Cambridge Structural Database (CSD, version 5.35 updated in February 2014) (Table 3.1-4). Detailed analysis shows majority of those molecules follow the same rule as proposed above (10 out of 12).

Table 3.1-4: Selected molecular, supramolecular and crystal parameters for racemic and/or enantiopure non carborane-based 2-pyridylalcohols from the CSD and the chemical structures.

Refcode[a]	SG[b]	Z'	OCCN torsion (º)		SMC[c]	P (Å)[d]	ON (Å)	OHN (º)
			R-isomer	*S*-isomer				
Enantiopure Structures								
R' = H; R = OMe, Ph **ALUKEX**	$P2_12_12_1$	1	-	+150.37	*S-^{sup}P*	8.187	2.775	-[e]
R' = H; R = O (cyclopentenone) **ERIWOR**	$P2_12_12_1$	1	-	+169.02	*S-^{sup}P*	8.427	2.796	178.33

Structure	Space group	Z			Chirality			Pitch
R' = H; R = *iPr* ... Me **IJEJOW**	$P2_1$	1	-	−46.74	*S*-^{sup}*M*	5.561	2.862	-[e]
R' = H; R = ...NO$_2$ **ISUXEA**	$P2_12_12_1$	1	−154.46	-	*R*-^{sup}*M*	7.145	2.720	172.55
R = Et; R' = ...I **JOGDUF**	$P2_1$	1	+174.77	-	*R*-^{sup}*M*	9.387	2.831	165.60
R = Me; R' = ... **JOGFAN**	$P2_12_12_1$	1	-	+171.61	*S*-^{sup}*P*	9.635	2.927	172.52
R = tBu; R' = *iPr* N O **KORKAD**	$P2_1$	1	-	+155.51	*S*-^{sup}*P*	6.893	2.901	-[e]
R' = Br; R = ... **NIZFOS**	$P2_12_12_1$	1	+177.40	-	*R*-^{sup}*P*	8.733	2.867	168.62
R = Et; R' = S O ... **XURJEZ**	$P2_1$	1	-	+157.10	*S*-^{sup}*P*	6.553	2.906	151.82
Racemic structures								
R' = H; R = ... *rac*-**Ph-L1**	Pna2_1	1	−150.73	-	*R*-^{sup}*M*	9.248	2.800	166.71
			-	+150.73	*S*-^{sup}*P*			
TICPIG	$P2_1/c$	1	−151.31	-	*R*-^{sup}*M*	9.458	2.842	174.86
			-	+151.31	*S*-^{sup}*P*			

[a] Identifiers for crystals structures in the Cambridge Structural Database. [b] Space group; [c] Supramolecular chirality of the OHN hydrogen bonding network. [d] Pitches of the 2_1 supramolecular helices. [e] H atoms not available.

Conclusively, the analyses of these 20 structures (carborane-based ligands **CB-L1** and the conventional organic ligands from CSD) show that certain conformation of the molecules seems can be translated into O-H⋯N helical networks with specific handedness and it is suggested that the correlation between the OCCN torsion angles of the molecules and the handedness of the supramolecular helices exist. Although there are possibly various mechanisms involved for the correlation of the MC and the SMC, according to this study, the OCCN torsion angles of the molecules could be one of the many driving factors for the formation of the supramolecular helices.

3.1.2.2 Homochiral Recognition of Disubstituted *ortho*-Carborane-Based Pyridylalcohol Derivatives

Self-assembly and organization of chiral species is another important study in crystal engineering to mimic the formation of high order functional structures in nature, especially the homochrial recognition of the chiral molecules in life.[12] However, it is still a challenge to design and prepare the chiral artificial self-assembled systems due to the unclear mechanism.[12,13] Many reports show the occurrence of homochiral recognition from the corresponding racemic mixture,[14,15] that is, an enantiomer preferentially recognizes itself to generate homochiral self-assemblies (*R*···*R* and *S*···*S*). The homochiral self-recognition of *meso*-compounds that incorporate both enantiomeric configurations and generate the homochiral arrangement (*R-S*···*S-R*···*R-S*···) is also found, although it is less common.[16]

The analyses of the supramolecular structures of the family of racemic monosubstituted *o*-carborane-based pyridylalcoholspreviously reported in the group,[1] revealed that the monosubstituted compounds containing non-nitrogenated aromatic rings do not show any homo-chiral recognition (Scheme 3.1-8, left). However, introduction of nitrogenated aromatic rings into the compounds seems to promote certain homochiral recognition (4 out of 9 structures) (Scheme3.1-8, right).

Scheme 3.1-8. Summary of supramolecular synthons for previously reported first generation of carboranyl alcohols and homochiral recognition
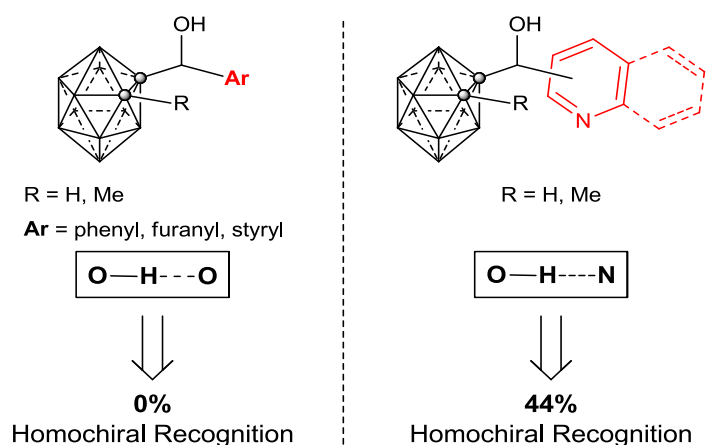
To further explore the possibility for complete homochiral recognition in this system, the structures of the corresponding disubstituted *o*-caraborane-based pyridylalcohol with phenyl, pyridyl or quinolyl moieties (Scheme 3.1-9) from racemic mixtures and *meso* stereoisomers have been analyzed and a complete homochiral self-assembly has been observed and shown in the following.

Scheme 3.1-9. Second generation of carboranyl alcohols
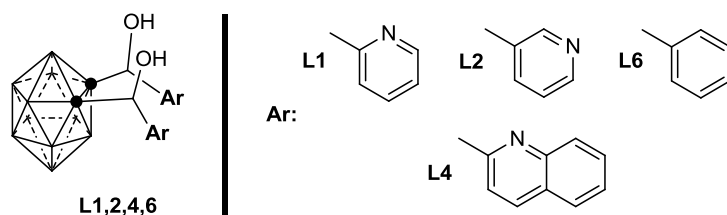
The structures of all these compounds have been determined by single-crystal XRD. SQUEEZE[17] was utilized to remove the disordered solvent molecules, and the hydrogen positions of the alcohols were determined from the different map and refined freely without any restrain. As mentioned in section 3.1.1.2, the disubstituted compounds have two diastereoisomers: *meso* compounds (*RS*; OH groups are in *syn*-orientation) and racemic compounds (mixture of *SS* and *RR*; OH groups are in *anti*-orientation). In the following, the *anti* or *syn*-isomers nomenclature will be employed to represent the racemic or *meso* compounds respectively.

Molecular Structures

The compounds *syn*-**oCB-(L1)₂**, *anti*-**oCB-(L1)₂**, *syn*-**oCB-(L6)₂** and *anti*-**oCB-(L4)₂** crystallized as solvates (*syn*-**oCB-(L1)₂**·2MeOH, *anti*-**oCB-(L1)₂**·MeOH, *anti*-**oCB-(L1)₂**·2EtOH, *syn*-**oCB-(L6)₂**·0.25H₂O and *anti*-**oCB-(L4)₂**·2H₂O) and *syn* **oCB-(L2)₂** crystallized without solvent molecules in its lattice (Figure 3.1-16).
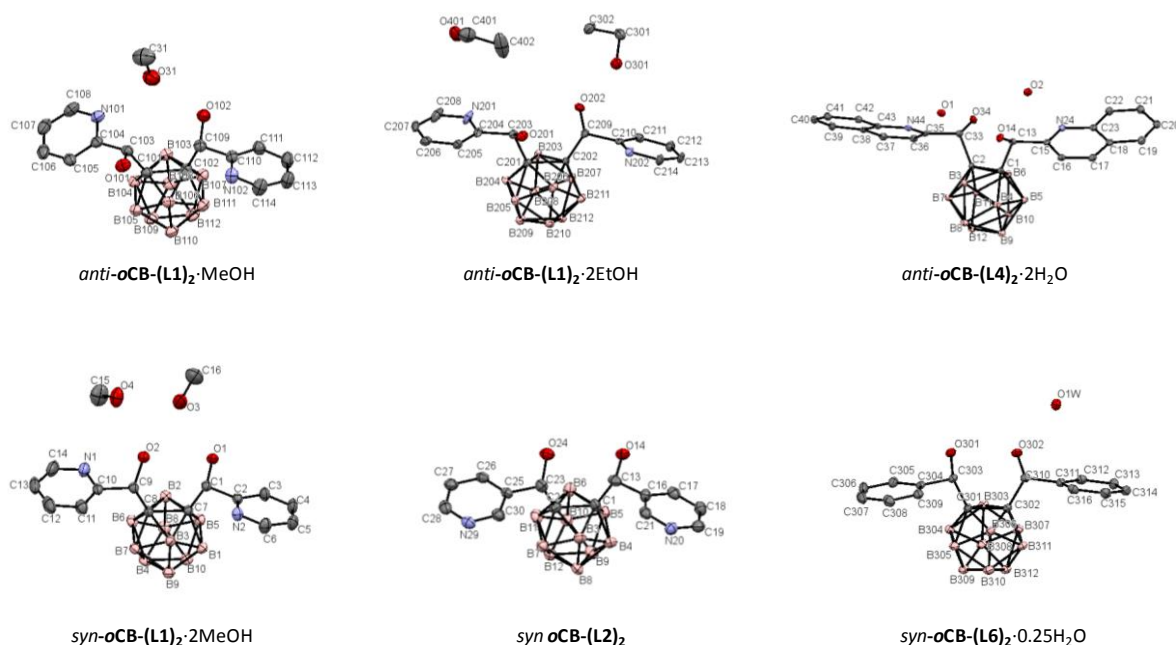

anti-**oCB-(L1)₂**·MeOH   anti-**oCB-(L1)₂**·2EtOH   anti-**oCB-(L4)₂**·2H₂O

syn-**oCB-(L1)₂**·2MeOH   syn **oCB-(L2)₂**   syn-**oCB-(L6)₂**·0.25H₂O

Figure 3.1-16: Molecular structures of *syn*-**oCB-(L1)₂**·2MeOH, *anti*-**oCB-(L1)₂**·MeOH, *anti*-**oCB-(L1)₂**·2EtOH, *syn*-**oCB-(L2)₂,** *syn*-**oCB-(L6)₂**·0.25H₂O and *anti*-**oCB-(L4)₂**·2H₂O. Thermal ellipsoids set at 35% probability (B-H and pyridine hydrogen atoms are omitted for clarity)

Supramolecular Structures

The supramolecular structures for all these compounds are built based on O–H···N and/or O–H···O hydrogen bonds. The distances of these intra- and/or intermolecular hydrogen bonds are shorter than the 2.75/2.72 Å with respect to the sum of the van der Waals radii (∑vdW) of hydrogen and nitrogen/oxygen atoms, where the intermolecular hydrogen bonds are near linear. Therefore, they are qualified as moderate hydrogen bonds.[6, 7]

For 2-pyridylalcohol derivatives *o*CB-(L1)$_2$ (*syn* and *anti*), all the compounds are assembled as dimers. For comparison purpose, the unsolvated *syn*-*o*CB-(L1)$_2$[18] will be briefly described. As shown in Figure 3.1-17, the unsolvated *syn*-*o*CB-(L1)$_2$ forms a dimer through two bifurcated O–H···(N)(O) hydrogen bonds: one intra (with nitrogen) and one intermolecular (with oxygen). The remaining OH groups are involved in the intramolecular O–H···N hydrogen bonds which facilitates the intramolecular C–H···O interactions. *syn*-*o*CB-(L1)$_2$·2MeOH also forms dimers and the arrangement of the chiral pyridylalcohol moieties is very similar to the corresponding moieties of the unsolvated *syn*-*o*CB-(L1)$_2$, except for the interruption of the intermolecular hydrogen bonds (observed in unsolvated *syn*-*o*CB-(L1)$_2$) by the methanol molecules. These interactions lead to the formation of homochiral dimers (··*R*-*S*···*S*-*R*··) as can be seen in Figure 3.1-17.
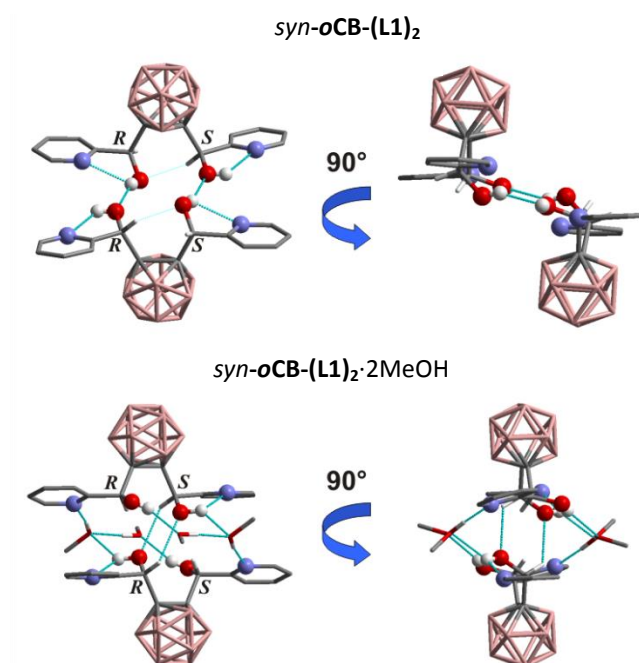

Figure 3.1-17: Supramolecular assemblies of *syn*-*o*CB-(L1)$_2$ (Top) and *syn*-*o*CB-(L1)$_2$·2MeOH (Bottom). Projections showing 2 molecules of each compound forming hydrogen bonded dimers. Configurations of chiral carbons are indicated. All hydrogen atoms, except the hydrogen bonded, are omitted for clarity. Color code: B pink; C grey; H white; O red; N blue.

Crystal Structures of *anti-o*CB-(L1)$_2$·MeOH and *anti-o*CB-(L1)$_2$·2EtOH also show dimeric arrangements (Figure 3.1-18). The dimers are formed by intermolecular O–H···N hydrogen bonds in a R2,2(16) ring, which leaves two donors (OH) and two acceptors (N) to interact with the methanol or ethanol solvent molecules to form two D2,2(4) patterns, resulting in the homochiral self-assembly for both *anti-o*CB-(L1)$_2$·MeOH and *anti-o*CB-(L1)$_2$·2EtOH.
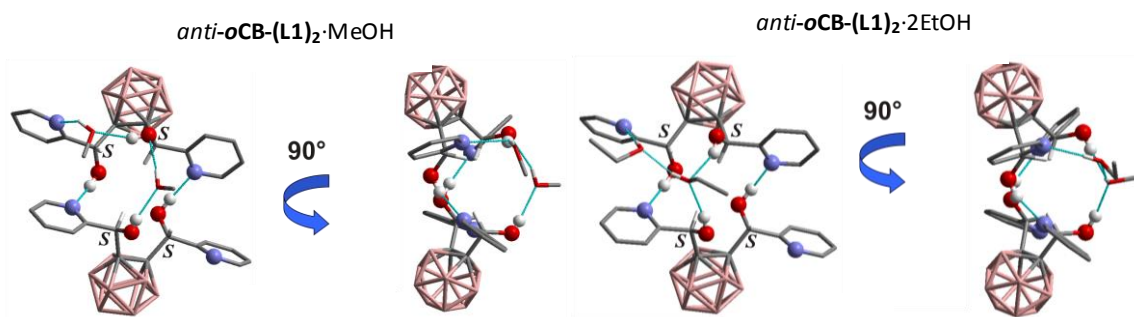

*anti-o*CB-(L1)$_2$·MeOH

*anti-o*CB-(L1)$_2$·2EtOH

Figure 3.1-18: Supramolecular assemblies of *anti-o*CB-(L1)$_2$·MeOH (Top) and *anti-o*CB-(L1)$_2$·2EtOH (Bottom). Projections showing 2 molecules of each compound forming hydrogen bonded dimers. Configurations of chiral carbons are indicated. All hydrogen atoms, except the hydrogen bonded, and solvent molecules in the channels are omitted for clarity. Color code: B pink; C grey; H white; O red; N blue.

Moreover, the dimers of the same chirality assemble together by weak interactions and generate channels that are occupied by solvent molecules. Selected example *anti-o*CB-(L1)$_2$·2EtOH is shown in Figure 3.1-19.
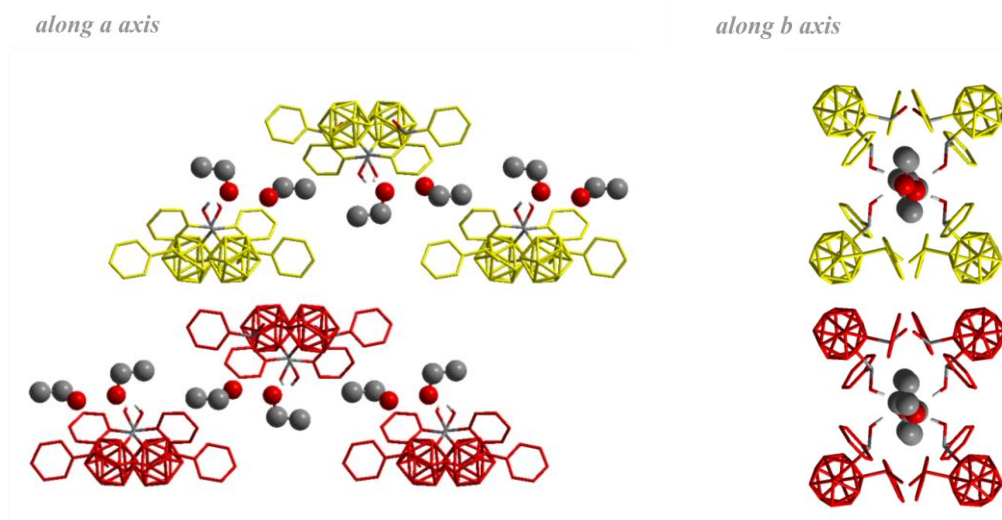

along a axis

along b axis

Figure 3.1-19: Comparative views of supramolecular assemblies of *anti-o*CB-(L1)$_2$·2EtOH, along the ethanol containing channels (top), and perpendicular to them (bottom). Three sets of homochiral dimers of different chirality (red for *R* enantiomers and yellow for *S*) assemble around a crystallographic 2$_1$ screw axes to generate the channels. Ethanol molecules are shown in ball and stick style. Color code: B pink; C grey; O red.

In the case of 3-pyridine derivatives *o*CB-(L2)$_2$, meso *syn*-*o*CB-(L2)$_2$ forms intermolecular O–H···N hydrogen bonds between two different molecules and gives rise to a zigzag 2D layer (Figue 3.1-20). The *R*-moieties only interact with *R*-moieties (and vice versa) to form supramolecular layers through homochiral hydrogen bonded chains, and thus afford a 3D structure (Figure 3.1-20, right).
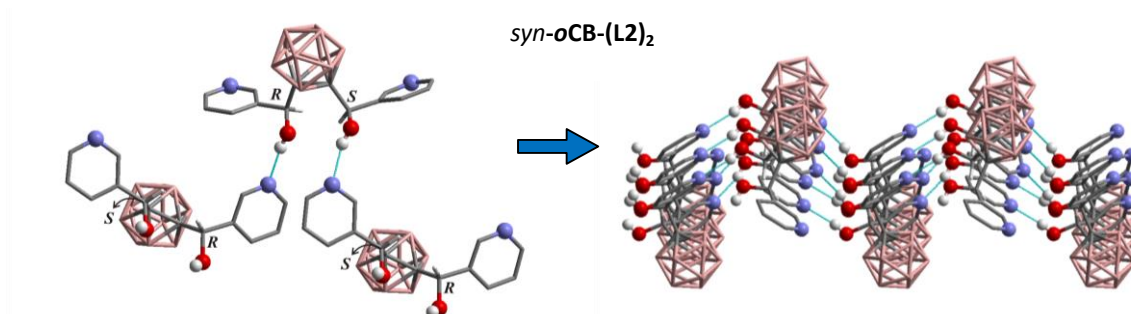

Figure 3.1-20: Supramolecular assemblies of *syn*-*o*CB-(L2)$_2$. Two projections showing three or fifteen molecules of *syn*-*o*CB-(L2)$_2$ forming hydrogen bonded zigzag layers.Configurations of chiral carbons are indicated. See Table 3.1-4 for metric parameters. All hydrogen atoms, except the hydrogen bonded, are omitted for clarity. Color code: B pink; C grey; H white; O red; N blue.

Phenyl derivatives *o*CB-(L6)$_2$ is expected to have different effect due to the absence of the nitrogenated ring. Only OH moieties can be involved in the interactions. However, surprisingly, homochiral recognition also takes place in *syn*-*o*CB-(L6)$_2$·0.25H$_2$O. As shown in Figure 3.1-21, one intramolecular O–H···O hydrogen bond is formed in each molecule, and the remaining OH group forms intermolecular O–H···O hydrogen bonds, resulting in a pentameric cluster by combination of four molecules and one water molecule.
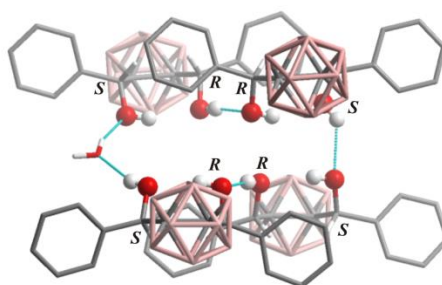

Figure 3.1-21: Supramolecular assemblies of *syn*-*o*CB-(L6)$_2$·0.25H$_2$O. Projection shows four molecules of *syn*-*o*CB-(L6)$_2$ and one molecule of water form a hydrogen bonded pentamer. Configurations of chiral carbons are indicated. All hydrogen atoms, except the hydrogen bonded, are omitted for clarity. Color code: B pink; C grey; H white; O red; N blue.

For 2-quinoline derivative *o*CB-(L4)$_2$, the formation of O–H···N hydrogen bonds are affected by the increased bulkiness around the nitrogen atoms and resulting in a different manner of homochiral self-assemblies. Two *anti-o*CB-(L4)$_2$ molecules and two water molecules interact with each other to form intermolecular O–H···O hydrogen bonds in cyclic, tetrameric styles (Figure 3.1-22).
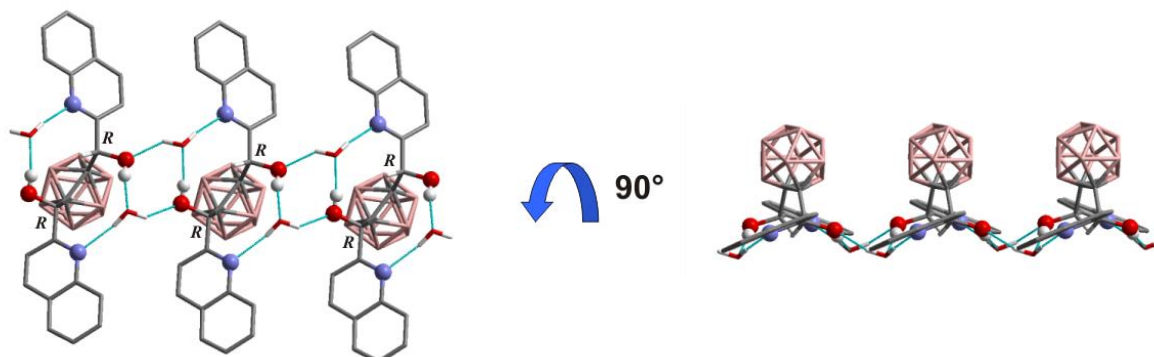

Figure 3.1-22: Supramolecular assembly of *anti-o*CB-(L4)$_2$·2H$_2$O. Two projections showing three molecules of *anti-o*CB-(L4)$_2$ forming O–H···O and O–H···N hydrogen bonded chains that include water molecules along the *a* axis. Configurations of chiral carbons are indicated. All hydrogen atoms, except the hydrogen bonded, are omitted for clarity. Color code: B pink; C grey; H white; O red; N blue.

The remaining H atom from the water molecule forms intermolecular O–H···N hydrogen bonds that lead to the formation of homochiral chains (*i.e.R-R···R-R···*). These homochiral chains are then packed as racemic columns by weak interactions (Figure 3.1-23).

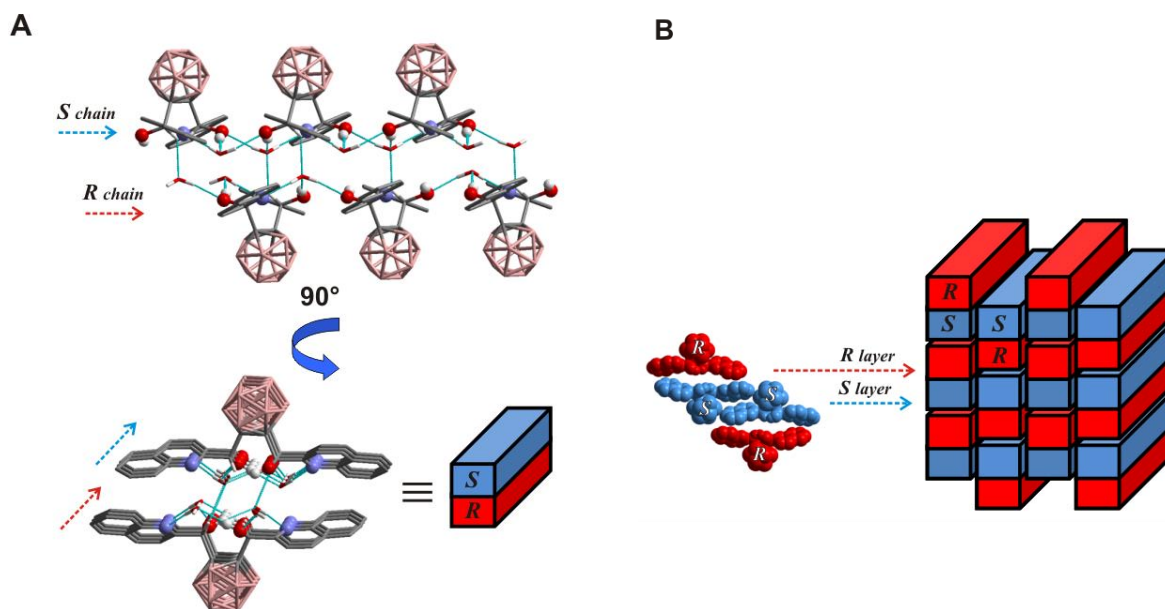**Figure 3.1-23**: (A): Comparative views of self-assembled supramolecular homochiral chains (indicated by arrows) of *anti-o*CB-(L4)$_2$··2H$_2$O, perpendicular (top) and along the O–H···O and O–H···N hydrogen bonds (bottom) giving racemic columns (represented as red/blue rectangular prism). Color code: B pink; C grey; H white; O red; N blue. (B): A pictorial representation of the 3D assembly of racemic columns of *anti-o*CB-(L4)$_2$·2H$_2$O.

The complete homochiral self-assemblies of all those analyzed compounds (*syn*-**oCB-(L1)₂**·2MeOH, *anti*-**oCB-(L1)₂**·MeOH, *anti*-**oCB-(L1)₂**·2EtOH, *syn*-**oCB-(L2)₂,** *syn*-**oCB-(L6)₂**·0.25H₂O and *anti*-**oCB-(L4)₂**·2H₂O) take place independently on whether the compounds are in *syn*- (meso) or *anti*-(racemic) forms. This could be due to the stereoselective intermolecular O–H···N/O hydrogen bonding, although the possible influences from the spatial requirements and other interactions between the molecules are inevitable. The mechanism for the self-recognition in these compounds is still unclear. Further studies on these behaviors and detail analyses on more related compounds are required. For instance, recrystallization in various solvents and analysis on the corresponding crystal structures can provide evidence whether the solvent molecules have influence for the homochiral recognition. In addition, more structures from different substituents such as **oCB-(L4)₂, oCB-(L5)₂** and even the corresponding conventional organic and *m*-carborane derivatives are crucial to determine whether the presence of pyridylalcohols drive the homochiral recognition.

References

[1]   (a) V. Terrasson, D. Prim, C. Viñas, J. G. Planas, F.Teixidor,M. E.Light, M. B.Hursthouse, *J. Org. Chem.* **2008**, *73*, 9140.(b) V.Terrasson, D. Prim ,J. G.Planas, F.Teixidor, C. Viñas, M. E.Light, M. B. Hursthouse, *Eur. J. Chem.***2009**, *15*, 12030 (c) V.Terrasson, Y García,. P.Farràs, F.Teixidor, C. Viñas,J. G.Planas, D.Prim, M. E.Light, M. B. Hursthouse, *CrystEngComm.***2010**,*12*, 4109. (d) F. Di Salvo, J. G. Planas, B. Camargo, Y.Garcia, F.Teixidor, C. Viñas, M. E.Light, M. B.Hursthouse, *CrystEngComm*,**2011**, *13*, 5788.

[2]   A. R. Popescu, A. D. Musteti, A. Ferrer-Ugalde, C. Vinas, R. Nunez, F. Teixidor, *Chem. Eur. J.,***2012**, *18*, 3174.

[3]   (a) A. M.Spokoyny, C. W.Machan, D. J.Clingerman, M. S.Rosen, M. J.Wiester, R. D.Kennedy, C. L.Stern, A. A.Sarjeant, C. A.Mirkin, *Nature Chemistry***2011**,*3*, 590. (b) T.Teixidor, G.Barberà, A.Vaca, R.Kivekäs, R.Sillanpää, J.Oliva, C.Viñas, *J. Am. Chem. Soc.* **2005**, *127*, 10158. (c) F. M. Alexander, **1991**, *Icosahedral carborane derivatives.* Durham theses, DurhamUniversity.Available at Durham E-Theses Online: http://etheses.dur.ac.uk/1186/ (d) S. Hermanek, *Inorg. Chim. Acta.*, **1999**, *289*, 20.

[4]   (a) J. F. Valliant, K. J. Guenther, A. S. King, P. Morel, P. Schaffer, O. O. Sogbein, K. A. Stephenson, *Coord. Chem. Rev*, **2002**, *232*, 173-230. (b) M. Scholz, E. Hey-Hawkins, *Chem. Rev.***2011**, *111*, 7035.

[5]   Z. P. Zheng, W. Jiang, A. A. Zinn, C. B. Knobler, M. F. Hawthorne, *Inorg. Chem.***1995**, *34*, 2095

[6]   (a) G. R. Desiraju, *Crystal Engineering. The Design of Organic Solids*, Elsevier Science Publishers B.V.: Amsterdam, **1989**. (b) G. R. Desiraju, T. Steiner. *The Weak Hydrogen Bond in Structural Chemistry and Biology*; Oxford University Press: Oxford, **2001**. (c) J. L. Atwood, J. W. Steed, *Encyclopedia of Supramolecular Chemistry*; Marcel Dekker: New York, **2004**. (d) J. W. Steed, J. L. Atwood, *Supramolecular Chemistry*, 2nd edition; Wiley: Chichester, **2009**.

[7]   (a) M. C. Etter, *Acc. Chem. Res.***1990**, *23*, 120. (b) T. Steiner, *Angew. Chem.***2002**, *114*, 50; *Angew. Chem. Int. Ed*. **2002**, *41*, 48. (c) P. Metrangolo. H. Neukirch, T. Pilati, G. Resnatti, *Acc. Chem. Res.***2005**, *38*, 386. (d) S. Kitagawa, K. Uemura, *Chem. Soc. Rev.***2005**, *34*, 109. (e) D. A. Britz, A. N. Khlobystov, *Chem. Soc. Rev.***2006**, *35*, 637.

[8]   (a) B. Moulton, M. Zaworotkko, *J. Chem. Rev.***2001**, *101*, 1629. (b) A. Ciesielski, C. A. Palma, M. Bonini, P. Samori, *Adv. Mater.***2010**, *22*, 3506.

[9]   G. E. Schulz, R. H. Schirmer, *Principles of Protein Structure*; C. R. Cantor Eds.; Springer-Verlag: New York, **1979**.

[10] T. Sasaki, I. Hisaki, T. Miyano, N. Tohnai, K. Morimoto, H. Sato, S. Tsuzuki, M. Miyata. *Nat. Commun*, **2013**, *4*, No. 1787, DOI: 10.1038/ncomms2756.

[11] I. Hisaki, T. Sasaki, T. Miyano, N. Tohnai, K. Morimoto, *Chem. Eur. J.***2012**, *22*, 3506-3520

[12] For example: (a) J.M.Lehn, *Supramolecular Chemistry:Concepts and Perspectives*; VCH: Weinheim, **1995**; (b) G.M.Whitesides, B.Grzybowski, *Science***2002**, *295*, 2418. (c) A. Guijarro, M.Yus, *The Origin of Chirality in the Molecules of Life. A Revision fromAwareness to the Current*

Theories and Perspectives of this Unsolved Problem; The Royal Society of Chemistry: Cambridge, U.K., **2009**.

[13] For example: (a) J. J. L. M.Cornelissen, A. E.nRowan, R. J. M. Nolte, N. A. J. M. Sommerdijk, *Chem. Rev.***2001**, *101*, 4039.(b) L.Pérez-García, D. B.Amabilino,*Chem. Soc. Rev.***2002**, *31*, 342.(c) M. A.Mateos-Timoneda, M.Crego-Calama, D. N.Reinhoudt, *Chem. Soc. Rev.***2004**, *33*, 363. (d) L.Pérez-García, D. B.Amabilino,*Chem. Soc. Rev.***2007**, *36*, 941. (e) G. A. Hembury, V. V.Borovkov,Y.Inoue, *Chem. Rev.***2008**,*108*, 1. (f) J.Crassous, *Chem. Soc. Rev.***2009**, *38*, 830. (g) F.Blanco, I.Alkorta, I.Rozas, J. J. Elguero,*Phys.Org. Chem.***2010**, *23*, 1155. (h) K.Tahara, H.Yamaga, E.Ghijsens, K.Inukai, J.Adipoejoso, M. O.Blunt, S.De Feyter, Y.Tobe, *Nat.Chem.* **2011**,*3*, 714.

[14] J.Jaques, A.Collet, S. H.Wilen, *Enantiomers, Racemates, andResolutions*; Krieger Publishing, FL, **1994**.

[15] For example: (a) S. G. Telfer, T.nSato, R.Kuroda, J.Lefebvre, D. B.Leznoff, *Inorg. Chem.***2004**, *43*, 421. (b) A. T.ten Cate,P. Y. W.Dankers, H. Kooijman, A. L.Spek, R. P. Sijbesma, E. W. Meijer, *J. Am. Chem. Soc.***2003**, *125*, 6860. (c) I.Weissbuch, G.Bolbach, H. Zepik, E.Shavit, M.Tang, J.Frey, T. R.Jensen, K.Kjaer, L.Leiserowitz, M. Lahav, *J. Am. Chem. Soc.***2002**, *124*, 9093.(d) Y.Ishida, T. Aida, *J. Am. Chem. Soc.***2002**, *124*, 14017. (e) L.Isaacs, D.Witt, *Angew. Chem. Int. Ed.***2002**, *41*, 1905. (f) E.Murguly, R.McDonald, R. N.Branda, *Org. Lett.***2000**, *2*, 3169. (g) L. J.Prins,J.Huskens, F.de Jong, P.Timmerman, D. N. Reinhoud, *Nature*,**1999**, *398*, 498.

[16] (a) S.Takahasi,T.Jukurogi, T.Katagiri, K.Uneyama, *CrystEngComm***2006**,*8*, 320. (b) S.Takahasi, T.Katagiri, K. Uneyama, *CrystEngComm***2006**, *8*, 132. (c) S. Takahasi, T.Katagiri,K.Uneyama, *Chem. Commun.***2005**,*127*, 3658.

[17] SQUEEZE: P. v.d. Sluis, A. L. Spek, *Acta Crystallogr*, **1990**, *A46*, 194-201

[18] B. Peng, Y. Nie, J. Miao, Z. Zhang, M. Xu, G. Sun, *J. Mol. Struct.***2012**, *1007*, 214.

3.2 Monosubstituted N,O-Type *ortho*- and *meta*-Carborane-Based Pyridylalcohol Complexes

2-pyridylalcohols (Figure 3.2-1) proved to be convenient precursors for the synthesis of polynuclear complexes, owing to their N,O-chelation capabilities, their relatively high acidity and, when deprotonated, the efficient O-bridging coordination over two or three metal centres (Figure 3.2-1A).[1] On the other hand, n-pyridylalcohols (n = 3, 4) can be used as monodentate ligands through the nitrogen or oxygen atoms but can also be used as bridging ligands for the construction of coordination polymers (Figure 3.2-1B).[2]
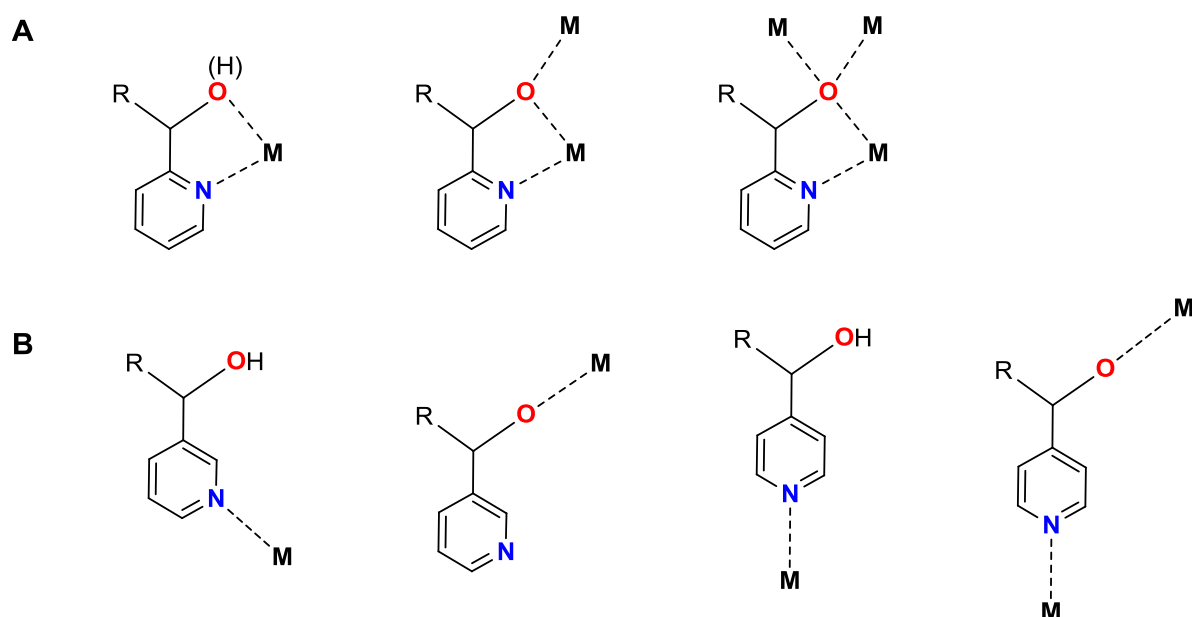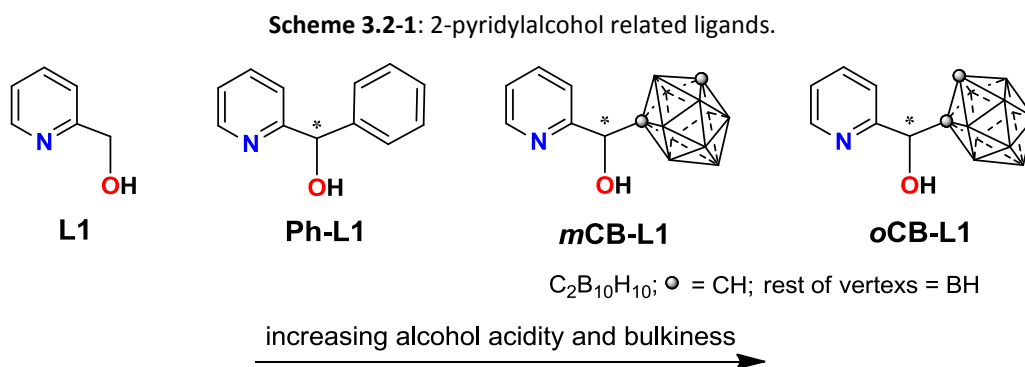

Figure 3.2-1: Some of the possible coordination mode of the monosubstituted pyridylalcohol ligands.

The pyridylalcohols described in the previous chapter can be regarded as hydroxymethylpyridine ligands (**L1** in Scheme 3.2-1) where one of the H atoms at the –CH$_2$– position of the alcohol arm has been replaced by a carboranyl fragment. The latter is shown for the (2-hydroxymethyl)pyridine in Scheme 3.2-1.

Scheme 3.2-1: 2-pyridylalcohol related ligands.

L1   **Ph-L1**   *m*CB-L1   *o*CB-L1

C$_2$B$_{10}$H$_{10}$; ● = CH; rest of vertexs = BH

increasing alcohol acidity and bulkiness

Phenyl derivatives are often compared with carboranyl moieties because of the similar size and the electron-withdrawing character (Chapter 1.1). Introduction of carborane into the **L1** backbone is expected to exert a higher acidity of the alcohol and an increase of size and hydrophobicity, with respect to the related phenyl-**L1** derivative (Scheme 3.2-1).

The first series of cobalt complexes with *o***CB-L** were published in our group earlier, providing an interesting antiferromagnetic and intrinsically porous molecular material.[3] As part of this PhD work, a series of unsymmetric iron (III) complexes have been obtained with the corresponding 2-pyridylalcohol ligands **CB-L1** and luminescent copper (I) complexes with 3- and 4- pyridylalcohol ligands **CB-L2** and **CB-L3**. These iron (III) and copper (I) complexes have been characterized and their properties will be discussed in the following sections.

3.2.1 Unsymmetric Iron (III) Complexes

Iron complexes have been widely studied for decades in material science not only because iron is one of the cheapest, most abundant and non-toxic transition metal source, but also for their attractive magnetic properties and oxidation states to develop potential materials for molecular magnetism, catalytic applications, molecular switches, etc.[4] The introduction of chirality increases the value on such materials in areas such as enantioselective catalysis, magnetochirality or non-linear optic materials.[5] In this section, 2-pyridylalcohol ligands **CB-L1** are applied and the complete study on the influence of the *ortho-* and *meta*-carborane moieties towards the formation and properties of iron complexes will be shown. Those will be also compared with the formation of the iron complexes from the phenyl **Ph-L1** ligand.
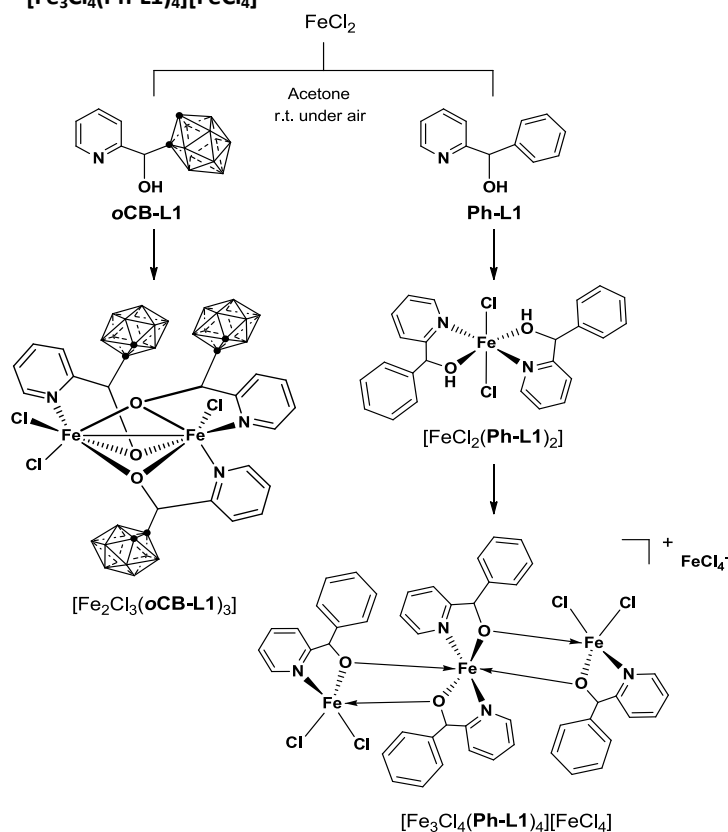
3.2.1.1. Synthesis of an *ortho*-Carborane-Based Complexes and Related Phenyl Derivative

The use of the *ortho*-carborane-based pyridylalcohol ligand (*o***CB-L1**) leads to the formation of an unique unsymmetric diiron (III) complex **FeCl₃(*o*CB-L1)₃** (see scheme 3.2-2) which is compared with the triiron (III) complex **[Fe₃Cl₄(Ph-L1)₄][FeCl₄]** that is formed when the conventional phenyl-pyridylalcohol (**Ph-L1**) ligand is used. The magnetic, chiroptical and nonlinear optical properties of **FeCl₃(*o*CB-L1)₃** have also been studied and will be discuss later in this chapter.
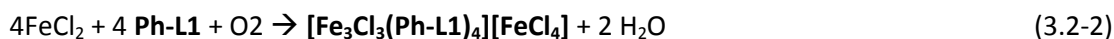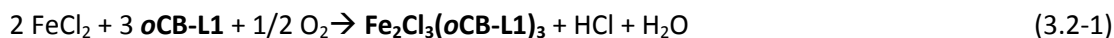
The general synthetic procedures are shown in Scheme **3.2-2**. The syntheses of all iron complexes were carried out under air. A clear yellowish golden solution was formed

Scheme 3.2-2: Formation route of Complexes **FeCl₃(*o*CB-L1)₃** and **[Fe₃Cl₄(Ph-L1)₄][FeCl₄]**

by mixing iron (II) dichloride (FeCl₂) with *o***CB-L1** in a 1.5:1 ratio in acetone. Slow evaporation of the acetone gave brownish yellow agglomerates **Fe₂Cl₃(*o*CB-L1)₃** in a quantitative yield. The same reaction was conducted with **Ph-L1**. A mononuclear iron (II) intermediate **FeCl₂(Ph-L1)₂** was observed in this case, followed by further conversion to a trinuclear iron (III) complex **[Fe₃Cl₃(Ph-L1)₄][FeCl₄]**, which is the most stable product as confirmed by a recent report.[6] All structures of iron complexes in scheme 3.2-2 were confirmed by single-crystal X-ray diffraction (XRD) measurements and the

purity was proven by elemental analysis and powder X-ray diffraction (PXRD). Equations (3.2-1) and (3.2-2) summarize the formation of these complexes, assuming that the atmospheric O_2 acts as oxidizing agent.

$$2\ FeCl_2 + 3\ \textbf{\textit{o}CB-L1} + 1/2\ O_2 \rightarrow \textbf{Fe}_2\textbf{Cl}_3(\textbf{\textit{o}CB-L1})_3 + HCl + H_2O \qquad (3.2\text{-}1)$$

$$4FeCl_2 + 4\ \textbf{Ph-L1} + O2 \rightarrow \textbf{[Fe}_3\textbf{Cl}_3(\textbf{Ph-L1})_4][\textbf{FeCl}_4] + 2\ H_2O \qquad (3.2\text{-}2)$$

The deprotonation of the corresponding alcohol ligands during the formation of these complexes, and in the absence of a base, can be explained by the hardness of the metal ion.[7] That is, the higher the hardness of the metal, the more the deprotonation of alcohols tends to occur upon coordination. Consequently, complexes of early transition metals (groups 4 – 6) exclusively contain the fully deprotonated alkoxide anions, while late transition metals (groups 9 – 12) usually coordinate to the fully protonated ligands. Group 7 and 8 transition metals

Figure 3.2-2: Molecular structure of **FeCl₂(Ph-L1)₂**. Color code: C grey; H white; O red; N light blue; Cl green; Fe orange.

are in an intermediate situation that the occurrence of the deprotonation of alcohols is the combined effect of hardness of the metal ion and the acidity of the alcohols. As expected, the acidity of the **oCB-L1** is higher than the **Ph-L1** due to the more electron-withdrawing character of the *o*-carboranyl than the phenyl moiety. This is proved indirectly by the isolated intermediate mononuclear iron (II) complex **FeCl₂(Ph-L1)₂** (Figure 3.2-2), in which the alcohol moieties remain protonated. However, during the formation of **FeCl₂(Ph-L1)₂**, no such intermediate was observed even by an in situ study under N_2 atmosphere by Cyclic Voltammetry and NMR spectroscopy, indicating the fast formation of the iron (III) compound.
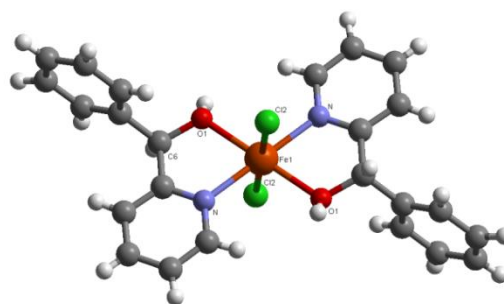
Two solvates were obtained by crystallization of complex **Fe₂Cl₃(oCB-L1)₃** in acetone or diethyl ether: an acetone solvate, **[Fe₂Cl₃(oCB-L1)₃]•acetone** and an ether solvate **[Fe₂Cl₃(oCB-L1)₃]•ether**. The corresponding structures were determined by single-crystal XRD. **[Fe₂Cl₃(oCB-L1)₃]•acetone** (Figure 3.2-3, left) and **[Fe₂Cl₃(oCB-L1)₃]•ether** (Figure 3.2-3, right) have the same arrangement of **oCB-L1** ligand, providing an unsymmetric dinuclear iron (III) complex.
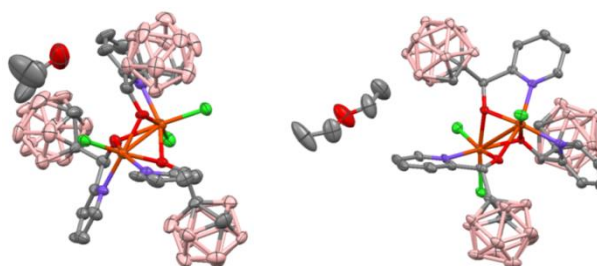

Figure 3.2-3: Ball and stick representation (Mercury 3.0) for molecular structure **[Fe₂Cl₃(oCB-L1)₃]•acetone** (left) and **[Fe₂Cl₃(oCB-L1)₃]•ether** (right). Color code: B pink; C grey; H white; O red; N light blue; Cl green; Fe orange.

It is known that the alcohol deprotonation in **L1** (Scheme 3.2-2) and its derivatives favour bridging ($\mu-\kappa^1(O)$: $\kappa^2(N,O)$) over chelating (N, OH) bonding modes which can foster the formation of polynuclear complexes. It is also known that the polynuclearity seems to be lowered by the addition of bulky substituents near

R = H, Ph (**FeCl₂(Ph-L1)₂**), 2-MeO-Ph   R = oCB-L1 (**Fe₂Cl₃(oCB-L1)₃**)

the alkoxide functional group.[8] An example was reported by Christou *et al.* where Mn clusters reduce their nuclearity from Mn_{16} to Mn_6 by increasing the bulkiness of the chelate ligands. This is one of the explanations to the formation of the dinuclear iron (III) complex **Fe₂Cl₃(oCB-L1)₃** against the trinuclear complex **[Fe₃Cl₃(Ph-L1)₄][FeCl₄]**. In addition, compare to the literature, diiron (III) complexes with **L1** ligands or its derivatives always contain an even number of alkoxide bridges (Scheme 3.2-3, left).[7,9] This is in contrast with complex **Fe₂Cl₃(oCB-L1)₃**, which contains three alkoxide bridges (Scheme 3.2-3, right), that is, an odd number of alkoxide bridges per diiron moiety. This unique formation can be interpreted by the combined effect of the higher acidity (alcohol functional group) and the bulky substituent (*o*-carboranyl) that makes the alkoxide ligand (*o*CB-L1⁻) less basic and less nucleophilic, consequently less coordinating at oxygen.[7] Therefore, an extra alkoxide bridge from the third *o*CB-L1 is needed to compensate the lack of electron densities in the metals.

As previously mentioned (section 3.1.1), the chiral pyridylalcohol ligand *o*CB-L1 can adopt an *R* or *S* configuration. Since the iron complex contains three *o*CB-L1 ligands, four configurations are possible: *RRR*, *SSS*, *RRS* and *SSR*. However, It was found that in complex **Fe₂Cl₃(oCB-L1)₃**, only *RRS* and *SSR* configurations are observed in the crystal structure represented in Figure 3.2-4. In order to further examine the formation of complex **Fe₂Cl₃(oCB-L1)₃** and the configuration of the ligands in the complex, the *R* and *S* enantiomers of *o*CB-L1 were separated by HPLC using chiral stationary phase

Figure 3.2-4: Fe₂Cl₃(*o*CB-L1)₃

(Chrialpak AZ-H) and hexane/ethanol 80/20 as eluent. Afterwards, it was followed the same synthetic procedure of complex **Fe₂Cl₃(oCB-L1)₃** (Scheme 3.2-2), but in this case by reacting FeCl₂ with controlled proportions of the enantiopure ligands (R)-(+)-*o*CB-L1/(S)-(-)-*o*CB-L1mixtures (1:0.5 equiv. or 0.5:1 equiv. per 1 equiv. of Fe) in acetone. In this way, the corresponding enantiopure complexes **Fe₂Cl₃(oCB-L1)₃** with *RRS* and *SSR* configurations, **Fe₂Cl₃((*RRS*)-oCB-L1)₃** and **Fe₂Cl₃((*SSR*)-oCB-L1)₃**, were obtained and the structures were confirmed by single-crystal XRD (Scheme 3.2-4).

Scheme 3.2-4: Synthetic route of enantiopure complexes **Fe₂Cl₃((RRS)-oCB-L1)₃** and **Fe₂Cl₃((SSR)-oCB-L1)₃**.
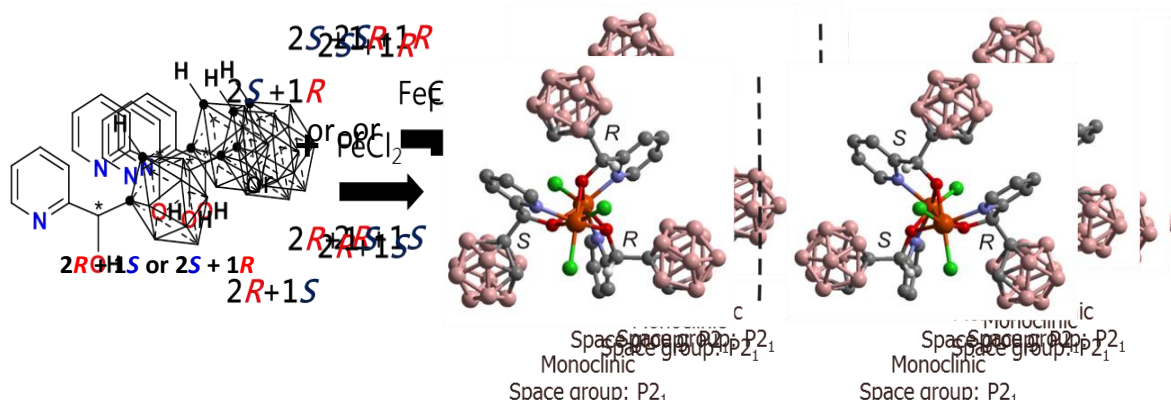
Further studies were carried out to verify whether the homochiral *RRR* or *SSS* complexes were possible. When only one of the enantiomers ((*R*)-(+)-*o*CB-L1 or (*S*)-(-)-*o*CB-L1) was reacted with FeCl₂ in a 1.5:1 ratio, the possible combination of complex **[Fe₂Cl₃(oCB-L1)₃]** in *RRR* and *SSS* configurations could not be formed. Instead, a dinuclear **[Fe₂Cl₂((RR)-oCB-L1)₂]•acetone** and a mononuclear **Fe((SSS)-oCB-L1)₃** were found and characterized by XRD (Figure 3.2-5). Comparison of the PXRD data of the simulated pattern from the structures of complexes **[Fe₂Cl₂((RR)-oCB-L1)₂]•acetone** and **Fe((SSS)-oCB-L1)₃** (Figure 3.2-5a and Figure 3.2-5c) and the experimental pattern of the reaction mixture (Figure 3.2-5b) confirmed that the final products of the reactions contain the mixture of both complexes.
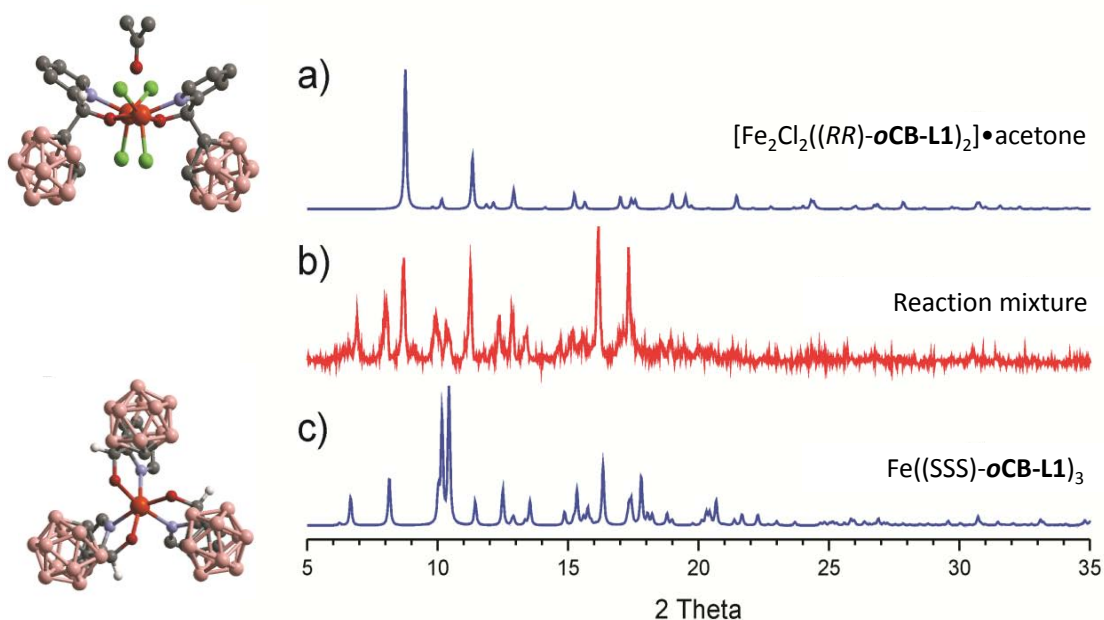
Figure 3.2-5: Comparison of PXRD of a) calculated PXRD of complex **[Fe₂Cl₂((RR)-oCB-L1)₂]•acetone** from the structure (left), b) experimental PXRD for the reaction mixture and c) calculated PXRD of complex **Fe((SSS)-oCB-L1)₃** and the corresponding structure (left). X-ray structures are shown in ball and stick representation (Mercury 3.0). Color code: B pink; C grey; H white; O red; N light blue; Cl green; Fe orange.

It is therefore proved that only *RRS* and *SSR* configurations of the complex **Fe₂Cl₃(*o*CB-L1)₃** can be formed, but not *RRR* and *SSS*, which maybe due to the steric hindrance of the *ortho*-carborane moiety in the **oCB-L1** ligand. Besides, it is worth notice that in complex **[Fe₂Cl₂((*RR*)-*o*CB-L1)₂]•acetone**, a symmetrical dinuclear iron (III) complex was formed with two **oCB-L1⁻** with a $\mu-\kappa^1(O):\kappa^2(N,O)$ bonding mode, and a solvated acetone molecule is interacting with the iron (III) centers as η^1-O coordination, which is known for electron-deficient metals.[10] This result supports the interpretation of the poor nucleophilic property of the alkoxide ligand **oCB-L1⁻** that drives to the formation of the three-alkoxide bridges in complex **Fe₂Cl₃(*o*CB-L1)₃** or the η^1-O coordination in complex **[Fe₂Cl₂((*RR*)-*o*CB-L1)₂]•acetone** to compensate the electron densities in the electron deficient metals.

3.2.1.2. Characterizations and Properties

The unsymmetric nature of the iron (III) complex and the possibility to obtain it in enantiopure form is interesting to further study its properties, both in solution (Cyclic voltammetry, NMR spectroscopy, UV-Vis spectrometry and chiroptical) and solid state (Magnetic and non-linear optic properties).

Cyclic Voltammetry

- 0.74

Figure 3.2-6: Cyclic votammetry (CV; a), E in mV) and square wave voltammetry (SWV; b and c) of complex **Fe₂Cl₃(*o*CB-L1)₃** at 100 mV⁻¹ in dry acetonitrile. Plots versus Ag wire; the ferrocene couple was measured at +0.220 V versus this reference under the same conditions.

The cyclic voltammogram (CV) and the square wave voltammograms (SWV) of this unsymmetric complex **Fe$_2$Cl$_3$(*o*CB-L1)$_3$** were measured in acetonitrile (Figure 3.2-6). Three quasi-reversible redox processes were observed at (I) +0.07 to −0.04, (II) −0.49 and (III) −0.74V. Process (I) is attributed to the successive one-electron redox couples: $2Fe^{III} + 1e^- \rightarrow Fe^{II}Fe^{III}$ and $Fe^{II}Fe^{III} + 1e^- \rightarrow 2Fe^{II}$. The reduction SWV plot shows a broad band at +0.07, consistent with the two iron centers with different environments reducing at slightly different voltage (c.a. +0.06 V difference). The low current intensity processes (II) and (III) suggests a partial decomposition take place after reduction of both iron (III) sites. The signal at process (IV) (+0.52 V) is attributed to species formed during reduction. This is supported by the SWV plot which shows no signal during reduction (Figure b) but is observed in the oxidation plot (Figure c). Overall, the CV for complex **Fe$_2$Cl$_3$(*o*CB-L1)$_3$** agrees with a dinuclear nature for the complex and it is in accordance with the solid state structure.

NMR Spectroscopy

Solution ^{1}H and ^{11}B NMR spectra show that the sharp signals from the ligand became broad after the addition of FeCl$_2$. The broadening of the signals indicate the formation of paramagnetic iron (III) centres in complex **Fe$_2$Cl$_3$(*o*CB-L1)$_3$** (Figure 3.2-7). Since the pyridine ring is closer to the paramagnetic iron centre than the carborane cluster in the complex **Fe$_2$Cl$_3$(*o*CB-L1)$_3$**, the interference by the paramagnetic iron (III) centre is larger to the proton resonances of the pyridine ring than the boron atoms of the carborane. Therefore, the ^{1}H NMR signals are generally broader than the ^{11}B NMR signal.
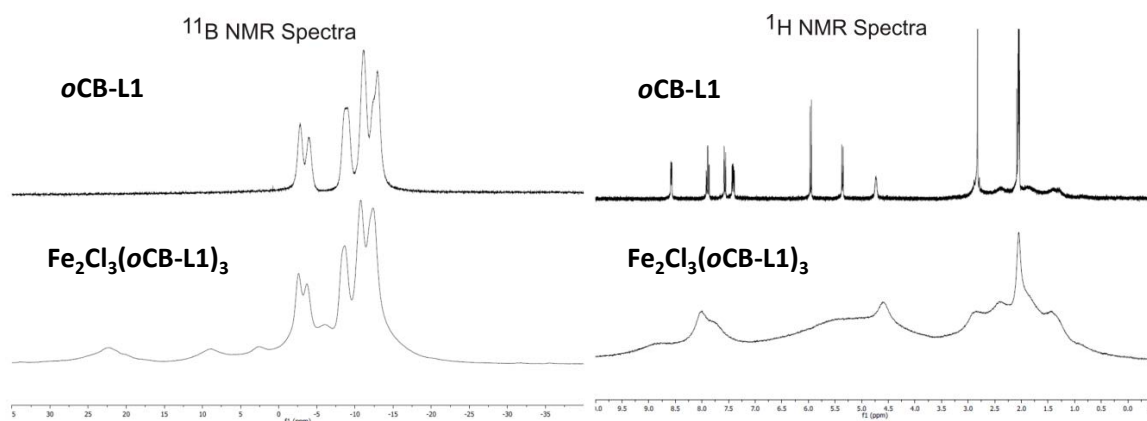
Figure 3.2-7: Comparison between ^{1}H NMR (top) and ^{11}B NMR (bottom) spectra for the *o*CB-L1 ligand and the iron (III) complex **Fe$_2$Cl$_3$(*o*CB-L1)$_3$** in acetone-D$_6$.

Magnetic Properties

The magnetic properties of complex **Fe$_2$Cl$_3$(*o*CB-L1)$_3$** in solid state were studied. The variable-temperature (2-300 K) magnetic susceptibility data of the bulk solid complex **Fe$_2$Cl$_3$(*o*CB-L1)$_3$** was collected under 0.03 and 0.5 T external magnetic fields (Figure 3.2-8). The result shows complex **Fe$_2$Cl$_3$(*o*CB-L1)$_3$** is an antiferromagnetic species (χ_MT is 7.50 cm^{3}mol^{-1}K at 300 K and decreases while lowering the temperature). The lower χ_MT value of complex **Fe$_2$Cl$_3$(*o*CB-L1)$_3$** compare to the two

independent high-spin iron (III) centers ($\chi_M T$ = 8.75 cm^{3}mol^{-1}K; g = 2.00) is an evidence of the antiferromagnetic interaction. Magnetic susceptibility data were analyzed using the Van Vleck equation, derived from the spin exchange Hamiltonian $H = -JS_1S_2$,[11] where $S_1 = S_2 = 5/2$. The best fit matches well with the experimental data and gives the following values: g = 2.05, J = -10.22, TIP = 280 × 10^{-6} cm^{3}mol^{-1}, ρ = 0.05 % and R = 1×10^{-5}. Overall, the analysis of the data agreeswith the shapeand values observed in the experimental measurement, in

Figure 3.2-8: Fitting of the $\chi_M T$ versus T of *rac*-**Fe$_2$Cl$_3$(*o*CB-L1)$_3$** between 2 and 300 K. The experimental data are shown as ∎ and − corresponds to the fitting values

which the exchange coupling for both iron (III) atomsis significantly antiferromagnetic. DFT calculation using the B3LYP functions was processed and in agreement with the experimental data, giving a calculated J value of -6.0 cm^{-1}. Although there is lack of correlated complexes to establish a clear magnetostructural correlation, the analysis of the structural parameters of the relevant complexes show the Fe-O-Fe angles are similar but difference in the Fe-O distances, suggesting the Fe-O distance could be the key parameter to control the magnetic behavior. That is, the longest Fe-O separation in the complex **Fe$_2$Cl$_3$(*o*CB-L1)$_3$** compare to other complexes seems to explain the antiferromagnetic coupling in this system.

UV-Vis Spectrometry

The UV-Vis spectrum of the complex **Fe$_2$Cl$_3$(*o*CB-L1)$_3$** and the ligand *o*CB-L1 were recorded in acetonitrile (Figure 3.2-9). Only one band is observed for the ligand *o*CB-L1 near 260 nm, while two bands can be observed for the complex **Fe$_2$Cl$_3$(*o*CB-L1)$_3$** near 250 nm and 320 nm. According to the literature, the absorption bandaround 250 nm can be attributed to the $\pi \rightarrow \pi^*$ transition of the ligand *o*CB-L1, and the band at 320 nm can be attributed to *o*CB-L1$^-$ $\rightarrow$ Fe (III) charge transfer transitions (LMCT).[12]
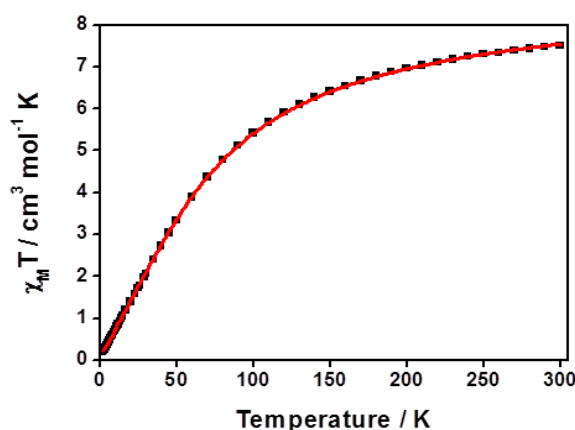

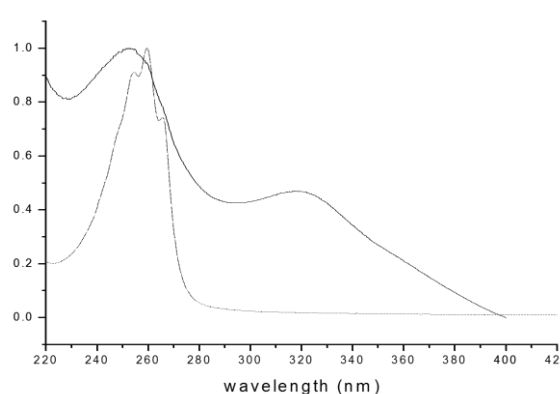**Figure 3.2-9**: UV-Vis absorption spectra (normalized) of *o*CBhmpH (dotted line) and complex **Fe$_2$Cl$_3$(*o*CB-L1)$_3$**(solid line) in acetonitrile.

Chiroptical Properties

The circular dichroism (CD) spectra of the enantiopure complexes (*RRS*)-(-)-**Fe₂Cl₃(*o*CB-L1)₃** and (*SSR*)-(+)-**Fe₂Cl₃(*o*CB-L1)₃** as well as the corresponding free enantiopure ligands (R)-(+)-***o*CB-L1**/(S)-(-)-***o*CB-L1** were recorded (Figure 3.2-10) in CH₂Cl₂. Both enantiopure ligands and complexes show mirror images. The bands at 260 nm with $\Delta\varepsilon$ value -9.3 M⁻¹ cm⁻¹ for the ligand (Figure 3.2-10, dotted line) is typical for chiral secondary alcohols with an aromatic substituent.[10,13] In the case of the iron (III) complexes (*RRS*)-(-)- **Fe-*o*CB-L1-a** and (*SSR*)-(+)-**Fe₂Cl₃(*o*CB-L1)₃**, the bands at 260 nm, 310 nm and 350 nm display as mirror images (Figure 3.2-10, solid line), revealed the chiral environment around the iron centres and suggest the chirality is transferred from the chiral ligands to the corresponding complexes.
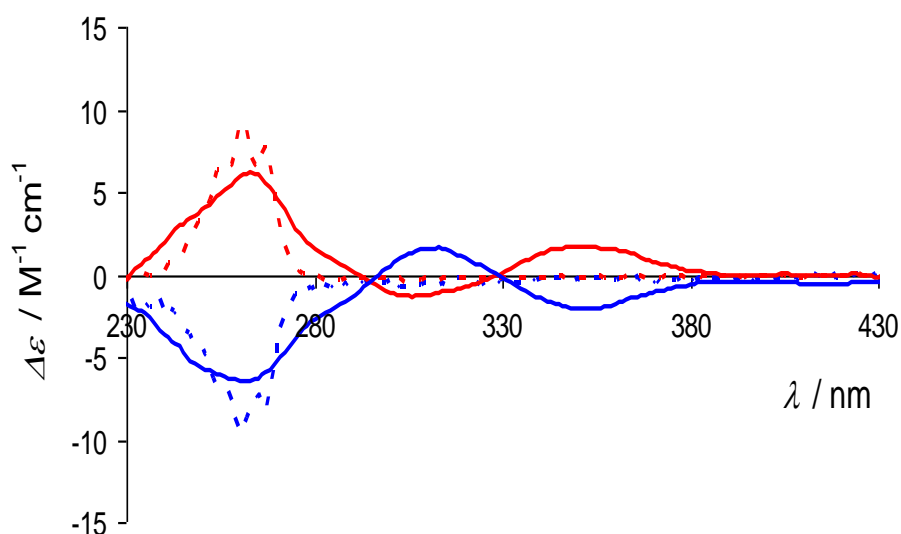

Figure 3.2-10: CD spectra of *R*(+)**oCB-L1** (blue dotted line), *S*(–)**oCB-L1** (red dotted line), (*RRS*)-(-)-**Fe₂Cl₃(*o*CB-L1)₃** (blue plain line) and(*SSR*)-(+)- **Fe₂Cl₃(*o*CB-L1)₃** (red plain line).

Spontaneous Resolution and Non-linear Optical (NLO) Properties

As mentioned before, two different solvates (**Fe₂Cl₃(*o*CB-L1)₃•acetone** and **Fe₂Cl₃(*o*CB-L1)₃•ether**, Figure 3.2-11) were obtained. **Fe₂Cl₃(*o*CB-L1)₃•acetone** (space group: centrosymmetric P2₁/*c*) is formed as a racemate (*rac*-**Fe₂Cl₃(*o*CB-L1)₃**), which means both enantiomers ((*RR*)-Fe:(*S*)-Fe and (*SS*)-Fe: (*R*)-Fe, Figure 3.2-11 left) crystalized in the same crystal. **Fe₂Cl₃(*o*CB-L1)₃•ether** (space group: non-centrosymmetric P2₁, Flack parameter: 0.004(15)[14]) is obtained as a conglomerate (*co*-**Fe₂Cl₃(*o*CB-L1)₃**), that is, the enantiomers ((*RR*)-Fe:(*S*)-Fe or (*SS*)-Fe:(*R*)-Fe, Figure 3.2-11 right) crystalized in separated crystals. The formation of *co*-**Fe₂Cl₃(*o*CB-L1)₃** indicates that during the recrystallization process, the spontaneous resolution occurs, or in other words, the immediate separation of the corresponding enantiomers from the racemic mixtures on crystallization.

Since the loss of centrosymmetry of the material could give interesting optical and electrical properties,[15] further investigationon whether spontaneous resolution and conglomerate formation were possible in the entire crystalline batch (bulk solid) was carried out.

Fe₂Cl₃(*o*CB-L1)₃•acetone   **Fe₂Cl₃(*o*CB-L1)₃•**ether

rac-**Fe₂Cl₃(*o*CB-L1)₃**   *co*-**Fe₂Cl₃(*o*CB-L1)₃**

(*RR*)Fe:(*S*)Fe + (*SS*)Fe:(*R*)Fe

(*RR*)Fe:(*S*)Fe and (*SS*)Fe:(*R*)Fe
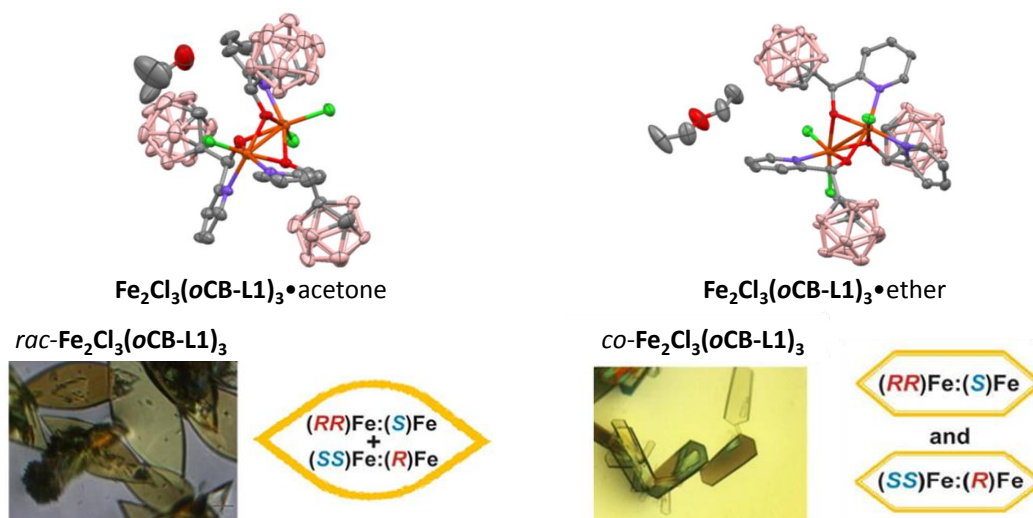
Figure 3.2-11: Single crystal structures of **Fe₂Cl₃(*o*CB-L1)₃•acetone** and illustration of racemate (left) and **Fe₂Cl₃(*o*CB-L1)₃•ether** and illustration of conglomerate (right). Yellow line shapes represent one crystal.

The slow evaporation of acetone for complex **Fe₂Cl₃(*o*CB-L1)₃** (Figure 3.2-12A) gave a crystalline solid that is isomorphous with **Fe₂Cl₃(*o*CB-L1)₃•acetone** by comparison of the PXRD patterns (Figure 3.2-12B (a) and (b)).
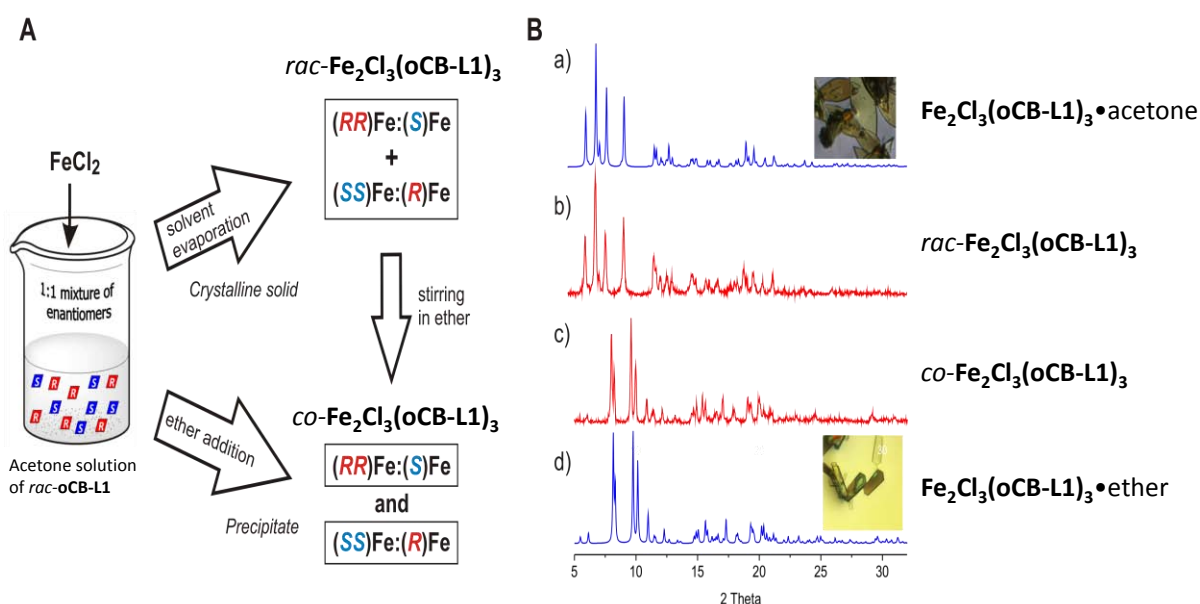
Figure 3.2-12: **A**: Schematic representation of racemic (*rac*-**Fe₂Cl₃(*o*CB-L1)₃**) and conglomerate (*co*-**Fe₂Cl₃(*o*CB-L1)₃**) formation for bulk samples of **Fe₂Cl₃(*o*CB-L1)₃**. See the text for details; **B**: PXRD of **Fe₂Cl₃(*o*CB-L1)₃**: a) calculated PXRD obtained from crystal structure **Fe₂Cl₃(*o*CB-L1)₃·acetone**, b) racemic mixture *rac*-**Fe₂Cl₃(*o*CB-L1)₃**, c) conglomerate *co*-**Fe₂Cl₃(*o*CB-L1)₃**, d) calculated XRPD obtained from crystal structure **Fe₂Cl₃(*o*CB-L1)₃·ether.**

Addition of diethyl ether to the solution of *rac*-**Fe₂Cl₃(*o*CB-L1)₃** in acetone provoked the formation of a precipitate (virtually no material remain in the solution) which PXRD pattern shows that it is

isomorphous with **Fe$_2$Cl$_3$(oCB-L1)$_3$•ether** (Figure 3.2-12B (c) and (d)). Therefore, the solid obtained on precipitation corresponds to a conglomerate co-**Fe$_2$Cl$_3$(oCB-L1)$_3$**.

Moreover, the conversion of rac-**Fe$_2$Cl$_3$(oCB-L1)$_3$** to co-**Fe$_2$Cl$_3$(oCB-L1)$_3$** in the solid state was also demonstrated experimentally by exposing rac-**Fe$_2$Cl$_3$(oCB-L1)3** crystalline solid to diethyl ether vapour for 3 days. The resulting solid was measured by PXRD and the experimental diffraction patterns matched with the calculated diffraction patterns from the single-crystal X-ray structure as well. Thus, the total spontaneous resolution in the entire crystalline batches from the racemate compounds to conglomerate, either on precipitation by addition of diethyl ether solvent or exposition to its vapour, is confirmed.

The chiral nature of the conglomerate co-**Fe$_2$Cl$_3$(oCB-L1)$_3$** was further confirmed by measuring its nonlinear optical activity by using second-harmonic generation (SHG) measurements. The SHG method is commonly applied to identify the formation of conglomerates.[16] The results show a positive SHG signal of complex co-**Fe$_2$Cl$_3$(oCB-L1)$_3$** that is in agreement with its non-centrosymmetric nature (chiral space group P2$_1$; Figure 3.2-13). The SHG signal maintains up to 110 ^{o}C exhibits the stability of co-**Fe$_2$Cl$_3$(oCB-L1)$_3$** under laser irradiation is also observed. Additionally, the CD spectrum shows no signal in solution implying that the co-**Fe$_2$Cl$_3$(oCB-L1)$_3$** contains a 1:1 mixture of the enantiomers. All data is consistent with the formation of conglomerate co-**Fe$_2$Cl$_3$(oCB-L1)$_3$**.
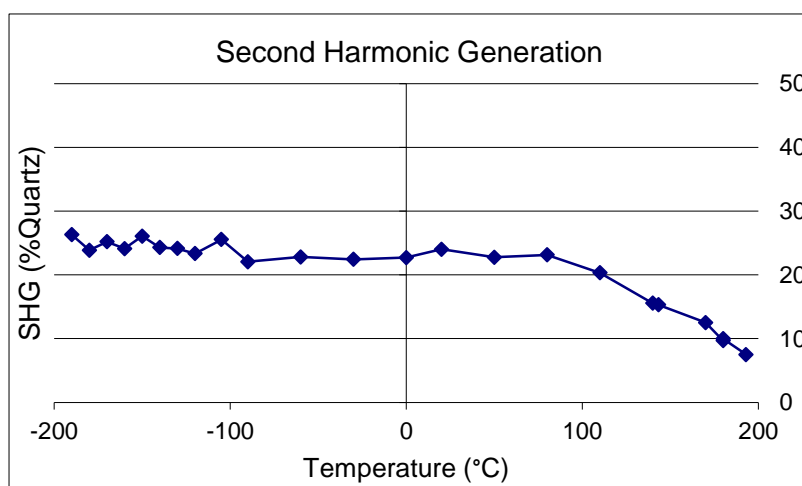
Figure 3.2-13: SHG intensity of co-**Fe$_2$Cl$_3$(oCB-L1)$_3$** versus temperature between -200 and 200 ^{o}C.

The study of the **oCB-L1** and its comparison with the **Ph-L1** highlights the unprecedented properties from the carborane moiety versus the conventional organic based moiety in coordination chemistry. In order to understand more the role of the carborane and the driving factors of such unique complex formation in this system, the $meta$-carborane derivative **mCB-L1** has also been synthesized (Chapter 3.1.1.1). The reactivity of **mCB-L1** toward FeCl$_2$ will be explained in the following section.

3.2.1.3. Syntheses of *meta*-Carborane-Based Complexes

The size of both carboranyl pyridylalcohols **oCB-L1** and **mCB-L1** are very similar, the main difference being their acidities.[17] As explained in the Introduction (Chapter 1.1.1), *o*-carborane will exert a higher electron-withdrawing effect on substituents at carbon than the related *m*-carborane. Thus, it results interesting to compare the coordination chemistry of **oCB-L1** and **mCB-L1** and investigate the possible effect of their different acidities on their coordination chemistry. Thus, the same synthetic procedure as complex **Fe₂Cl₃(oCB-L1)₃** has been used (Scheme 3.2-5). A clear yellow solution was formed by mixing iron (II) dichloride (FeCl₂) with **mCB-L1** in a 1.5:1 ratio in acetone. Slow

Scheme 3.2-5: Synthesis of complexes **[Fe₂Cl₃(oCB-L1)₃]** and **[Fe₂Cl₃(mCB-L1)₃]**

[Fe₂Cl₃(oCB-L1)₃]   [Fe₂Cl₃(mCB-L1)₃]

evaporation of the acetone gave a yellow crystalline solid that corresponds to **Fe₂Cl₃(mCB-L1)₃** in a quantitative yield (scheme 3.2-5, right). The structure of complex **Fe₂Cl₃(mCB-L1)₃** is confirmed by single-crystal XRD and the phase purity is proven by the PXRD. Unexpectedly, unlike in *o*-carborane complex **Fe₂Cl₃(oCB-L1)₃**, an isomeric dinuclear iron (III) complex is obtained when using **mCB-L1**. The pyridine nitrogens of three **mCB-L1** ligands are coordinated to only one of the iron (III) ions in **Fe₂Cl₃(mCB-L1)₃**. As it can be seen in the Scheme 3.2-5, the same as **oCB-L1**, **mCB-L1** also adopts *R* and *S* configuration. Different than the **Fe₂Cl₃(oCB-L1)₃** complex, where only *RRS* and *SSR* configurations are found, **mCB-L1** ligands in complex **Fe₂Cl₃(mCB-L1)₃** are found in *RRR* and *SSS* configurations. At this point, it is vital to remind that **[Fe₂Cl₂((RR)-oCB-L1)₂]•acetone** or **[Fe((SSS)-oCB-L1)₃]** were formed when only one of the **oCB-L1** enantiomers (*R* or *S*) were employed in the synthesis (Figure 3.2-5; section 3.2.1.1). The construction of **Fe₂Cl₃(mCB-L1)₃** could then be explained by preferential formation of a mononuclear **[Fe(mCB-L1)₃]** in solution, followed by its coordination to FeCl₃ that present in the reaction media. Following the same interpretation employed in the case of the **Fe₂Cl₃(oCB-L1)₃** complex, the **mCB-L1** is expected to be less acidic than the related **oCB-L1**, therefore, the corresponding alkoxide ligand **mCB-L1⁻** should bemore basic and consequently more coordinating than the **oCB-L1** derivative. This might certainly explain a higher stability of a mononuclear complex like **Fe(mCB-L1)₃**, that then reacts or just crystallized with FeCl₃. Unfortunately, the presence of the paramagnetic iron (III) species inhibited the analysis by NMR spectroscopy. Thus, a family of **mCB-L1** derivatives is set to be synthesized, where the electron-withdrawing nature of the cluster and therefore the acidity of the alcohols substituent can
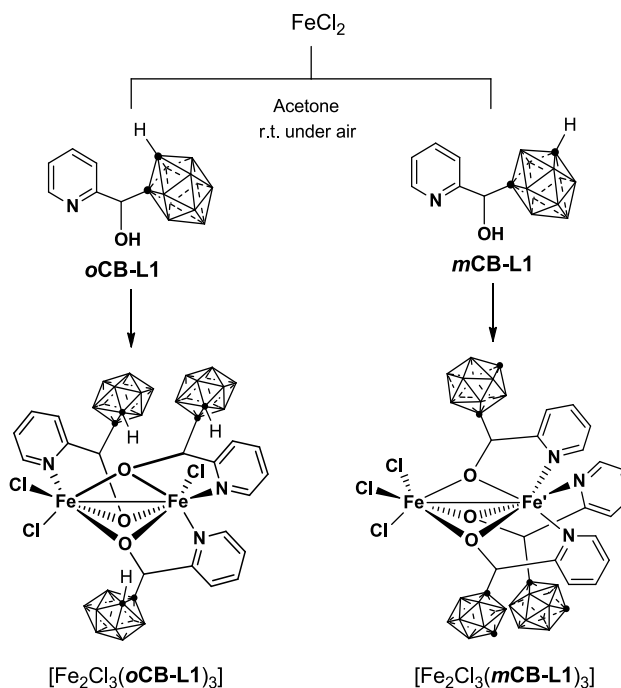
be changed, in order to further investigate the acidity in the **CB-L1** system towards the formation of the dinuclear iron (III) complex. As previously described in section 3.1.1.1, a series of B-iodinated **mCB-L1** derivatives (**I-mCB-L1** and **I$_2$-mCB-L1**) were synthesized by substituting the hydride (H⁻) to iodide (I⁻) at B(9) or/and B(10) position(s), since the introduction of an electron-withdrawing group such as iodine in such positions is known to exert an influence in the cluster carbon atoms.[18]

An indirect proof of the changes of acidity of the alcohol in the **CB-L1** system can be observed by NMR spectroscopy under the same condition (5 mg/0.3 mL Ac-D$_6$ solvent, room temperature) (Figure 3.2-14), The highlighted signals in the ¹H NMR spectra of **oCB-L1**, **mCB-L1**, **I-mCB-L1** and **I$_2$-mCB-L1** correspond to the proton of the alcohol (-OH). As shown in the spectra, the -OH proton signal of **oCB-L1** appears at 5.97 ppm, whereas the corresponding -OH proton signal of **mCB-L1**, **I-mCB-L1** and **I$_2$-mCB-L1** appear 5.45 ppm, 5.64 ppm and 5.80 ppm, respectively. Within the **mCB** series, the OH proton signal is more downfield shifted as more iodines are introduced in the cluster. Since the electron density of the alcohol would be reduced by the more electron-withdrawing moieties, the proton from the alcohol would be more deshielded and resulting in the more downfielded chemical shift.
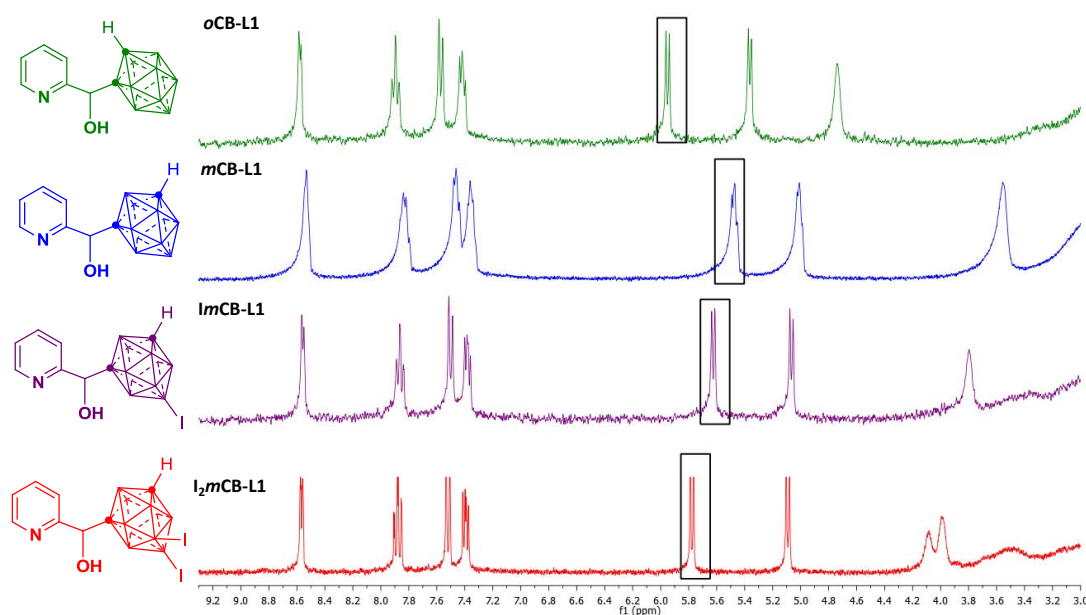
Figure 3.2-14: Comparison between ¹H NMR spectra for the **oCB-L1** (green), **mCB-L1** (blue), **I-mCB-L1**(purple) and **I$_2$-mCB-L1** (red) ligands in acetone-D$_6$.

The corresponding iron (III) complexes with **I-mCB-L1** and **I$_2$-mCB-L1** ligands were synthesized following the same reaction procedure as complex **Fe$_2$Cl$_3$(mCB-L1)$_3$**. Slow evaporation of the acetone gave yellowish brown amorphous solid **Fe$_2$Cl$_3$(I-mCB-L1)$_3$** and **Fe$_2$Cl$_3$(I$_2$-mCB-L1)$_3$**, in which the proposed formulas are in agreement with the elemental analyses. In the ¹H NMR spectra (Figure 3.2-15), although the paramagnetic properties of the complexes causes the broadening of the signals, it is clear that the spectra of **Fe$_2$Cl$_3$(mCB-L1)$_3$**, **Fe$_2$Cl$_3$(I-mCB-L1)$_3$** and **Fe$_2$Cl$_3$(I$_2$-mCB-L1)$_3$** are comparable. Therefore, both formation of the complexes **Fe$_2$Cl$_3$(I-mCB-L1)$_3$** and **Fe$_2$Cl$_3$(I$_2$-mCB-L1)$_3$**

are suggested to have the same architecture as complex **Fe$_2$Cl$_3$(*m*CB-L1)$_3$** rather than complex **Fe$_2$Cl$_3$(*o*CB-L1)$_3$** (scheme 3.2-5).
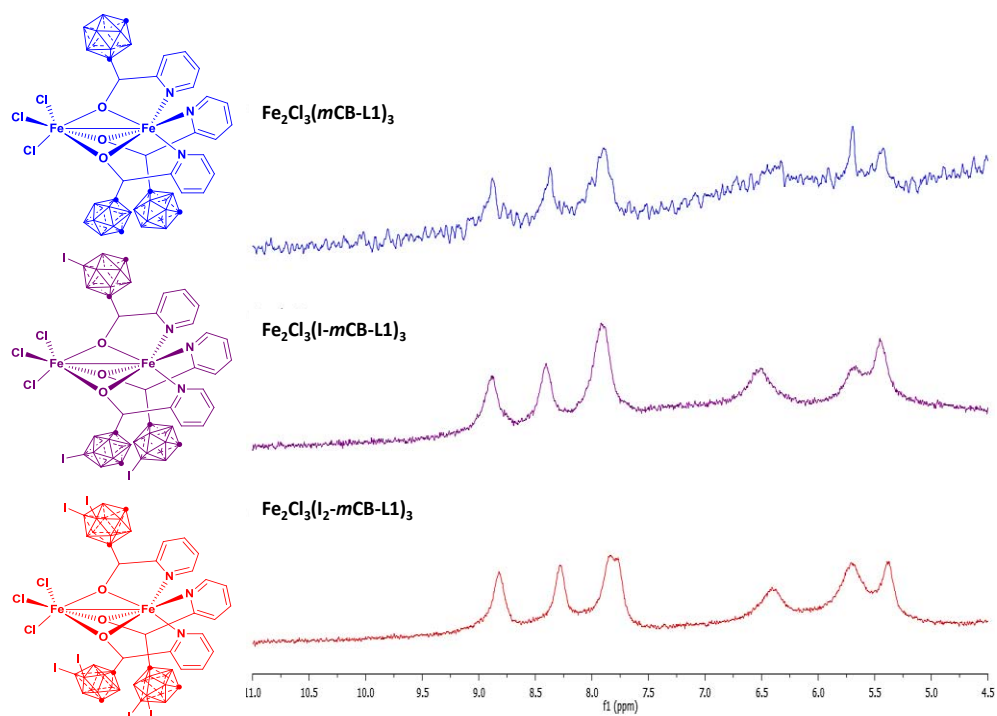
Figure 3.2-15: ^{1}H NMR spectra for the corresponding complex **Fe$_2$Cl$_3$(*m*CB-L1)$_3$** (blue), **Fe$_2$Cl$_3$(I-*m*CB-L1)$_3$** (purple) and **Fe$_2$Cl$_3$(I$_2$-*m*CB-L1)$_3$** (red) ligands in acetone-D$_6$.

In order to shed more light into the coordination mode of the series of **mCB-L1** ligands, the iron complexes were also characterized by Cyclic Voltammetry (CV) and UV-visible spectroscopy. The preliminary voltammograms of complexes **Fe$_2$Cl$_3$(*m*CB-L1)$_3$**, **Fe$_2$Cl$_3$(I-*m*CB-L1)$_3$** and **Fe$_2$Cl$_3$(I$_2$-*m*CB-L1)$_3$** were determined under the same conditions (0.85 mM complexes in TBAPF6 acetonitrile solution with 100 mV^{-1} scan rates) and compare with complex **Fe$_2$Cl$_3$(*o*CB-L1)$_3$**. Similar voltammograms are observed for complexes **Fe$_2$Cl$_3$(*m*CB-L1)$_3$**, **Fe$_2$Cl$_3$(I-*m*CB-L1)$_3$** and **Fe$_2$Cl$_3$(I$_2$-*m*CB-L1)$_3$**. As shown in the voltammograms (Figure 3.2-16), only one quasi-reversible redox process was observed for complexes **Fe$_2$Cl$_3$(*m*CB-L1)$_3$**, **Fe$_2$Cl$_3$(I-*m*CB-L1)$_3$** and **Fe$_2$Cl$_3$(I$_2$-*m*CB-L1)$_3$**, whereas in the quasi-reversible redox process (I) of complex **Fe$_2$Cl$_3$(*o*CB-L1)$_3$**, two waves was observed during reduction process as explained previously. Although **Fe$_2$Cl$_3$(*m*CB-L1)$_3$**, **Fe$_2$Cl$_3$(I-*m*CB-L1)$_3$** and **Fe$_2$Cl$_3$(I$_2$-*m*CB-L1)$_3$** are also asymmetric iron (III) complexes, there is no obvious wave splitting observed during the reduction processes, which may due to instabilityof the complexes **Fe$_2$Cl$_3$(*m*CB-L1)$_3$**, **Fe$_2$Cl$_3$(I-*m*CB-L1)$_3$** and **Fe$_2$Cl$_3$(I$_2$-*m*CB-L1)$_3$**in acetonitrile (ACN) and resulting in split of complexes to a mono-nuclear complex **Fe(mCB-L1)$_3$** and FeCl$_3$, as previously hypothesized. The observed CV signals for the **mCB**-basedcomplexes are certainly compatible with such mononuclear complex formation in solution.

Fe$_2$Cl$_3$(*o*CB-L1)$_3$ Fe$_2$Cl$_3$(*m*CB-L1)$_3$

Fe$_2$Cl$_3$(I-*m*CB-L1)$_3$ Fe$_2$Cl$_3$(I$_2$-*m*CB-L1)$_3$
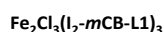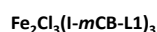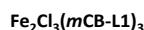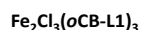
Figure 3.2-16: Cyclic voltammograms (CV) of complex **Fe$_2$Cl$_3$(*o*CB-L1)$_3$, Fe$_2$Cl$_3$(*m*CB-L1)$_3$, Fe$_2$Cl$_3$(I-*m*CB-L1)$_3$** and **Fe$_2$Cl$_3$(I$_2$-*m*CB-L1)$_3$** at 100 mV^{-1}scan rates in dry acetonitrile TBAPF$_6$ solution. Plots versus Ag wire; the ferrocene couple was measured at +0.220 V for complex **Fe$_2$Cl$_3$(*o*CB-L1)$_3$** and +0.430 V for complex **Fe$_2$Cl$_3$(*m*CB-L1)$_3$, Fe$_2$Cl$_3$(I-*m*CB-L1)$_3$** and **Fe$_2$Cl$_3$(I$_2$-*m*CB-L1)$_3$** versus this reference under the same conditions.

Moreover, a slight shift of the cathodic peaks for complexes **Fe$_2$Cl$_3$(*m*CB-L1)$_3$, Fe$_2$Cl$_3$(I-*m*CB-L1)$_3$** and **Fe$_2$Cl$_3$(I$_2$-*m*CB-L1)$_3$** to more positive potentials are observed (Figure 3.2-17), where the E$_{1/2}$ are +4.25, +6.75 and +9.25 mV vs Fc$^+$/Fc, respectively. Although the shift is not significant (±2.5 mV), it can be observed some influence of the ligands towards the electron density of the metal centers. The displacement of E$_{1/2}$ towards more positive potentials is consistent with the electron-withdrawing nature of the ligands (**I$_2$-*m*CB-L1** > **I-*m*CB-L1** > **mCB-L1**). The more elctron-withdrawing the ligands, the easier is the oxidation of the corresponding iron complexes:[19]

Figure 3.2-17: CV of complex **Fe$_2$Cl$_3$(*m*CB-L1)$_3$, Fe$_2$Cl$_3$(I-*m*CB-L1)$_3$** and **Fe$_2$Cl$_3$(I$_2$-*m*CB-L1)$_3$**in the range of +500 to -500 mV.

Fe$_2$Cl$_3$(I$_2$-*m*CB-L1)$_3$) > Fe$_2$Cl$_3$(I-*m*CB-L1)$_3$ > (Fe$_2$Cl$_3$(*m*CB-L1)$_3$.
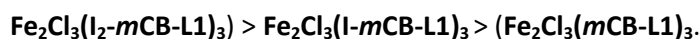
The UV-Vis spectra of complex **Fe₂Cl₃(mCB-L1)₃**, **Fe₂Cl₃(I-mCB-L1)₃** and **Fe₂Cl₃(I₂-mCB-L1)₃** were collected and compared with that for complex **Fe₂Cl₃(oCB-L1)₃** and iron trichloride (FeCl₃•xH₂O) as well (Figure 3.2-18). The UV-Vis spectra of complexes **Fe₂Cl₃(mCB-L1)₃**, **Fe₂Cl₃(I-mCB-L1)₃** and **Fe₂Cl₃(I₂-mCB-L1)₃** are similar with each other, indicating the electronic features of the complexes are comparable. Those are however different to that of **Fe₂Cl₃(oCB-L1)₃**. For all **Fe₂Cl₃(mCB-L1)₃**, **Fe₂Cl₃(I-mCB-L1)₃** and **Fe₂Cl₃(I₂-mCB-L1)₃** complexes, three bands at 250 nm, 320 nm and 360 nm are observed, while only two bands are observed for **Fe₂Cl₃(oCB-L1)₃** complex. Same as complex **Fe₂Cl₃(oCB-L1)₃**, the bands near 250 nm can be attributed to the $\pi \rightarrow \pi^*$ transition of the ligands **CB-L1**. The bands around 320 nm are assigned to **CB-L1**⁻ $\rightarrow$ Fe (III) ligand-to-metal charge transfer transitions (LMCT) for complexes **Fe₂Cl₃(mCB-L1)₃**, **Fe₂Cl₃(I-mCB-L1)₃** and **Fe₂Cl₃(I₂-mCB-L1)₃**. Interestingly, the band near 360 nm that appears in complexes **Fe₂Cl₃(mCB-L1)₃**, **Fe₂Cl₃(I-mCB-L1)₃** and **Fe₂Cl₃(I₂-mCB-L1)₃** also appears in the UV-spectrum of FeCl₃ (both in CH₃CN (360 nm) and CH₂Cl₂ (350 nm)). Those low energy bands are therefore tentatively assigned to Cl⁻ $\rightarrow$ Fe (III) LMCT from FeCl₃ units, although further investigation by gas phase calculation is necessary in order to confirm the band assignments. This result is in agreement with the earlier hypothesis where the **mCB**-based dinuclear iron (III) complexes split in solution into mononuclear iron (III) complexes and FeCl₃. This will certainly explain the differences of CV and UV results between **mCB** and **oCB**-based iron complexes.

Figure 3.2-18: UV-Vis absorption spectra (normalized) of FeCl₃ (dotted line), complex **Fe₂Cl₃(oCB-L1)₃** (solid line, green), **Fe₂Cl₃(mCB-L1)₃** (solid line, blue), **Fe₂Cl₃(I-mCB-L1)₃** (solid line, purple) and **Fe₂Cl₃(I₂-mCB-L1)₃** (solid line, red) in acetonitrile.

All the characterizations of complexes **Fe$_2$Cl$_3$(I-mCB-L1)$_3$** and **Fe$_2$Cl$_3$(I$_2$-mCB-L1)$_3$** implied that the same isomer as complex **Fe$_2$Cl$_3$(mCB-L1)$_3$** is formed, at least in solution. Unfortunately none of the iodo-derivatives could be crystallized so that it is not possible at this moment to verify the solid state structures. Providing that the analysis is correct and that all **mCB**-based iron (III) complexes correspond to mononuclear **Fe(mCB-L1)$_3$** complexes in solution, the basicity of the ligands might explain the differences with the related **oCB** complex. However, the effect of the size of the ligands in the architectures of the complexes cannot be ruled out. Nevertheless, the complexity of this chemistry certainly requires further and more intensive studies.

3.2.1.4. Bulkiness versus Acidity towards Formation of Iron (III) Complexes

As mentioned before, different formation of complexes **Fe$_2$Cl$_3$(oCB-L1)$_3$** and **[Fe$_3$Cl$_3$(Ph-L1)$_4$][FeCl$_4$]** is presumably caused by the combined effects of the different acidity and the bulkiness of the corresponding ligands (**Ph-L1**, **oCB-L1** and **mCB-L1**). In this section, the acidities and bulkiness of the ligands employed in the sections above will be discussed and extent the analysis to the other two **oCB** derivatives, a 2-quinolyl (**oCB-L4**) and a **methyl-oCB-L1** derivatives (see nomenclature in Page I), where both are bulkier than the **CB-L1** compounds.

Table 3.2-1 summarized the ^{1}H chemical shifts of the alcohols of all the ligands under the same conditions. According to the NMR spectra, the acidity of the ligands seems to be: **oCB-L4** > **oCB-L1** > **MeoCB-L1** > **Ph-L1** = **I$_2$-mCL1** > **I-mCB-L1** > **mCB-L1**. Note that although the acidity of the alcohol **I$_2$-mCB-L1** is comparable to that of **Ph-L1**, they form different architectures in their reactions with FeCl$_2$ (*vide supra*). This clearly indicates that the dominant factor in this case is the bulkiness of the corresponding ligand. As discussed in the previous section, all **mCB**-based ligands seem to form the same architectures in solution, regardless of their different acidities and bulkiness.

Table 3.2-1: Summary of -OH chemical shiftin ^{1}H NMR

Ligands	-OH δ(ppm)
oCB-L4	6.27
oCB-L1	5.97
MeoCB-L1	5.85
mCB-L1	5.45
I-mCB-L1	5.64
I$_2$-mCB-L1	5.80
Ph-L1	5.80

An interesting example is that for the bulkier ligand **oCB-L4**. The NMR data suggests that the alcohol group in this compound is the most acidic (Table 3.2-1). It was anticipated that the bulky nature of this compound would not form a dinuclear iron complex **FeCl(oCB-L4)$_2$**. This is confirmed by its reaction with FeCl$_3$ and the solid state characterization by single-crystal XRD (Figure 3.2-19) of the final product. Even when a slightly bulkier ligand than **oCB-L1**, such as **MeoCB-L1**, was employed for the reaction with iron, a mono-nuclear iron (III) complex **[FeCl$_3$(MeoCB-L1)][HMeoCB-L1]** was formed (confirmed by

Figure 3.2-19: single-crystal XRD structure of **[FeCl(oCB-L4)$_2$]**

single-crystal XRD[20]). The structures of both **FeCl(oCB-L4)$_2$** and **[FeCl$_3$(MeoCB-L1)][HMeoCB-L1]** are illustrated in Figure 3.2-20.

FeCl(oCB-L4)$_2$ **[FeCl$_3$(MeoCB-L1)][HMeoCB-L1]**
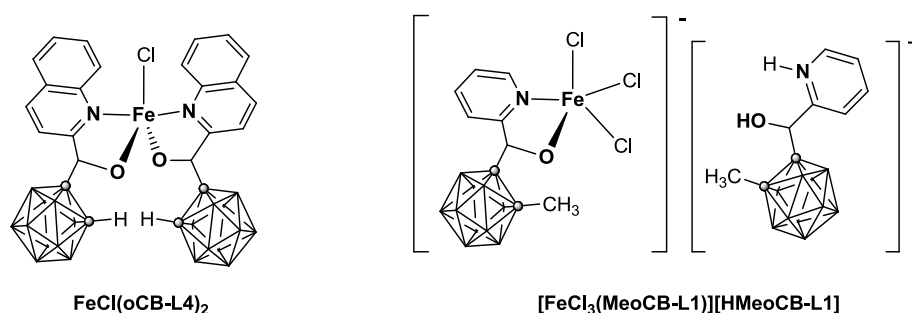
Figure 3.2-20: **FeCl(oCB-L4)$_2$** (left) and **[FeCl$_3$(MeoCB-L1)][HMeoCB-L1]** (right)

These results indicate that the bulkiness of the ligand is the dominant factor for the formation of the iron (III) complex in this system, in which the bulkier the ligand, the lower the polynuclearity. It is in agreement with the literature.[8] However, the influence of the acidity cannot be neglected and could become the dominant factor in the case that the bulky substituent is far away from the reactive coordination site of the ligand, so that the influence of the steric hindrance is minimized. Further studies on the influence of the acidity towards the formation of diiron (III) complexes with carborane moieties might help in understanding this chemistry. For instance, addition of the methyl group(s) at the boron vertex(es) in the corresponding *o*-carborane ligand could in principle reduce the acidity while being far enough of the coordination site (*e.g.* B (9) and/or (12)). This may allow the formation of dinuclear complexes as **oCB-L1** ligand or even as **mCB-L1** derivatives.

3.2.2 Cubane-Liked Copper (I) Iodide Complexes

Luminescent materials received intense studies for sensors or optical devices. Coordination of N-containing monodentate ligands and copper (I) halide can form metal cluster $Cu_nX_nL_m$ which gives intensive luminescent properties. The first copper (I) halide complex $Cu_4I_4(pyridine)_4$ was discovered in 1985 and well-studied thereafter.[21] Even though the topologies are stoichiometric dependence (CuX : L = 1:1 or 1:2) and result in different copper clusters (Scheme 3.2-6),[22] the most studied and common morphology is $Cu_4X_4L_4$ type complexes with cubane-liked cluster.

Scheme 3.2-6: Different morphologies of $Cu_nX_nL_m$ clusters.

| Tetra-nuclear cubane cluster | Tetra-nuclear step cluster | Di-nuclear cluster |

● = Cu (I)
L = donor ligand
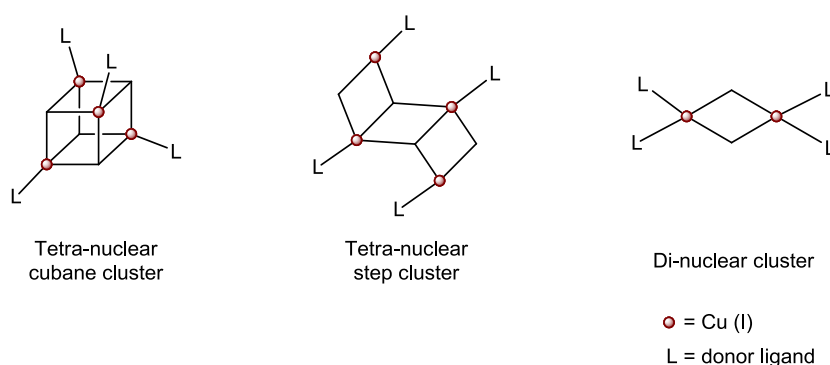
The luminescent properties are depending on the domination of the high energy (HE) halide-to-pyridine charge transfer excited state (XLCT*) or the low energy (LE) cluster-centered excited state (CC*) by changing the temperature, therefore, these Cu(I) complexes are thermochromics. At most of the cases, LE emission is dominant at room temperature while HE emission is dominant at low temperature. For instance, $Cu_4I_4(py)_4$ solid exhibit yellow emission at room temperature, while blue emission appears at 77K. On the other hand, the emission properties are also sensitive to the coordinated ligands. By addition of different substituents to the pyridine ring, various emission colours can be observed, which is due to the flexible Cu_4I_4 core that change the Cu···Cu distance and hence results in different CC* emission.[23,24] Several reports also show potential applications on sensing or light emitting diode (LED) by copper (I) halide materials.[25]

In this section, the preliminary results for the luminescent properties of copper (I) complexes with mono-substituted carborane-based 3-pyridylalcohol (**CB-L2**) and 4-pyridylalcohol (**CB-L3**) will be discussed and compared with the corresponding phenyl derivative (**Ph-L2** and **Ph-L3**).

3.2.2.1   Syntheses with 3- and 4-Pyridylalcohol Ligands

The synthetic procedure was followed with slight modification from the reported literature.[26] Copper (I) iodide (CuI) and the corresponding 4-pyridylalcohols (**R-L3**; where R represents **Ph, *o*CB, *m*CB**) were mixed in 1:1 ratio in acetonitrile at room temperature under ambient condition and stirred until a constant clear yellowish orange solution was obtained (approx. 15 min) (Scheme 3.2-7),

The solvent was then removed and the obtained yellowish powder was re-dissolved in toluene for recrystallization and orange square crystals were formed for **Cu-*o*CB-L3** and **Cu-*m*CB-L3**.

Scheme 3.2-7: Syntheses of **Cu-R-L3**.
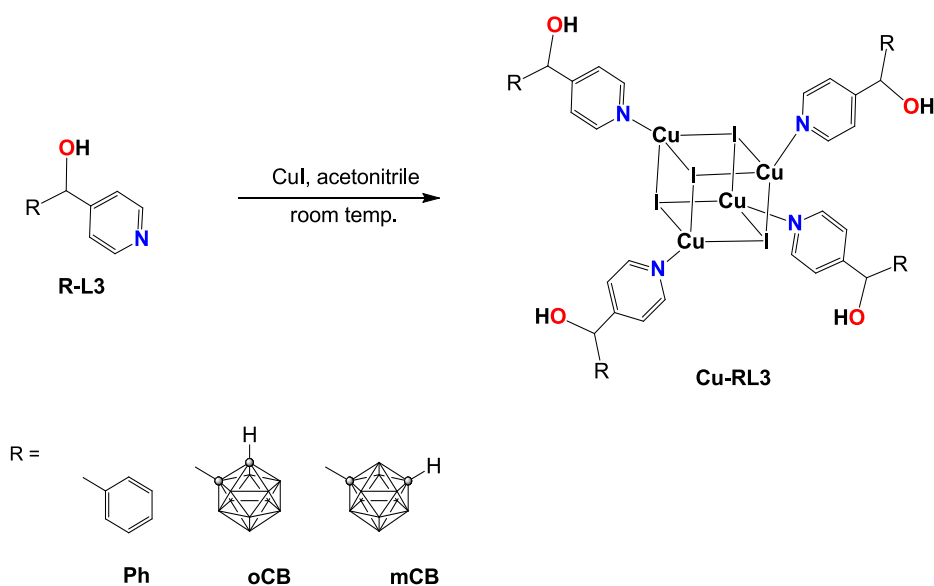
All **Cu-R-L3** compounds are characterized by FTIR-ATR, NMR (^{1}H, ^{11}B, ^{13}C), solid state UV-Vis spectroscopy and fluorescence spectroscopy. The purity of **Cu-R-L3** was proved by elemental analysis and the crystal structure of **Cu-*o*CB-L3** was solved by single-crystal XRD and the preliminary single-crystal XRD data shows that **Cu-*m*CB-L3** is isostructural to **Cu-*o*CB-L3**.

Cu-*o*CB-L3 crystallized in the triclinic and P-1 space group as shown in Figure 3.2-21, the structure for **Cu-*o*CB-L3** consists of a tetranulcear Cu_4I_4 cubane-liked core and each copper ion coordinatedby one *o*CB-L3 ligand, via the nitrogen atoms. The solid structure is dominated by intermolecular O-H···I interactions (Figure 3.2-22).
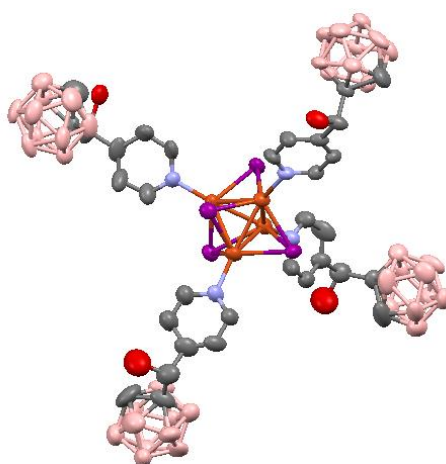
Figure 3.2-21: crystal structure of **Cu-*o*CB-L3**. Thermal ellipsoid set at 50%. Colour code: B pink; C grey; O red; N blue; I violet; Cu orange. Only one enantiomer is represented in those structures with disorder of OH groups.
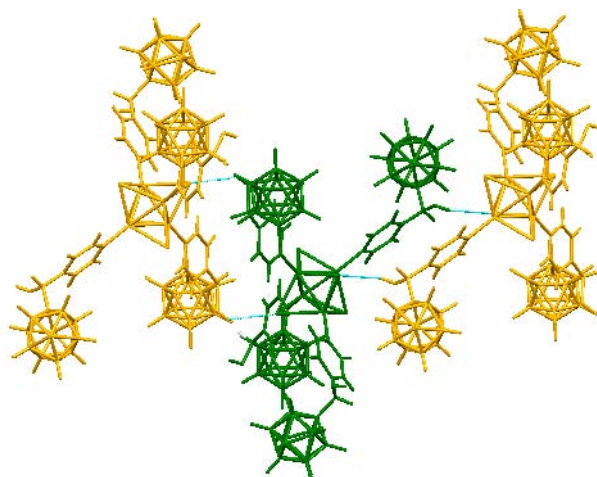
Figure 3.2-22: crystal packing of **Cu-*o*CB-L3** in symmetry operation style. **Cu-*o*CB-L3** molecules are connected through I···H-O hydrogen bonds in the crystal lattice.

Characterization of selected example **Cu-*o*CB-L3** and the corresponding ***o*CB-L3** ligand by ^{1}H and ^{11}B NMR spectra.

NMR (^{1}H and [11]B) spectra of the ***o*CB-L3** and **Cu-*o*CB-L3** are shown in Figure 3.2-23 as a general example for the chemical shift of the **Cu-R-L3** complexes and the corresponding **R-L3** ligand. In the ^{1}H NMR spectra, the proton resonances show characteristic peaks for one cage-carbon C-H vertex of the carborane cluster, pyridine ring and CHOH moiety as discussed in Chapter 3.1.1. The signals of **Cu-*o*CB-L3** are shifted downfield as expected because of the coordination with copper ions. The clear sharp signals also an indication of diamagnetic species, in this case copper (I), therefore, no oxidation occurs to form copper (II) (paramagnetic). In the ^{11}B NMR spectra, both ***o*CB-L3** and **Cu-*o*CB-L3** are in the range of in the range of δ-2.4 to -12.4 for ten boron atoms, which is consistent with the boron cage of the mono-substituted ligand, implying that there is no degradation occurs for the carborane clusters during complexation.
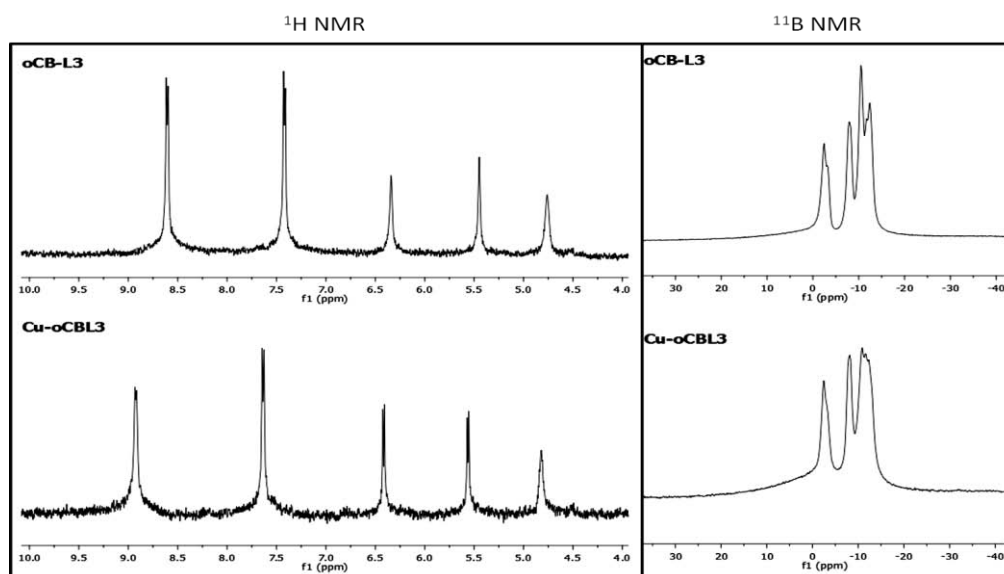
Figure 3.2-23: ^{1}H NMR (left) and ^{11}B NMR (right) of ***o*CB-L3** (top) and **Cu-*o*CB-L3** (bottom).

In addition, since such Cu_4I_4 systems are well studied, the same architecture of Cu (I) complexes can be formed by using 3-pyridylalcohol (**R-L2**) derivatives. In order to study whether the position of the substituents to the pyridine matters for the luminescence behavior, **R-L2** derivatives have been used to synthesize the corresponding Cu_4I_4 complexes followed by the same reaction procedure as for **Cu-R-L3**, where **R** represents **Ph**, ***o*CB** or ***m*CB** and the general characterization of the corresponding complexes **Cu-*o*CB-L2**, **Cu-*m*CB-L2** and **Cu-Ph-L2** have also been performed.

3.2.2.2   Luminescent Properties

Solid-state luminescence results for all complexes **Cu-*o*CB-L3**, **Cu-*m*CB-L3** and **Cu-Ph-L3** in Figure 3.2-24A and **Cu-*o*CB-L2**, **Cu-*m*CB-L2** and **Cu-Ph-L2** in Figure 3.2-24B at room temperature are shown as excitation and emission spectra. The maximum excitation and emission wavelengths are summarized in Table 3.2-2.

A   **B**

Figure 3.2-24: A: Normalized excitation spetra (dotted line, 300 – 450 nm, excitation at maximum emission) and emission spectra (solid line, 450 -750 nm, $\lambda_{exc.}$ = 380 nm). **Cu-*o*CBL3** (blue), **Cu-*m*CBL3** (red) and **Cu-PhL3** (black). All the measurements were done in powder at room temperature. B: Normalized excitation spetra (dotted line, 300 – 450 nm, excitation at maximum emission) and emission spectra (solid line, 450 -750 nm, $\lambda_{exc.}$ = 380 nm). **Cu-*o*CBL2** (blue), **Cu-*m*CBL2** (red) and **Cu-PhL2** (black). All the measurements were done in powder at room temperature.

In general, for the **Cu-R-L3** family, maximum excitation wavelengths for all copper (I) iodide complexes are similar, which is at around 377 nm. The emission wavelengths for **Cu-*o*CB-L3**, **Cu-*m*CB-L3** and **Cu-Ph-L3** are 613 nm, 618 nm and 622 nm, respectively. In the case of **Cu-R-L2** family, maximum excitation wavelengths for all copper (I) iodide complexes are around 380 nm. The emission wavelengths for **Cu-*o*CB-L2**, **Cu-*m*CB-L2** and **Cu-Ph-L2** are 624 nm, 628 nm and 595 nm, respectively.

When comparing to the reported $Cu_4I_4(py)_4$ system, the emission wavelengths for both **Cu-R-L3** and **Cu-R-L2** complexes in general exhibit 20 to 50 nm higher, indicating the addition of the

electron-withdrawing group to the pyridine affect the luminescence and resulting in red shift of the emission wavelength in this system.

Table 3.2-2: Summary of maximum emission and maximum excitation of **Cu-oCB-L3**, **Cu-mCB-L3**, **Cu-Ph-L3**, **Cu-oCB-L2**, **Cu-mCB-L2** and **Cu-Ph-L2** in comparison with the typical $Cu_4I_4(py)_4$ from the literature[24a,27].

		oCB	**mCB**	**Ph**	**Cu₄I₄(py)₄**[24a,27]
L3	Max. emission (nm)	613	618	622	580
	Max. excitation (nm)	377	377	378	380
L2	Max. emission (nm)	624	628	595	
	Max. excitation (nm)	378	382	382	

As explained earlier, there are two distinct emission bands: lower-energy (LE) and higher-energy (HE) bands. Depending on the various factors as mentioned, the inner Cu_4 core size could be changed and given different emissions. At room temperature, the dominant emission is normally by LE. Therefore, the emission bands of complexes **Cu-oCB-L3**, **Cu-mCB-L3**, **Cu-Ph-L3**, **Cu-oCB-L2**, **Cu-mCB-L2** and **Cu-Ph-L2** in Figure 3.2-24 are tentatively assigned to LE emission, which also shown common large stoke shifts that is in agreement with the feature of LE emission.[27] Furthermore, the experimental results show that the addition of electron-withdrawing group in the coordinating ligands seems to increase the emission wavelengths by shortening the Cu⋯Cu distances. It is supported by the comparison of the Cu⋯Cu distances of the core as shown in Table 3.2-3, where the average Cu⋯Cu distance in **Cu-oCB-L3** is shorter than $Cu_4I_4(py)_4$.

Table 3.2-3: Comparison of the selected bond lengths, atom distances and bond angles of **Cu-oCB-L3** from the crystal structure and $Cu_4I_4(py)_4$[28]

	Cu-I Å	Cu-N Å	**Cu⋯Cu Å**	I⋯I Å	Cu-I-Cu deg	N-Cu-I deg	Cu-N-C deg
Cu-oCB-L3	2.632 – 2.734	1.986 – 2.021	**2.585 – 2.701**	4.372 – 4.594	57.07 – 61.10	95.97 – 114.14	115.43 – 127.31
Cu₄I₄(py)₄[28]	2.665 – 2.734	2.02 – 2.06	**2.619 – 2.722**	4.442 – 4.594	57.7 – 61.1	95.2 – 111.4	117.0 – 124.0

As shown earlier (Chapter 3.2), carboranes are more electron-withdrawing than phenyl group, the electron-withdrawing character increases in the order of **Ph** to **mCB** to **oCB**. Thus, addition of these substituents should affect the emission of the Cu_4I_4 complexes in the same trend. However, the maximum emission is observed in the order of **Cu-oCB-L3** < **Cu-mCB-L3** < **Cu-Ph-L3** which is totally opposite to what is expected, even though the difference of the emission wavelengths are very subtle (± 5 nm) which may due to the far away position of the carborane and phenyl moieties from the nitrogen atom. It is worth notice that intermolecular O-H⋯I interactions are presented in the solid state (Figure 3.2-22), in which may affect the Cu_4I_4 core. Therefore, the resulting experimental

emission of **Cu-R-L3** series may due to the combined effects of both electron-withdrawing property and the intermolecular O-H···I interactions. Differently, in the **Cu-R-L2** series, the trend of maximum emissions is in the order of **Cu-Ph-L2** < **Cu-*o*CB-L2** < **Cu-*m*CB-L2**. Since the substituents are relatively closer to the nitrogen atom, the bulkiness of the substituents may also a effect the size of Cu_4I_4 core and result in change of Cu···Cu distance. Besides, when comparing the **L2** and **L3** substituents, the difference of **Cu-Ph-L2** and **Cu-Ph-L3** is 27 nm, **Cu-*o*CB-L2** and **Cu-*o*CB-L3** is 11 nm, **Cu-*m*CB-L2** and **Cu-*m*CB-L3** is 10 nm. This results show the influence of the 3- and 4-pyridine in the carborane moieties seem to be smaller than that of the phenyl moieties for the Cu_4I_4 complexes.

In addition, the preliminary results of the luminescence under UV lamp at both wavelengths 254 nm and 365 nm are shown for the **Cu-R-L3** (Figure 3.2-25A) and the **Cu-R-L2** (Figure 3.2-25B).
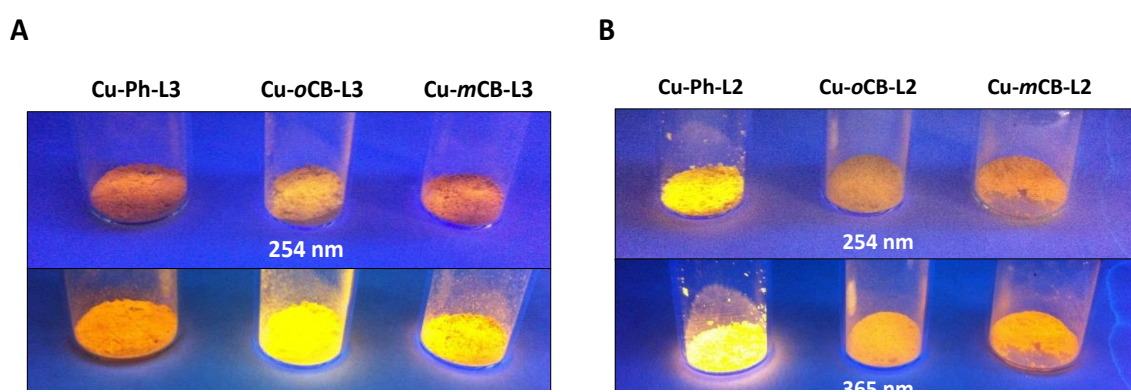
Figure 3.2-25: luminescence images of A: complexes **Cu-*o*CB-L3**, **Cu-*m*CB-L3** and **Cu-Ph-L3** and B: complexes **Cu-*o*CB-L2**, **Cu-*m*CB-L2** and **Cu-Ph-L2** at 254 nm (top) and 365 nm (bottom) under UV lamp.

In the **Cu-R-L3** family, **Cu-*o*CB-L3** appears to have significantly more intense luminescence, followed by **Cu-*m*CB-L3** and **Cu-Ph-L3** has less intense luminescence (Figure 3.2-25A). However, in the case of the **Cu-R-L2** series, **Cu-Ph-L2** appears to have the most intense luminescence. Although further investigation for the solid state emission quantum yields for these complexes is on-going, one of the possible reasons that could influence the emission intensity is the rigidity of the Cu_4I_4 core, in which more rigid of the Cu_4I_4 core can reduce the non-radiative decay, and therefore resulting in higher emission intensity.[29]

The details study of all these series of **Cu-R-L3** and **Cu-R-L2** are still in progress. The influence of the substituents towards the emission of this system is clearly not straightforward, theoretical calculations are definitely required to determine the HOMO and LUMO of the complexes. In addition, the luminescent properties at low temperature and the quantum yields determination are also crucial in order to understand the effect of carboranyl and phenyl moieties towards the Cu_4I_4 complexes system.

References

[1] See for example: T. Taguchi, W. Wernsdorfer, K. A. Abboud and G. Christou,*Inorg. Chem.*, **2010**, *49*, 10579; M. Morimoto, H. Miyasaka, M. Yamashita and M. Irie, *J. Am. Chem. Soc.*, **2009**, *131*, 9823; J. Lawrence, E. C. Yang, D. N. Hendrickson and S. Hill, *Phys. Chem. Chem. Phys.*, **2009**, *11*, 6743; C. G. Efthymiou, C. Papatriantafyllopoulou, N. I. Alexopoulou, C. P. Raptopoulou, R. Boca, J. Mrozinski, E. G. Bakalbassis and S. P. Perlepes,*Polyhedron*, **2009**, *28*, 3373 ; E. Ruiz, T. Cauchy, J. Cano, R. Costa, J. Tercero and S. Alvarez, *J. Am. Chem. Soc.*, **2008**, *130*, 7420; J. Lawrence, E.-C. Yang, R. Edwards, M. M. Olmstead, C. Ramsey, N. S. Dalal, P. K. Gantzel, S. Hill and D. N. Hendrickson, *Inorg. Chem.*, **2008**, *47*, 1965; E.-C. Yang, W. Wernsdorfer, L. N. Zakharov, Y. Karaki, A. Yamaguchi, R. M. Isidro, G.-D. Lu, S. A. Wilson, A. L. Rheingold, H. Ishimoto and D. N. Hendrickson, *Inorg. Chem.*, **2006**, *45*, 529; E.-C. Yang, W. Wernsdorfer, S. Hill, R. S. Edwards, M. Nakano, S. Maccagnano, L. N. Zakharov, A. L. Rheingold, G. Christou and D. N. Hendrickson, *Polyhedron*, **2003**, *22*, 17273

[2] See for example:Jan Moncol, Peter Segla, Dusan Miklos, Milan Mazur, Milan Melnik, Tadeusz Glowiak, Marian Valko, Marian Koman, *Polyhedron*, **2006**, *25*, 1561; J. Moncol, M. Koman, M. Melník, T. Glowiak, *CrystEngComm*, **2001**, 54, 1; Suzanne M. Neville,Gregory J. Halder,Karena W. Chapman,Martin B. Duriska,Peter D. Southon,John D. Cashion,Jean-François Létard,Boujemaa Moubaraki,Keith S. Murray,Cameron J. Kepert, *J. Am. Chem. Soc.,***2008**, *130*, 2869.

[3] F. Di Salvo, F. Teixidor, C. Viñas, J. G. Planas, M. E. Light, M. B. Hursthouse, N. Aliaga-Alcalde, *Cryst. Growth. Des.*, **2012**, *12*, 5720.

[4] a) M. Murugesu, A. Mishra, W. Wernsdorfer, K. A. Abboud, G. Christou., *Polyhedron,***2006**, *25*, 613-625. b) M. C. Munoz, J. A. Real, *Coord. Chem. Rev.*, **2011**, *255*, 2068. c) R. A. Layfield, *Organometallics*, **2014**, *33*, 1084 d) K. Riener, S. Haslinger, A. Raba, M. P. Hogerl, M. Cokoja, W. A. Herrmann, F. E. Kuhn, *Chem. Rev.*, **2014**, *114*, 5215. e) B. Schafer, C. Rajnak, I. Salitros, O. Fuhr, D. Klar, C. Schmitz-Antoniak, E. Weschke, H. Wende, M. Ruben, *Chem. Commun.*, **2013**, *49*, 10986.

[5] a) H. Amouri, M. Gruselle, *Chirality in Transition Metal Chemistry: Molecules, Supramolecular Assemblies and Materials*, Wiley, Chichester, **2008**. b) J. Crassous, Chem. *Soc. Rev.***2009**, *38*, 830, c) C. Train, M. Gruselle, M. Verdaguer, *Chem. Soc. Rev.,***2011**, *40*, 3297. d) J. Crassous, *Chem. Commun*. **2012**, *48*, 9684. e) E. B. Bauer, *Chem. Soc. Rev.*, **2012**, *41*, 3153. f) C. Train, T. Nuida, R. Gheorghe, M. Gruselle, S. Ohkoshi, *JACS*, **2009**, *131*, 16838.

[6] W. Q. Chen, Y. M. Chen, T. Lei, W. Liu, Y. Li, *Inorg. Chem. Commun.*, **2012**, *19*, 4.

[7] K. Butsch, A. Klein, M. Bauer, *Inorg. Chim. Acta.*, **2011**, *374*, *350* and references therein.

[8] T. Taguchi, W. Wernsdofer, K.A. Abboud, G. Christou, *Inorg. Chem.,* **2010**, *49*, 10579

[9] a) J. P. Sun, L. C. Li, X. J. Zheng, *Inorg. Chem. Commun.* **2011**, *14*, 877; b) T. Taguchi, T. C. Stamatatos, K. A. Abboud, C M. Jones, K. M. Poole, T. A. O'Brien, G. Christou, *Inorg. Chem.* **2008**,

47, 4095; c) C. A. Christmas, H. L. Pardi, J. M. Kesselman, P. K. Gantzel, R. K. Chadha, D. Gatteschi, D. F. Harvey, D. N. Hendricson, *JACS*, **1993**, *115*, 12482.

[10] F. Delbecq, P. Sautet, *JACS*, **1992**, *114*, 2446.

[11] O. Kahn, *Molecular Magnetism,* Wiley—VCH, New York, **1993**, 23.

[12] a) R. Singh, A. Banerjee, E. Colacio, K. K. Rajak, *Inorg. Chem.* **2009**, *48*, 4753; b) C. A. Brown, G. J. Rennar, R. L.Musselman, E. I. Solomon, *Inorg. Chem.* **1995**, *34*, 688; c) L. Casella, M. Gullotti, A. Pintar, L.Messori, A.Rockenbauer, M. Gyorl, *Inorg. Chem.* **1987**, *26*, 1031.

[13] H. E. Smith in *Circhlar Dichroism: Principles and Applications, 2nd ed.*, (Eds.: N. Berova, K. Nakanishi, R. W. Woody), Wiley-VCH, Weinheim, **2000**.

[14] H. D. Flack, *Acta Crystallogr. Sect. A* **1983**, *39*, 876.

[15] (a) P. S. Halasyamani, K. R. Poeppelmeier, *Chem. Mater.* **1998**, *10*, 2753; (b) K. M. Ok, E. O. Chi, P. S. Halasyamani, *Chem Soc. Rev.* **2006**, *35*, 710.

[16] a) K. Kinbara, Y. Hashimoto, M. Sukegawa, H. Nohira, K. Saigo, *JACS*, **1996**, *118*, 3441; b) A. Galland, V. Dupray, B. Berton, S. Morin, M. Sanselme, H. Atmani, G. Coquerel, *Cryst. Growth Des.* **2009**, *9*, 2713.

[17] M. Scholz, E. Hey-Hawkins, *Chem. Rev.*, **2011**, *111*, 7035.

[18] A. V. Puga, F. Teixidor, R. Sillanpaa, R. Kivekas, M. Arca, G. Barbera, C. Vinas, *Chem Eur. J.,* **2009**, *15*, 9755.

[19] A. Pepiol, F. Teixidor, R. Sillanpaa, M. Lupu, C. Vinas, *Angew. Chem. Int. Ed.*, **2011**, *50*, 12491.

[20] F. Di Salvo, unpublished result.

[21] J. C. Dyason, P. C. Healy, *J. Chem. Soc. Dalton Trans.*, **1985**, 831.

[22] M. Vitale, P. C. Ford, *Coord. Chem. Rev.*, **2001**, *3*, 219.

[23] F. Parmeggiani, A. Sacchetti, *J. Chem. Educ.*, **2012**, *89*, 946.

[24] (a) P. C. Ford, E. Cariati, J. Bourassa, *Chem. Rev.*, **1999**, *99*, 3625. (b) R. Peng, D. Li, *Coord. Chem. Rev.* **2010**, *254*, 1.

[25] (a) F. D. Angelis, S. Fantacci, A. Sgamellotti, E. Cariati, R. Ugo, P. C. Ford. *Inorg. Chem.*, **2006**, *45*, 10576. (b) S-L. Li, X-M. Zhang, *Inorg. Chem.*, **2014**, *53*, 8376.

[26] R. Peng, M. Li, D. Li, *Coord. Chem. Rev.*, **2010**, *254*, 1.

[27] M. Vitale, W.E. Palke, P. C. Ford, *J. Phys. Chem*., **1992**, *96*, 8329.

[28] F. De Angelis, S. Fantacci, A. Sgamellotti, E. Cariati, R. Ugo, P. C. Ford, *Inorg. Chem.*, **2006**, *45*, 10576.

[29] P. P. mazzeo, L. Maini, A. Petrolati, V. Fattori, K. Shankland, D. Braga, *Dalton Traons.*, **2014**, *43*, 9448.

3.3 Disubstituted N,O-Type *ortho-* and *meta-* Carborane-Based 2-Pyridylalcohol Complexes

Similar to the monosubstituted 2-pyridylalcohol ligands, both disubstituted *ortho-* and *meta-* carborane based 2-pyridylalcohol ligands (**oCB-(L1)₂** and **mCB-(L1)₂**, respectively) contain two side arms which can act as bidentate or monodentate moieties (Figure 3.3-1).
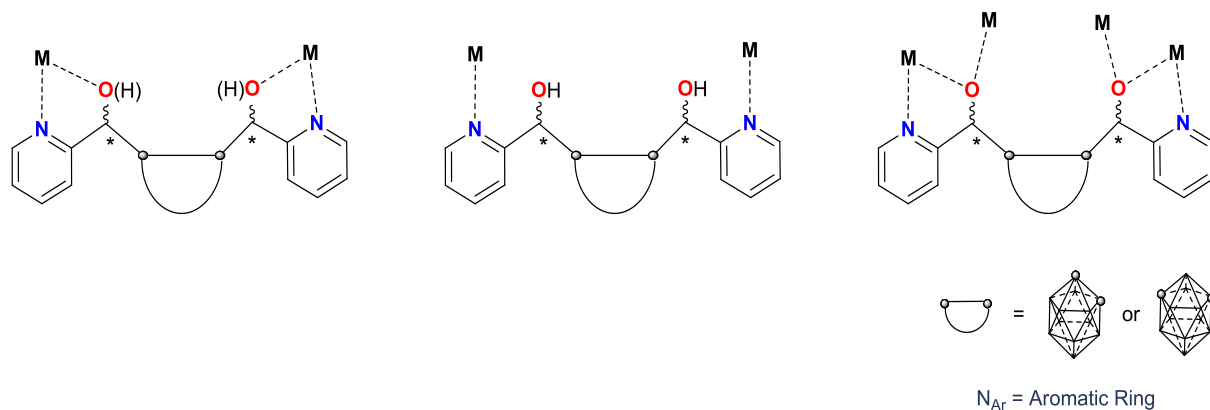
Figure 3.3-1: Some of the possible coordination of **oCB-(L1)₂** and **mCB-(L1)₂**.

The flexibility (bending and rotation) of the side arms, in addition to the hetero-donor coordination sites of the ligands bring numerous possibilities to form different functional compounds. Nevertheless, as mentioned in section 3.1.1.2, the diastereoisomers (*syn-* and *anti-*) are differentiable due to the steric hindrance of **oCB-(L1)₂**. Therefore, the coordination with metal ions can be affected at certain circumstances. As shown in Scheme 3.3-1, in principle, the rotation of the *anti-***oCB-(L1)₂** is less restricted compared to the *syn-***oCB-(L1)₂** due to the position of the alcohol moieties. Thus, a tetradentate coordination of *anti-***oCB-(L1)₂** is feasible. This is demonstrated by the first complexation example from the disubstituted ligand, a tetradentate cobalt (II) complex.[1] However, because of the far distance between two carbons of the carborane cluster, the tetradentate coordination is probably not feasible for the case of **mCB-(L1)₂** ligands.

Scheme 3.3-1: Illustration of the rotation flexibility for anti-isomer of 2-pyridylalchol ligand **oCB-(L1)₂** and the possible tetradentate coordination with metal ions
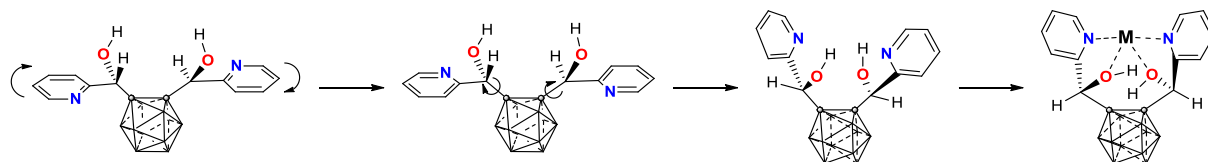
In this chapter, complexation of **oCB-(L1)₂** and **mCB-(L1)₂** with palladium and iron will be shown. A series of palladium (II) pincer type complexes have been synthesized and the potential catalytic application will be demonstrated. Additionally, the formation of the iron (III) complexes and its magnetic properties will be discussed thereafter.

3.3.1 Pincer-Type Palladium (II) Complexes

Pincer complexes have received considerate attention since the first discovery in 1976.[2] The corresponding ligands feature with tridentate binding sites constructed by aσ-bond coordinating bridgehead and two donor side-arms (Scheme 3.3-2). This type of ligands allows functionalization of the side-arms and the bridgehead position, providing a way to fine tune the steric and electronic properties of the ligands to obtain new complex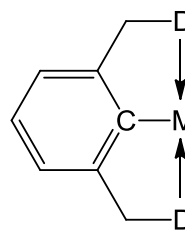es with desired properties. Besides, the direct σ-bonding gives additional stability to the complexes. These unique systems have gained interest in catalyses[3] also some on sensors[4] or switches.[5]

Scheme 3.3-2: General structure of Pincer complex

D = donor atom: O, S, N, P
M = metallic centre

Most of the coordinating bridgehead positions are carbon-based, although some contain amido,[6] silyl[7] or phophido[8] units. The first boron-based coordinating bridgehead position system was reported by Teixidor *et al.*[9] Later, two different groups reported the first YBY (Y = S or Se; B = boron) (Figure 3.3-2) and NBN *closo-meta*-carboranyl pincer complexes and studies on its catalytic activity.[10,11]

VUGWOK   **VUGWIE**
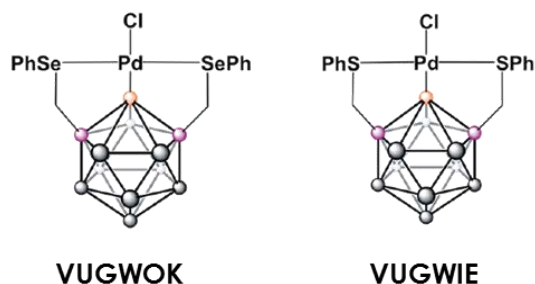
Figure 3.3-2: The first reported closo-*meta*-carboranyl pincer complexes.[9]

Herein, by introducing the disubstituted carboranyl 2-pyridylalcohol ligands **CB-(L1)$_2$** and **CB-(L5)$_2$** described in Chapter 3.1, the first family of *ortho*-carboranyl NBN palladium pincer complexes were obtained and compared with the corresponding *meta*-carboranyl NBN pincer complexes. The synthesis, structural and electronic characterization, and study on their catalytic properties will be reported in the present section.

3.3.1.1 Syntheses of the NBN Pincer Complexes

The disubstituted 2-pyridylalcohol ligands *o***CB-(L1)$_2$**, *o***CB-(L5)$_2$** and *m***CB-(L1)$_2$** were used to react with palladium. Due to the higher tendency of palladium ion to coordinate to nitrogen from the pyridine rings over oxygen from the alcohol groups and the flexibility of the methylalcohol arms of the ligand, polynuclear complexes were expected to be formed. Surprisingly, mononuclear pincer complexes were formed as shown in Scheme 3.3-3. The mononuclear pincer complexes were obtained by reaction of corresponding 2-pyridylalcohol **CB-(L)$_2$** ligand and [PdCl$_2$(MeCN)$_2$] in acetone under air. The pincer complexes were obtained as pale yellow precipitates in high yield (71 – 76 %).

Scheme 3.3-3: Synthetic route of NBN pincer complexes **Pd-*o*CB(L1)₂**, **Pd-*o*CB(L5)₂** (top) and **Pd-*m*CB(L1)₂** (bottom).

The formation of the pincer complexes was confirmed by single-crystal XRD (Figure 3.3-3). The Pd-B σ-bond formation is driven by the B-H activation occurred at the relatively more positive charge B(3) or B(6) in *o*-carborane and B(2) or B(3) in *m*-carborane (those close to the carborane carbon atoms).[12,13]

Pd-*o*CB(L1)₂
Triclinic
Space group: P-1

Pd-*o*CB(L5)₂
Triclinic
Space group: P-1

Pd-*m*CB(L1)₂
Triclinic
Space group: P2₁/c

Figure 3.3-3: Structures of **Pd-*o*CB(L1)₂**, **Pd-*o*CB(L5)₂** and **Pd-*m*CB(L1)₂**; thermal ellipsoids set at 90%, 70% and 80% probability, respectively, and H atoms are represented as fixed-size spheres of 0.18Å (B-H and pyridine hydrogen atoms are omitted for clarity). Color code: B pink; C grey; H white; O red; N blue; Cl green; Pd prussian blue. Only one steroisomer is reporesented in those structures with disorder of OH groups.

Complete characterization has been done by conventional spectroscopic methods and elemental analysis and all the data is consistent with the proposed structures. Selected NMR spectra for **Pd-*o*CB(L1)₂** and **Pd-*m*CB(L1)₂** are shown in Figure 3.3-4 and 3.3-5, respectively.

In the ¹H NMR spectra, the proton resonances show characteristic peaks for the pyridine ring and CHOH moiety as discussed in Chapter 3.1.2. The proton signals of the pyridylalcohols ligand in the

pincer complexes are shifted downfield as expected due to the coordination to the palladium ions. In both cases, diastereoisomers are expected to form but only those for the *meta*-carborane pincer complex **Pd-*m*CB(L1)$_2$** are observed by NMR (Figure 3.3-4 and 3.3-5, left).
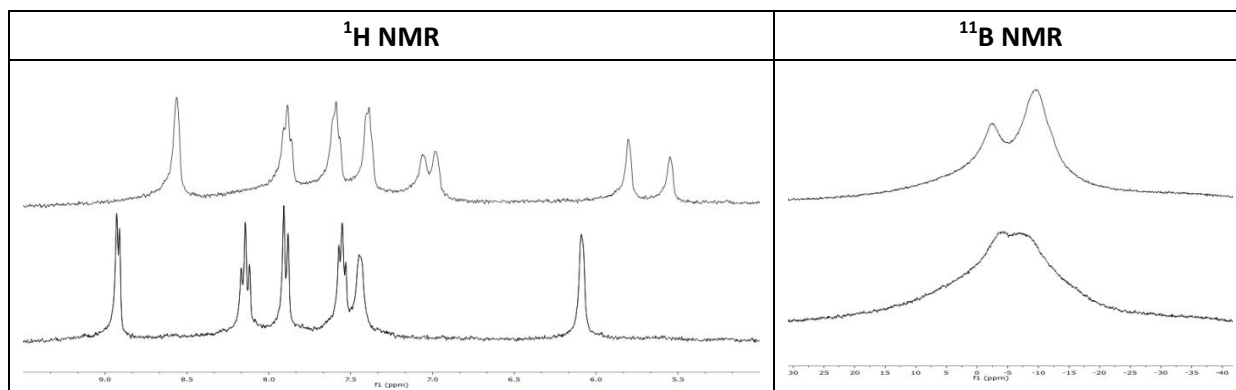

Figure 3.3-4: Comparison of a selected ^{1}H and 11B NMR spectra for ***o*CB-(L1)$_2$** (top) and **Pd-*o*CB(L1)$_2$** (bottom) in DMSO-D$_6$.
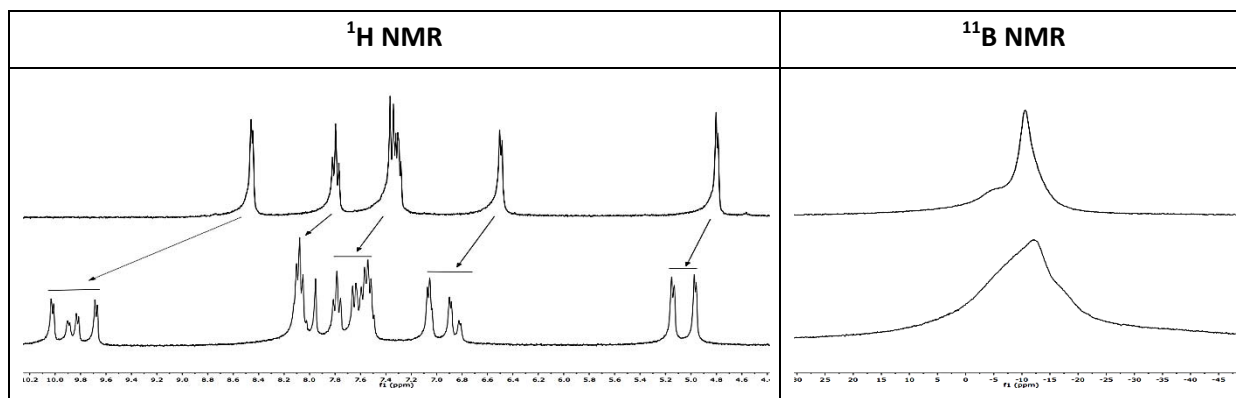

Figure 3.3-5: Comparison of a selected ^{1}H and 11B NMR spectra for ***m*CB-(L1)$_2$** (top) and **Pd-*m*CB(L1)$_2$** (bottom) in DMSO-D$_6$.

It is worth notice that the symmetry of the carborane clusters are different between the free ligands (10 B-Hs) and the pincer complexes (9 B-Hs) giving differentiable patterns for the hydride signals in the ^{11}B-decoupled ^{1}H NMR (^{1}H{^{11}B} NMR) spectra (Figure 3.3-6). A significant upfield BH hydrogen signal at δ 0.37 is observed in ^{1}H{^{11}B} NMR spectrum of **Pd-*o*CB(L1)$_2$**. This signal is likely due to the effect of the shielding cone of the pyridine rings to the hydrides of B (4) and B (7). Although the assignment of the upfielded signals are not so obvious in the ^{1}H{^{11}B} NMR spectrum of **Pd-*m*CB(L1)$_2$** due to the mixture of the diastereoisomers and the overlapped signals of the solvents (DMSO-D$_6$, DMF and H$_2$O), a clear difference of the hydrides patterns from the ***m*CB-(L1)$_2$** are seen.

Very broad resonances are observed in the ^{11}B NMR spectra (Figure 3.3-4 and 3.3-5, right) for both **Pd-*o*CB(L1)$_2$** and **Pd-*m*CB(L1)$_2$**, compared to the free ligands, the broad resonances in the range of δ +10 to -20. This broadness, probably due to the overlapped signals of the diastereomeric mixtures, does not allow the observation of the typical singlet signal for the boron atom bonded to Pd at $\delta \approx 0$.[10]
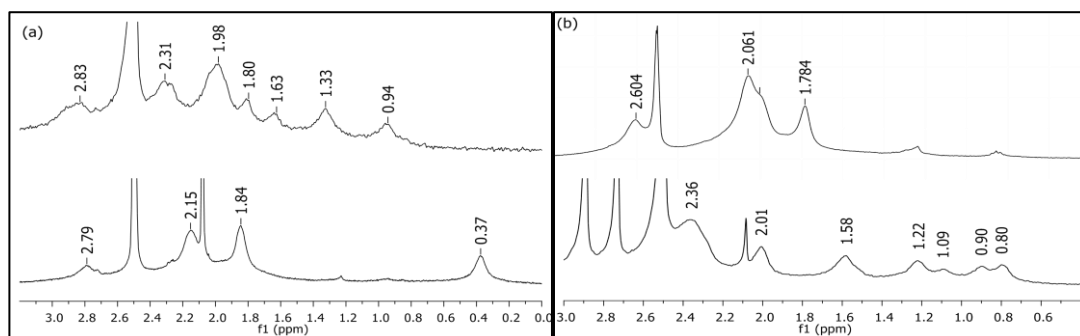
Figure 3.3-6: Comparison of a selected range of ^{1}H $\{^{11}$B$\}$ NMR spectra (a) *o*CB-(L1)$_2$ (top) and **Pd-*o*CB(L1)$_2$** (bottom); (b) ***m*CB-(L1)$_2$** (top) and **Pd-*m*CB(L1)$_2$** (bottom) in DMSO-D$_6$, the labelled signals correspond to the H$^-$ of BHs.

3.3.1.2 *Trans* Influence: X-ray Structures versus DFT Calculations

The structures of those complexes that have been measured by single-crystal XRD are shown in Figure 3.3-3, in which the pyridine rings are in a *trans* fashion, as well as the chloride atom which is opposite to the boron atom that is coordinated to Pd ion. The observed long Pd-Cl distance in the crystal structures suggests a strong *trans* influence induced by the carborane moieties. The short Pd-B distances are also consistent with the previously reported *m*-carboranyl-based pincers.[10] Comparing the Pd-Cl distance to the similar motifs in aryl-based pincers (2.39 – 2.45 Å),[14] the complexes *syn*-**Pd-*o*CB(L1)$_2$**, **Pd-*o*CB(L5)$_2$** and **Pd-*m*CB(L1)$_2$** display exceptionally longer Pd-Cl distances, however, comparable with the related alkyl-based pincers (2.49 – 2.52 Å).[15] In order to understand more the architecture of such pincers, density functional theory (DFT) calculations were performed for complexes *syn*-**Pd-*o*CB(L1)$_2$**, **Pd-*o*CB(L5)$_2$** and **Pd-*m*CB(L1)$_2$** as well as the reported pincers **VUGWIE** and **VUGWOK** (Figure 3.3-2).[10] Unlike the measured distances from the X-ray structures, the optimized monomers of compounds *syn*-**Pd-*o*CB(L1)$_2$**, **Pd-*o*CB(L5)$_2$** and **Pd-*m*CB(L1)$_2$** show significantly shorter Pd-Cl distances (and longer Pd-B distances). Control calculations with different theoretical methods were performed and gave the similar outcome (Table 3.3-1), indicating that the discrepancy is not due to the accuracy of the calculation methods.
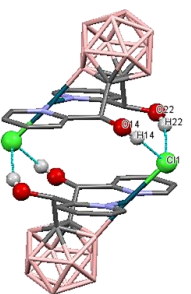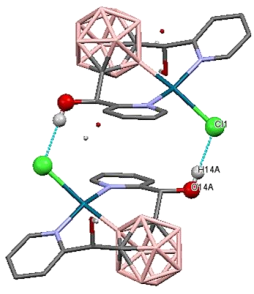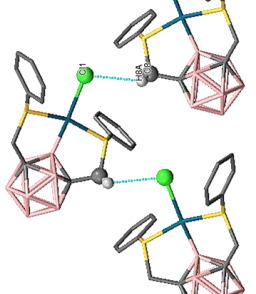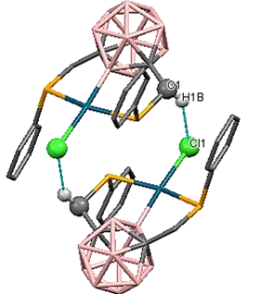
Table 3.3-1: Comparison of the selected Pd-Cl distances (Å) for **Pd-*o*CB(L1)$_2$**, **Pd-*o*CB(L5)$_2$** and **Pd-*m*CB(L1)$_2$**, **VUGWIE** and **VUGWOK** from x-ray structures and different DFT calculation methods.

	syn-**Pd-*o*CB(L1)$_2$**	**Pd-*o*CB(L5)$_2$**	**Pd-*m*CB(L1)$_2$**	**VUGWIE**	**VUGWOK**
Measured (X-ray structure)	2.4915	2.4879	2.5063	2.4170	2.4371
PBE-D3	2.406	2.430	2.437	2.402	2.422
PBE	2.410	--	--	--	--
M06*	2.429	2.456	2.466	2.424	2.432
*perfomed with Gaussian09 with basis set 6-311g(d) on B, C, N, 6-311+g(d) on O and Cl, and SDD core potential and associated basis set augmented with an f polarization function on Pd					

Further study of the crystal structures reveal that the elongation of the Pd-Cl distances are caused by the formation of the moderate H-bonds between the hydroxyl groups and the chloride ligand of the neighbouring complexes and a relatively weaker C–H···Cl H-bond interactions in **VUGWIE** and **VUGWOK** (Table 3.3-2). Thus, the DFT calculations of the dimeric structures of *syn*-**Pd-*o*CB(L1)₂** and **Pd-*m*CB(L1)₂** were performed, as well as the **VUGWIE** and **VUGWOK** for comparison purpose. The results show good agreement with the measured data from the crystal structures (Table 3.3-2). Therefore, the operative factors that modulate the Pd-Cl distances in the solid state can be concluded by the two effects: the *trans* influence of the carborane moieties and the intermolecular moderate H-bond interactions among the neighbouring complexes. Thus, more appropriate indication to conclude the *trans* influence should be determined by the gas phase calculations rather than the measured distances in the X-ray crystal structures.

Table 3.3-2: Comparison of the selected Pd-B and Pd-Cl distances (Å) for *syn*-**Pd-*o*CB(L1)₂**, **Pd-*m*CB(L1)₂** and **VUGWOK** dimers and **VUGWIE** trimer from x-ray structures and the calculated values.

	syn-Pd-oCB(L1)₂ (dimer)	Pd-mCB(L1)₂ (dimer)	VUGWIE (trimer)	VUGWOK (dimer)
Measured Pd-Cl (X-ray structure)	2.4915	2.5063	2.4170	2.4371
Measured Pd-B (X-ray structure)	2.021	1.974	1.983	1.982
Pd-Cl	2.502	2.497 (anti) 2.505 (syn)	2.402	2.422
Pd-B	2.043	1.992 (anti) 1.987 (syn)	1.998	2.011

*perfomed with Gaussian09 with basis set 6-311g(d) on B, C, N, 6-311+g(d) on O and Cl, and SDD core potential and associated basis set augmented with an f polarization function on Pd

3.3.1.3   Determination of the Palladium Oxidation State

It is important to examine the nature of the palladium metal centre since in these carboranyl pincer compounds, the oxidation state of the palladium was proposed to be palladium (0) based on the calculation with Mulliken and Löwdin methods.[10] In order to investigate these compounds, the atomic charges with various methods (Mulliken, Löwdin, Bader and NPA) were performed in compounds *syn*-**Pd-*o*CB(L1)₂**, **Pd-*m*CB(L1)₂**, and also **VUGWIE**, **VUGWOK** for comparison. The

resulting calculated atomic charge of the **Pd** and **B** atoms show no consistency (Table 3.3-3). In another words, the charge of the **Pd** and **B** atoms could be positive or negative depending on the selected calculation method. This suggests that the interpretation of the oxidation state of the metal centre based on the charge calculation is delicate.

Table 3.3-3: Selected atomic charges (Bader / Mulliken / Lowdin / NPA).

complex	*syn*- **Pd-oCB(L1)$_2$**	**Pd-oCB(L5)$_2$**	**Pd-mCB(L1)$_2$**	**VUGWIE**	**VUGWOK**
Pd	+0.280	+0.241	+0.247	+0.060	+0.007
	-0.097	-0.114	-0.061	-0.382	-0.230
	-0.491	-0.545	-0.423	-1.065	-0.959
	+0.512	+0.493	+0.540	+0.300	+0.265
Cl	-0.616	-0.615	-0.638	-0.607	-0.608
	-0.444	-0.444	-0.453	-0.429	-0.439
	+0.039	+0.060	+0.067	+0.018	+0.060
	-0.674	-0.680	-0.691	-0.667	-0.672
B (coord.)	+0.856	+0.746	+1.254	+1.205	+1.238
	+0.151	+0.144	+0.139	+0.087	+0.128
	+0.109	+0.116	+0.062	-0.038	+0.011
	+0.260	+0.257	+0.280	+0.251	+0.245
ligand	*syn*-**oCB-(L1)$_2$**	**oCB-(L2)$_2$**	*m***CB-(L1)$_2$**	**VUGWIE**	**VUGWOK**
B	+1.837	+1.746	+2.192	+2.247	+2.193
	+0.061	+0.056	+0.063	+0.015	+0.034
	+0.091	+0.092	+0.095	+0.068	+0.066

The orbital localization procedure provides the electron density distribution of each orbital and the localized centroid (Wannier centers) of the orbital, which allows visualization of *where* the electrons are and *who* they belong to. In this method, only valence electrons are involved in the calculation. For example, in Figure 3.3-7, one localized orbital of the Pd-Cl bond is shown from the PdCl$_4^{2-}$ complex. The red dots represent the centroid of the localized orbitals, in which, each red dot accounts for two electrons. Basically, as illustrated, the centroid of the Pd-Cl orbital (as pointed with red arrow) is closer to the Cl, so the bonding electrons *belong* to Cl. Besides, the 8 centroids around the Pd atom indicate the corresponding valence electrons $4s^2 4p^6 4d^8$, as expected for palladium (II).[16]

This approach has been successfully applied to characterize the surrounding effects[17] on bonding interactions and developing iconicity scales,[18] and also proposed by Sit *et al.* to determine the oxidation state of the transition metal centres by electron counting procedure that is based on the assignment of the localized orbital centroids to the individual atoms.[19] In addition, the electronic structure of organometallic compounds are also analysed by this method recently.[16]
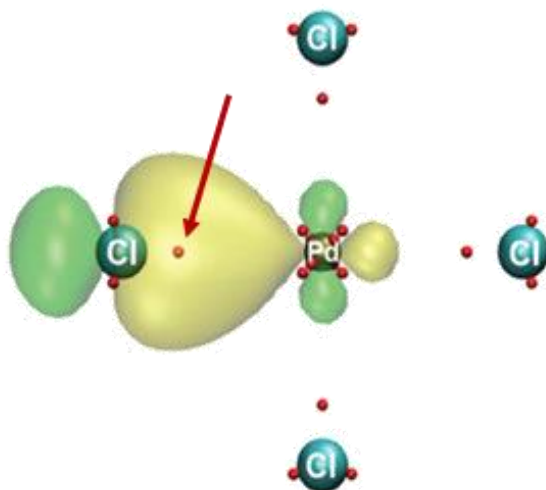
Figure 3.3-7: Square planar PdCl$_4^{2-}$ complex as an example. Centroids of the localized orbitals are shown as red dots (each centroid is hidden below the atom's spheres). An isosurface of a localized orbital corresponding to one Pd-Cl bond is also shown.[16]

Thus, this method has been applied to investigate all the pincer complexes and the same methodology that proposed by Sit *et al*. has been employed to analyse the oxidation state of the palladium metal centre. The selected localized centroid of *syn*-**Pd-*o*CB(L1)$_2$** and the corresponding free ligand *syn*-***o*CB-(L1)$_2$** are shown as a representation (Figure 3.3-8). The results show the localized orbitals corresponding to the Pd-Cl bond and the Pd-B bond in *syn*-**Pd-*o*CB(L1)$_2$** (Figure 3.3-8a and b) and H-B bond in the free ligand *syn*-***o*CB-(L1)$_2$** (Figure 3.3-8c). Combining the resulting change of the polarity of the bond, from the H-B (centroid closer to H) to the Pd-B (centroid locates in the middle), and the pear shape of the Pd-B localized orbital, the electrons in the Pd-B bond seem to *belong* to the boron which is in agreement with a palladium (II). Therefore, the oxidation state of the palladium is assigned as palladium (II) and not as palladium (0) as previously suggested for this type of pincer complexes.[10]

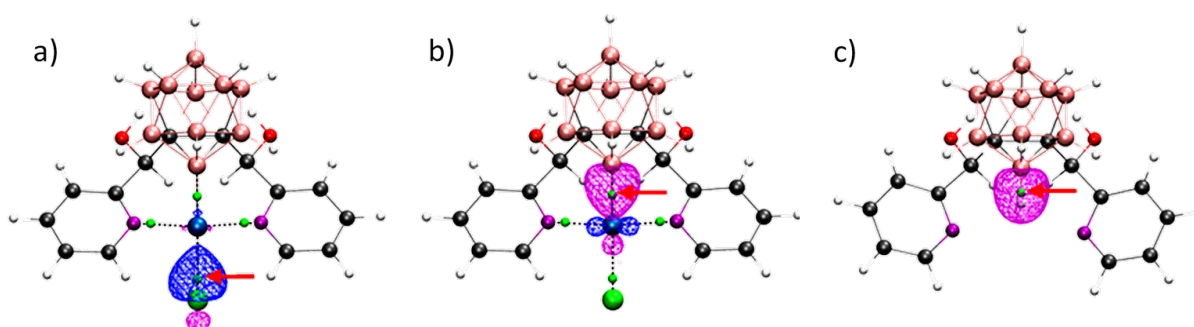**Figure 3.3-8**: Localized orbitals corresponding to the Pd-Cl, Pd-B and H-B bonds of *syn*-**Pd-*o*CB(L1)$_2$** (a and b) and *syn*-***o*CB-(L1)$_2$** (c), respectively. The orbital centroids of the localized orbitals at the Pd center are shown as small green dots

3.3.1.4 Catalytic Activities

As mentioned previously, pincer complexes are potential catalysts. Thus, a systematic study on the homogeneous catalytic activity of the pincer complexes **Pd-*o*CB(L1)₂**, **Pd-*m*CB(L1)₂** were evaluated in the Suzuki-Miyaura cross-coupling reaction which is a Pd-catalyzed C-C bond-forming processes.[20] Two common substrates, 4-methyoxylphenylboronic acid and 4-bromoacetophenone, were chosen. Initial study by using **Pd-*o*CB(L1)₂** as the catalyst in a constant loading (0.1 mol %) with various conditions were performed (Table 3.3-4) and the conversion rates were determined by GC-MS. The preliminary data showed that the use of water as reaction media gave far better results (entry 10 vs 1-8) than the organic solvents or aqueous/organic solvent mixtures (THF, DMF, MeOH, THF/H$_2$O, MeOH/H$_2$O), or even with the addition of tetra-n-butylammonium bromide (TBAB) as a stabilizing agent (entry 5 vs 6) for the palladium nanoparticles.[21] Further decrease of the amount of catalyst to 10^{-4} mol % also results in a high conversion (entry 16). A blank reaction was performed in the absence of the pincer complex, and no coupling reaction was observed. ICP-MS analysis of all the reagents employed for the test (aryl halide, boronic acid, potassium carbonate (K$_2$CO$_3$)) shows that the content of the palladium residual is only around 10^{-5} mol %. Therefore, the possibility of the coupling reaction that induces by this palladium trace from the substrates can be ruled out.

Table 3.3-4: Summary of reactions conditions for the coupling between 4-bromoacetophenone and 4-methoxyphenylboronic acid.

Entry	Reaction conditions (i)[a]	Conv. (%)[b]
1	KOH (2.5 eq.), THF, 40ºC, 10h	-
2	K$_2$CO$_3$ (2.0 eq.), TBAB (1 eq.), THF, 40ºC, 12h	10
3	K$_3$PO$_4$ (2 eq.), DMF, 80ºC, 10h	5
4	K$_2$CO$_3$ (2.0 eq.), CH$_3$OH:H$_2$O (3:1), 70ºC, 12h	-
5	K$_2$CO$_3$ (2.5 eq.), TBAB (1 eq.), CH$_3$OH, 70ºC, 10h	68
6	K$_2$CO$_3$ (2.0 eq.), CH$_3$OH, 70ºC, 10h	66
7	Cs$_2$CO$_3$ (2.5 eq.), H$_2$O, 100ºC, 12h	7
8	K$_2$CO$_3$ (2.0 eq.), THF:H$_2$O (9:1), 80ºC, 10h	88
9	Et$_3$N (2.0 eq.), H$_2$O, 80ºC, 12h	99
10	K$_2$CO$_3$ (2.0 eq.), H$_2$O, 110ºC, 10h	99
11[c]	K$_2$CO$_3$ (2.5 eq.), TBAB (1 eq.), CH$_3$OH, 70ºC, 10h	62

12[c]	K$_2$CO$_3$ (2.5 eq.), TBAB (1 eq.), CH$_3$OH, 100ºC, 10h	63
13[c]	K$_2$CO$_3$ (2.0 eq.), CH$_3$OH, 70ºC, 10h	60
14[c]	K$_2$CO$_3$ (2.0 eq.), THF:H$_2$O (9:1), 80ºC, 10h	84
15[c]	Et$_3$N (2.0 eq.), H$_2$O, 80ºC, 12h	95
16[c]	K$_2$CO$_3$ (2.0 eq.), H$_2$O, 110ºC, 10h	99
17[d]	K$_2$CO$_3$ (2.0 eq.), H$_2$O, 110ºC, 10h	-

[a]4-bromoacetophenone, 4-methoxyphenylboronic acid (1.5 equiv), **Pd-oCB(L1)$_2$** (10^{-1} mol %), base (2-3 equiv), solvent (1 mL per mmol of substrate), additive (when indicated). [b]Conversion rate measured by GC-MS. [c]**Pd-oCB(L1)$_2$** (10^{-4} mol %). [d]Reaction performed in the absence of **Pd-oCB(L1)$_2$**.

Furthermore, a range of different substrates were submitted to the full catalytic activity study by using both **Pd-oCB(L1)$_2$** and **Pd-mCB(L1)$_2$** pincer complexes as catalysts under the optimized condition (10^{-4} mol % catalyst loading, K$_2$CO$_3$, H$_2$O, 110 ^{o}C, 10h), and the final products were isolated by column chromatography and confirmed by NMR spectroscopy. The results show that not only arylboronic acids can be coupled effectively with aryl bromides, but also the potassium phenyltrifluoroborate (Table 3.3-5, entries 3, 5, 7 and 10). Nonetheless, benzyl bromide can also be used as a coupling partner (Table 3.3-5, entries 11-14), in which either electron withdrawing or electron donating groups can be incorporated in the substrates. Additionally, no by-product can be observed but only the unreacted halides were found in the crude reaction mixtures. Overall, **Pd-oCB(L1)$_2$** gives a better catalytic profile than **Pd-mCB(L1)$_2$**. Also, the turn-over-number (TON) values for **Pd-oCB(L1)$_2$** is ranging from 770000 to 990000. Hence, a very high catalytic activity is revealed from **Pd-oCB(L1)$_2$** which rivals the reported palladium catalysts performance in very low catalyst loading on Suzuki coupling reaction, even with the other pincer type complexes.[22]

Table 3.3-5: Suzuki Coupling in the presence of carborane-based NBN Pincer complexes.

Entry	R^1	R^2	n	Y	**Pd-oCB(L1)$_2$**(%)[a]	**Pd-mCB(L1)$_2$**(%)[a]
1	(acetophenyl)	(4-OMe-phenyl)	0	B(OH)$_2$	99	60
2	(acetophenyl)	(phenyl)	0	B(OH)$_2$	99	85

3[b]	4-acetylphenyl	phenyl	0	BF$_3$K	99	93
4	4-MeO-phenyl	phenyl	0	B(OH)$_2$	84	90
5[b]	4-MeO-phenyl	phenyl	0	BF$_3$K	92	60
6	2-Cl-phenyl	phenyl	0	B(OH)$_2$	91	5
7[b]	2-Cl-phenyl	phenyl	0	BF$_3$K	97	69
8	2-Cl-phenyl	3,4-(OMe)$_2$-phenyl	0	B(OH)$_2$	77	20
9	5-Cl-2-OMe-phenyl	phenyl	0	B(OH)$_2$	66	56
10[b]	5-Cl-2-OMe-phenyl	phenyl	0	BF$_3$K	61	54
11	benzyl	4-OMe-phenyl	1	B(OH)$_2$	82	99
12	benzyl	naphthyl	1	B(OH)$_2$	99	99
13	benzyl	3,5-F$_2$-phenyl	1	B(OH)$_2$	87	95
14	benzyl	3,4-(OMe)$_2$-phenyl	1	B(OH)$_2$	99	99

[a] Aryl or arylmethyl bromide, arylboronic acid or aryl trifluoroborate (1.5 eq.), **Pd-*o*CB(L1)$_2$** or **Pd-*m*CB(L1)$_2$** (10^{-4} mol%), K$_2$CO$_3$ (2.0 eq.), H$_2$O (1 ml per mmol of ArBr or ArCH$_2$Br), 110ºC, 10h. Isolated yields. [b] 2.5 eq. of K$_2$CO$_3$ were used.

These remarkable results open a new window for development of a new type of carborane-based pincer catalysts. The chirality of these carborane-based ligands also provides a possible synthetic path to obtain the corresponding chiral pincer complexes as a potential candidate for enantioselective catalytic studies.

3.3.2 Symmetric Iron (III) Complexes

As shown previously in Chapter 3.1.1.2, disubstituted ligands are obtained as a mixture of two diastereoisomers: meso compound (*RS*; OH groups in a *syn*-orientation; non chiral) and racemic compound (mixture of *SS* and *RR*; OH groups in an *anti*-orientation, chiral). Influence towards complex formation is possible by incorporating with different diastereoisomer as mentioned at the beginning of this chapter.Therefore, in this section, the coordination chemistry of both diastereoisomers of the 2-pyridylalcohol ligand **oCB-(L1)₂** is explored individually for iron. The study on the complexes formation and the magnetic properties will be discussed, followed by the coordination study with diastereoisomers of **oCB-(L1)₂**.

3.3.2.1 Synthesis of *ortho*-Carborane-Based Complex with *anti-o*CB-(L1)₂

The *syn*- and *anti-o*CB-(L1)₂ were separated by preparative TLC (eluent: hexane/ethanol = 9:1) andwere studied individually. The separated *anti-o*CB-(L1)₂ ligand was then reacted with FeCl₂ (1:1 ratio) in acetone at room temperature under air. Slow evaporation of solvent from the reaction mixture afforded yellow needle-like crystals that corresponded to the tetradentate dinuclear iron (III) complex **Fe₂Cl₂(*anti-o*CB-(L1)₂)₂** (Scheme 3.3-4). The purity was proved by elemental analysis and the structure confirmed by single-crystal XRD.

Scheme 3.3-4: synthetic procedure of **Fe₂Cl₂(*o*CB-(L1)₂)₂**

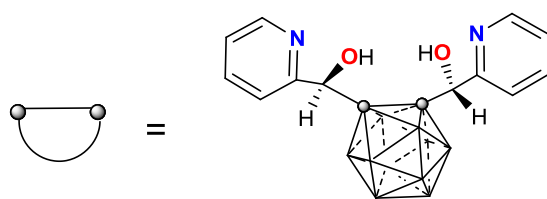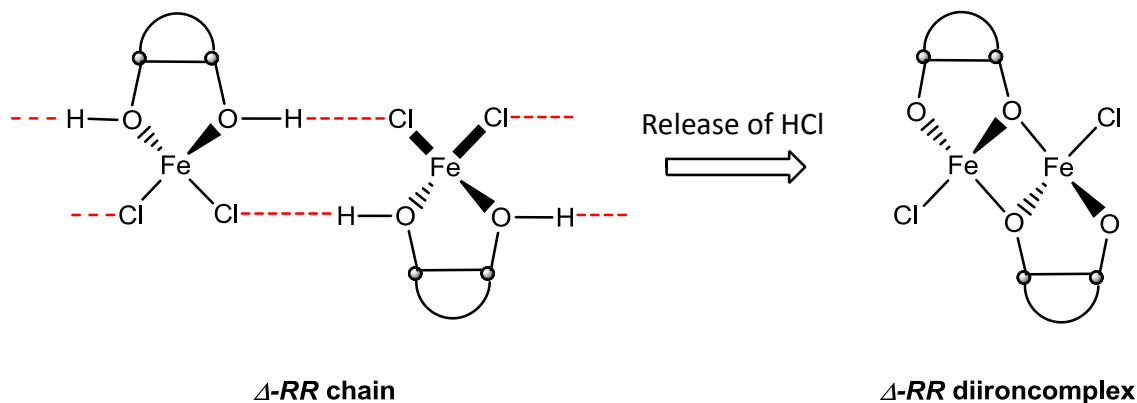*anti-o*CB-(L1)₂   **Fe₂Cl₂(*anti-o*CB-(L1)₂)₂**
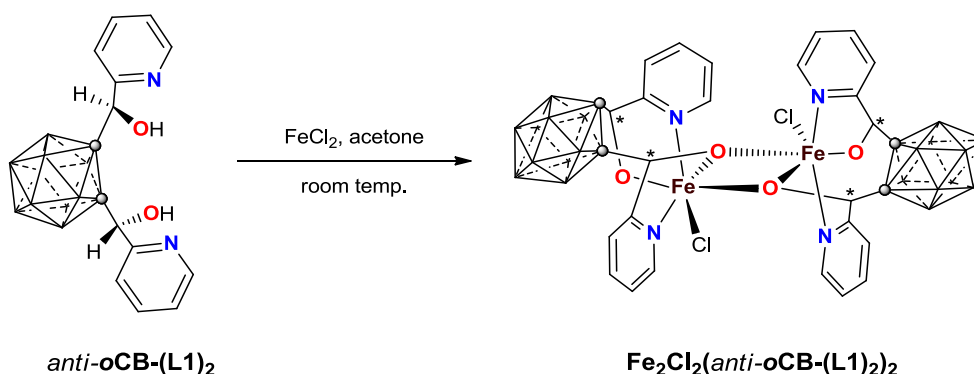
Different than palladium, iron has high affinity to coordinate with oxygen as explained earlier (see Chapter 3.2.1.). Similar to the previously reported cobalt (II) complex,[1] distorted octahedral geometry is observed in **Fe₂Cl₂(*anti-o*CB-(L1)₂)₂** (Figure 3.3-9A). The six coordinated iron (III) atoms are linked by two μ-alkoxo bridges from one of the oxygen atoms of each *anti-o*CB-(L1)₂ ligand. The octahedral coordination of each iron (III) ion is completed by one oxygen, two nitrogen atoms from the *anti-o*CB-(L1)₂ ligand and a terminal Cl⁻ ion.

As mentioned earlier (Chapter 3.1.1), only the *anti*-isomer of disubstituted ligand such as *anti-o*CB-(L1)₂ is chiral. Interestingly, homochirality is observed in complex **Fe₂Cl₂(*anti-o*CB-(L1)₂)₂**. That is, both ligands in each dinuclear complex in the solid structure show the same configuration (*RR* or *SS*), affording **Fe₂Cl₂(*RR*anti-o*CB-(L1)₂)₂** or **Fe₂Cl₂(*SS*anti-o*CB-(L1)₂)₂**. Homochirla recognition was

previously observed in cobalt (II) complexes with *anti-o*CB-(L1)$_2$, where mononuclear compleces formed supramolecular homochiral ribbons in the solid state.[1] Provided that a similar homochiral recognition takes place for the iron derivative in solution (Scheme 3.3-5), HCl release and oxidation to iron (III) would explain the observed homochirality of **Fe$_2$Cl$_2$(*anti-o*CB-(L1)$_2$)$_2$** (Scheme 3.3-5).

Scheme 3.3-5: Hypothetic scheme for the formation of homochiral **Fe$_2$Cl$_2$(*anti-o*CB-(L1)$_2$)$_2$**

Δ-RR **chain**   *Δ-RR* **diironcomplex**

Cl⁻exchange is possible and gives rise to an opportunity to modify and functionalize the corresponding complexes. Since the chloride ions are exposed from the complex skeleton, **Fe$_2$Cl$_2$(*anti-o*CB-(L1)$_2$)$_2$** could be used as a building unit. Thus, thiocyanide ion was selected for the initial study as it can be a bridging unit for further extension.
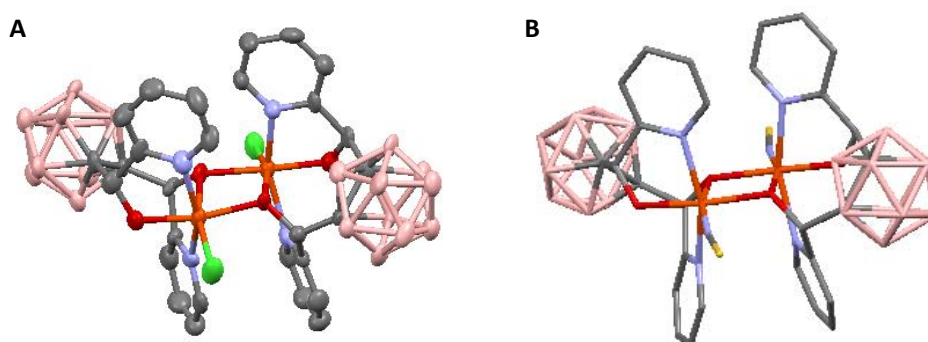
A   B

Figure 3.3-9: A:Molecular structure of**Fe$_2$Cl$_2$(*o*CB-(L1)$_2$)$_2$**. Thermal ellipsoids set at 80% probability (hydrogen atoms are omitted for clarity). B: provisional molecular structure of **Fe$_2$(SCN)$_2$(*o*CB-(L1)$_2$)$_2$**. Color code: B pink; C grey; H white; O red; N blue;Cl green; Feorange, S: yellow.

Two equivalents of thiocyanide (SCN⁻) were added to the *anti-o*CB-(L1)$_2$ and FeCl$_2$ reaction mixture in acetone, a reddish solution was obtained. Evaporation of the solvent afforded reddish needle-like

crystals and the preliminary crystallographic data shows that the same architecture of iron (III) complex as **Fe$_2$Cl$_2$(*anti*-*o*CB-(L1)$_2$)$_2$** is formed and the Cl$^-$ ions are replaced by SCN$^-$ (Figure 3.3-10B).

3.3.2.2 Characterization and Properties

The symmetric **Fe$_2$Cl$_2$(*anti*-*o*CB-(L1)$_2$)$_2$** has been fully characterized by FTIR-ATR, cyclic voltammetry and the purity of the complex is proved by elemental analysis. The magnetic properties have also been measured in solid state.

Cyclic Voltammetry

The cyclic voltammogram (CV) of this symmetric complex **Fe$_2$Cl$_2$(*anti*-*o*CB-(L1)$_2$)$_2$** was measured in acetonitrile (Figure 3.3-10). One quasi-reversible redox process (I) was obseved at E$_{1/2}$ = -0.08 V which is attributed to the successive one-electron redox couples Fe^{III} + 1e$^-$ $\rightarrow$ Fe^{II}. This correlates well with the formation of a symmetric **Fe$_2$Cl$_2$(*anti*-*o*CB-(L1)$_2$)$_2$** complex. In addition, an irreversible wave (II) was observed at +0.56 V which is similar to the complex **Fe$_2$Cl$_3$(*o*CB-L1)$_3$** as discussed earlier (Chapter 3.2.1).
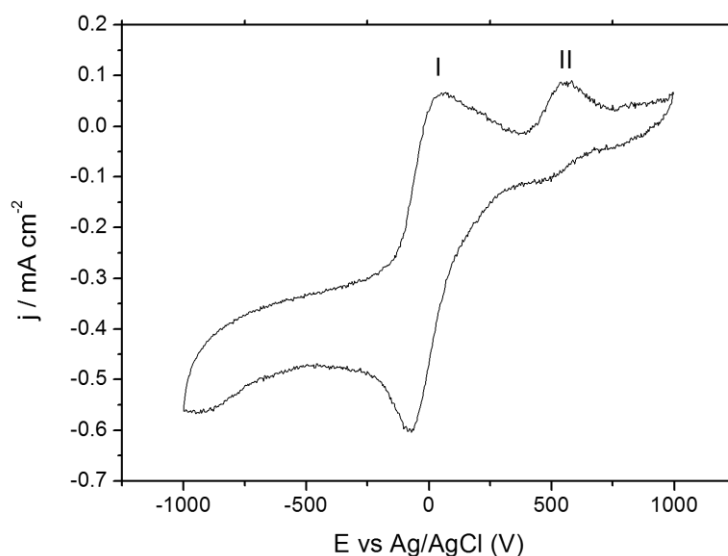

Figure 3.3-10: Cyclic votammetry (CV) of complex **Fe$_2$Cl$_2$(*anti*-*o*CB-(L1)$_2$)$_2$** at 100 mV^{-1} in dry acetonitrile. Plots versus Ag wire; the ferrocene couple was measured at +0.220 V versus this reference under the same conditions.

Magnetic Properties

The variable-temperature (2 - 300 K) magnetic susceptibility data of the bulk solid complex **Fe$_2$Cl$_2$(*anti*-*o*CB-(L1)$_2$)$_2$** was collected under 0.03 and 0.5 T external magnetic fields (Figure 3.3-11). The result shows the antiferromagnetic behavior where the susceptibility χ_MT is 6.56 cm^{3}mol^{-1}K at

300 K and decreases to 0.19 $cm^3mol^{-1}K$ while lowering the temperatureto1.8 K. The lower $\chi_M T$ value of complex **Fe₂Cl₃(*o*CB-L1)₃** compared to the two independent high-spin iron (III) centers ($\chi_M T$ = 8.75 $cm^3mol^{-1}K$; *g* = 2.00) is a clear evidence of the antiferromagnetic interaction.

Figure 3.3-11: Fitting of the $\chi_M T$versus T of **Fe₂Cl₂(*anti-o*CB-(L1)₂)₂** between 2 and 300K. The experimental data are shown as ■ and − corresponds to the fitting values

The data was analyzed by using the highest field and program PHI,[23] that incorporates the spin exchange Hamiltonian H = -2JS_1S_2, where here S_1 = S_2 = 5/2.The best fit matches well with experimental data and provided the following values: D = +47.7 cm^{-1}, E = -3.6 cm^{-1}, where $D$and E correspond to the values of the axial and values of rhombic field splitting,respectively, for each individual Fe[III] carrier, *g* = 1.96, 2J = -7.62 (J = -15.2 cm^{-1}) cm^{-1} and ρ = 0.04 %. Overall, the analysis of the data agreeswith the shapeand values observed in the experimental measurement,in which the exchange coupling for both iron (III) atomsis significantly antiferromagnetic.Tests using exclusively the exchange coupling parameter J and *g*also allow similar results (2J = -7.24 cm^{-1} and *g* = 1.93). Similarly, a common antiferromagnetic behavior is observed in **Fe₂Cl₂(*anti-o*CB-(L1)₂)₂** and in other reported symmetric [Fe[III]₂-(OX)₂] complexes.[24] Although the exceptionally long Fe-O distance (2.052 – 2.083 Å) is observed in **Fe₂Cl₂(*anti-o*CB-(L1)₂)₂**, the Fe···Fe distance (3.259 Å) and the average Fe-O-Fe angle (103.6°) are in line with the reported alkoxo-bridged diiron (III) complexes.[24]

3.3.2.3 Complexation with *syn-o*CB-(L1)₂: Conformational Influence

The high flexibility allows the *anti-o*CB-(L1)₂ ligand to coordinate in a tetradentate style. In order to investigate whether the less flexible meso diastereoisomer affects the complex formation, *syn-o*CB-(L1)₂ ligand was used. As in all iron chemistry in this thesis, the paramagnetic nature of the iron (III) complexes prevented the analysis with NMR spectroscopy. Therefore, reaction with different solvents for crystallization was performed to get measurable single crystals for characterization. Only polar solvents can be used as reaction media, in this case, acetone, acetonitrile,

DMF, MeOH and EtOH were used respectively. After 3-5 days, yellowish single crystals were obtained only when using DMF, MeOH and EtOH (Figure 3.3-12). Unexpectedly, no iron complexes were formed from DMF or MeOH reaction media (Figure 3.3-12A and B), instead, carborane cage degradation occurred and formed *nido*-species. This can be explained by the long crystallization process in relatively basic and/or nucleophilic solvents and that the **oCB-(L1)₂** ligand is activated toward the deboronation (see Chapter 1.1).
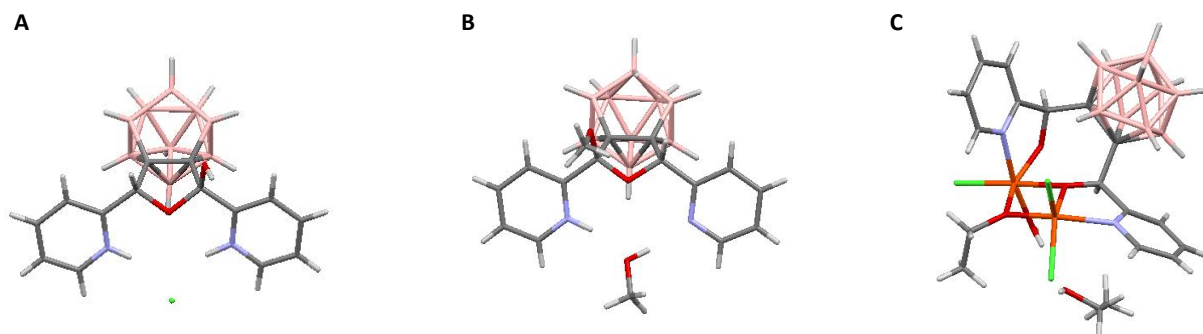
Figure 3.3-12: Molecular structure of reaction product in different solvent media. A: DMF, B: MeOH and C: EtOH. Color code: B pink; C grey; H white; O red; N blue;Cl green; Feorange

Besides, protonation of the pyridine rings are observed and the diols in *syn-oCB-(L1)₂* was converted to a cyclic ether compound in both cases (Figure 3.3-12A and B). It is known that diols can be converted to cyclic ether under acidic condition in organic synthesis.[25] As mentioned earlier in Chapter 3.2.1, HCl is released while forming the iron complexes. Therefore, creating an acidic environment during complexation is possibly the driving factor to convert the diol to cyclic ether. On the contrary, when EtOH was used as the reaction media, a dinuclear iron (III) complex **Fe₂Cl₃(*syn-oCB-(L1)(DMF)(H₂O)*)** was formed without deboronation of the carborane cage (Figure 3.3-12C). Similar to **Fe₂Cl₂(*anti-oCB-(L1)₂)₂*)**, the six coordinated Fe (III) atoms are linked by two μ-alkoxo bridges, but from only one *syn-oCB-(L1)₂* ligand instead and one ethanol molecule. The octahedral coordination of each iron (III) ion is completed by a Cl⁻ ion and a H₂O molecule on one iron ion and two Cl⁻ ions on the other iron ion.

The structure of **Fe₂Cl₃(*syn-oCB-(L1)(DMF)(H₂O)*)** clearly indicates that coordination of *syn-oCB-(L1)₂* is different to that of its *anti-oCB-(L1)₂* isomer and it is probably due to the steric hindrance from the *syn*-configuration of the OH groups. Thus, unlike *anti-oCB-(L1)₂*, *syn-oCB-(L1)₂* could only act as bidentate ligand and resulting in coordination of the pyridylalcohol units with two different iron ions (Figure 3.3-13).
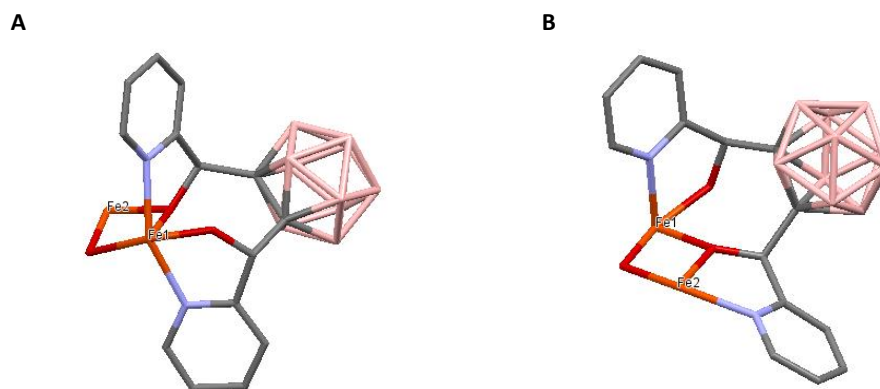
A   B

Figure 3.3-13: Selected coordination architecture of ligand **o**CB-(L1)$_2$ and diiron core from the crystal structures of A: **Fe$_2$Cl$_2$(**anti-**o**CB-(L1)$_2$)$_2$** and B: **Fe$_2$Cl$_3$(**syn-**o**CB-(L1)(DMF)(H$_2$O)**. The two iron (III) atoms are labelled.

References

[1] F. Di Salvo, F. Teixidor, C. Viñas, J. G. Planas, *Z. Anorg. Allg. Chem.*, **2013**, *639*, 1194.

[2] C. J. Moulton, B. L. Shaw,*J. Chem. Soc. Dalton Trans*. **1976**, 1020-1024.

[3] (a) M. Albrecht, G. van Koten, *Angew. Chem. Int. Ed.*, **2001**, *40*, 3750. (b) D. Morales-Morales, *Rev. Soc. Quim. Mex.*, **2004**, *48*, 338-346. (c) G. van Koten, *J.Organomet. Chem.*, **2013**, *730*, 156-164. (d) D. Benito-Garagorri, K. Kirchner, *Acc. Chem. Res.*, **2008**, *41*, 201-213. (e) N, Selander, K. Szabo, *J. Chem. Rev.*, **2011**, *111*, 2048-2076. (f) I. Moreno, R. SanMartin, B. Ines, F. Churruca. E. Dominguez., *Inorg. Chim. Acta.*, **2010**, *363*, 1903-1911.

[4] (a) M. Albrecht, M. Schlupp, J. Bargon,G.van Koten, *Chem. Commun.***2001**, 1874-1875. (b) M. Albrecht, G. van Koten, *Adv. Mater.*, **1999**, *11*, 171-174. (c) D. Benito-Garagorri, M. Puchberger, K. Mereiter. K. Kirchner., *Angew. Chem. Int. Ed.*, **2008**, *47*, 9142-9145.

[5] M. Albrecht, M. Lutz, A. M. M. Schreurs, E. T. H. Lutz, A. L. Spek,G. van Koten, *J. Chem. Soc. Dalton Trans.***2000**, 3797-3804.

[6] (a) L. C.Liang, *Coord. Chem. Rev.***2006**, *250*, 1152-1177. (b) L. Fan,B. M.Foxman, O. V. Ozerov, *Organometallics*,**2004**, *23*, 326-328.(c) M. D. Fryzuk, Can. *J. Chem.***1992**, *70*, 2839-2845.

[7] (a) L. S. H.Dixon, A. F.Hill, A.Sinha, J. S.Ward,*Organometallics*,**2014**, *33*, 653-658. (b) E. E.Korshin, G.Leitus, L. J. W.Shimon, L.Konstantinovski, D. Milstein, *Inorg. Chem.***2008**, *47*, 7177-7189.(c) M. C.MacInnis, D. F.MacLean,R. J.Lundgren, R.MacDonald,L.Turculet, *Organometallics*,**2007**, *26*, 6522-6525. (d) P.Sangtrirutnugul,T. D.Tilley, *Organometallics*,**2007**, *26*, 5557-5568.

[8] N. P.Mankad, E.Rivard, S. B.Harkins, J. C.Peters,*J. Am.Chem. Soc,.* **2005**, *127*, 16032-16033.

[9] F.Teixidor, A.Romerosa, C.Viñas, J.Rius, C.Miravittles,J.Casabó, *J. Chem. Soc. Chem. Commun.* **1991**, 192-193.

[10] A. M.Spokoyny, M. G.Reuter, C. L. Sterm, M. A.Ratner,T.Seideman, C. A.Mirkin,*J. Am. Chem. Soc.***2009**, *131*, 9482-9483.

[11] M. E.El-Zaria, H.Arii, H.Nakamura, *Inorg. Chem.***2011**, *50*,4149-4161.

[12] (a) R. N.Grimes, *Carboranes, 2nd ed*; Elsevier: Amsterdam,**2011**. (b) M.Scholz, E.Hey-Hawkins, *Chem. Rev.*,**2011**, *111*, 7035-7062.(c) I. T.Chizhevsky, *Coord. Chem. Rev.*,**2007**, *251*, 1590-1619. (d) F.Teixidor, C.Viñas, In Science of Synthesis; Thieme: Stuttgart, **2005**; Vol. 6, p1235. (e) Z. Xie, *Acc. Chem. Res.*,**2003**, *36*, 1-9.

[13] (a) J. F. Valliant,K. J.Guenther, A. S.King, P.Morel, P. Schaffer, O. O.Sogbein,K.Stephensen, *Coord. Chem. Rev.*,**2002**, *232*, 173-230. (b) M.F.Hawthorne, Z.P.Zheng, *Acc. Chem. Res.*,**1997**, *30*, 267-276. (c) J. Plešek, *Chem. Rev.*,**1992**, *92*, 269-278. (d) V. I.Bregadze, *Chem. Rev.*,**1992**, *92*, 209-223.

[14] Selected examples of NCarylN-pincer palladium:
(a)(pyrido[2',3':5,6]naphtho[2,3-h]quinolin-14-yl)PdCl, Pd–Cl2.4304(17) Å, K. J. H.Young, X.Bu, W. C. J.Kaska, *Organomet.Chem.* **2011**, *696*, 3992–3997.
(b) (2-(pyridin-2-yl)-6-((pyridin-2-yl)sulfanyl)phenyl)PdCl, Pd–Cl 2.4191(6) Å, M.Hirotsu,Y.Tsukahara, I.Kinoshita, *Bull. Chem. Soc. Jpn.***2010**, *83*, 1058-1066.

(c) ((5S,7S)-2,6-bis(6,6-dimethyl-5,6,7,8-tetrahydro-5,7-methanoquinolin-2-yl)phenyl)PdCl, Pd−Cl 2.451(1) Å, B. Soro,; S. Stoccoro,G. Minghetti, A. Zucca, M. A. Cinellu, M. Manassero, S. Gladiali,*Inorg. Chim. Acta.*. **2006**, *359*, 1879−1888.

(d) (2,6-bis(2-pyridyl)phenyl)PdCl, Pd−Cl 2.427(1) Å, B. Soro, S. Stoccoro, G. Minghetti, A. Zucca, M. A. Cinellu, S. Gladiali, M. Manassero, M. Sansoni, *Organometallics*, **2005**, *24*, 53−61.

(e) (4-bromo-2,6-bis(7-azaindolyl)-phenyl)PdCl, Pd−Cl 2.3867(16) Å, D. Song, Q. Wu, A. Hook,I. Kozin, S. Wang, *Organometallics*, **2001**, *20*, 4683−4689.

[15] Selected examples of NCa lkylN-pincer palladium:

(a) (3,5-tBu2pz)2PdCl(Me), Pd−Cl 2.5165(9) Å, K. Li, J. Darkwa, I. A. Guzei, S. F. Mapolie, *J. Organomet. Chem.***2002**, *660*, 108−115. (b)(N-N')(h2-olefin)PdCl(Me), Pd−Cl 2.492(1) Å, V. G. Albano, C. Casterllari, *Organometallics*, **1990**, *9*, 1269−1276.

[16] P. Vidossich, A. Lledos, *Dalton Trans*,.**2014**, *43*, 11145-11151.

[17] F. Alber, G. Folkers, P. J. Carloni, *Phys. Chem. B*, **1999**, *103*, 6121-6126.

[18] H. Abu-Farsakh, A. Qteish, *Phys. Rev. B*, **2007**, *75*, 085201.

[19] P. H. L. Sit, F. Zipoli, J. Chen, R. Car, M. H. Cohen, A. Selloni, *Chem.Eur.J,.***2011**, *17*, 12136-12143.

[20] R. martin, S. L. Buchwald, *Acc. Chem. Res.*, **2008**, *41*, 1461-1473

[21] A. Molnar, *Palladium-Catalyzed Coupling Reactions: Practical Aspects and Future Developments*, Ed.; Wiley: Weinheim, **2013**.

[22] (a) I. P.Beletskaya, A. V.Cheprakov, *J. Organomet. Chem*,.**2004**,*689*, 4055-4082. (b) J. L.Bolliger, O.Blacque, C. M.Frech, *Angew. Chem. Int. Ed.,***2007**,*46*, 6514-6517. (c) B.Inés, R.SanMartin, M. J.Moure, E.Dominguez, *Adv. Synth. Catal.,***2009**, *351*, 2124–2132. (d) G. K.Rao, A.Kumar, J.Ahmedz, A. K. Singh, *Chem.Commun.,***2010**, *46*, 5954−5956.

[23] N. F. Chilton, R. P. Anderson, L. D. Turner, A. Soncini and K. S. Murray *J. Comput. Chem.* **2013**,*34*, 1164.

[24] R. Biswas, C. Diaz, A. Bauza, A. Frontera, A. Ghosh, *Dalton Trans.*, **2013**, *42*, 12274

[25] (a) F. Arico, P. Tundo, A. Maranzana, G. Tonachini, *ChemSusChem.*, **2012**, *5*, 1578. (b) Y. Kasashima, H. Fujimoto, T. Mino, M. Sakamoto, T. Fujita, *J. Oleo Sci.*, **2008**, *57*, 437

3.4 Disubstituted N,O-Type *ortho*- and *meta*- Carborane-Based 3-Pyridylalcohol Complexes

Disubstituted 3- and 4-pyridylalcohol ligands (*o*CB-(L2)$_2$, *o*CB-(L3)$_2$, *m*CB-(L2)$_2$ and *m*CB-(L3)$_2$) contain two monodentate side arms as previously discussed in Chapter 3.1.1.1 The ditopic nature of the N donors from the pyridine rings and the flexibility of the side arms provide a wide bite angle range ($0^o - 180^o$), which allow these ligands to act as bridging linkers. Thus, n-nuclear (n = 2 to ∞) complexes with various architectures are in principle possible (Scheme 3.4-1). This big directional variation of the ligands gives opportunities to target different functional materials by proper selection of transition metals.

Scheme 3.4-1: The illustration for the coordination mode of the disubstituted 3- pyridylalcohol ligands *o*CB-(L2)$_2$, and *m*CB-(L2)$_2$ and 4- pyridylalcohol ligands *o*CB-(L3)$_2$ and *m*CB-(L3)$_2$.
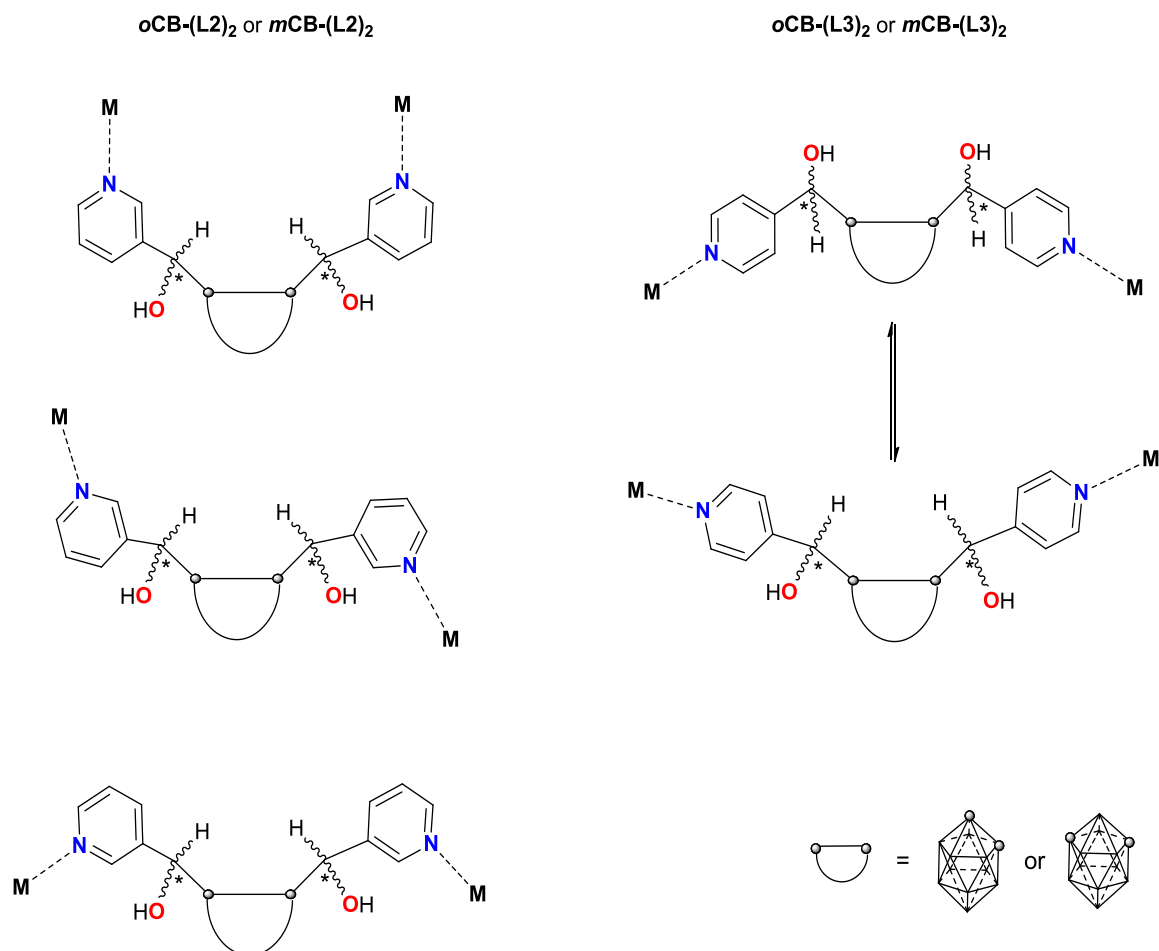
In this chapter, it is summarized some preliminary results on the coordination chemistry of 3-pyridylalcohol ligands **CB-(L2)$_2$** toward Pd, Zn and Co, which include a palladium (II) macrocyclic dimer and zinc (II) and cobalt (II) coordination polymers. The flexibility of such ligands makes it possible to create materials from molecular levels to three dimensional frameworks with different strategies.

3.4.1 Palladium (II) Macrocyclic Dimer

The complexation studies of the **CB-(L2)$_2$** ligands was started by using palladium due to its simple coordination behaviour (4 coordination sites with square planar geometry) and because of the diamagnetic nature of this metal allows NMR characterization and analysis. Initial study has been carried out with the 3-pyridylalcohol ligands *syn*-isomer (*syn*-**oCB-(L2)$_2$**) ligand because of its relatively rigid conformation of *o*-carborane derivatives as mentioned earlier in Chapter 3.1.1.2.

Many studies on Pd$_2$L$_2$ macrocyclic system demonstrate interesting behaviours, such as polymeric transformation and selective solvent container.[1] Beside that, the addition of tuneable functional group in the internal structure of the macrocyclic ring can improves the selectivity of the materials on host-guest system or sensors *etc.*[2] Preliminary results of palladium macrocyclic system and its potential inclusion properties will be discussed thereafter.

3.4.1.1 Synthesis of *ortho*-Carborane-Based Macrocycle

The 3-pyridylalcohol ligand **oCB-(L2)$_2$** has *syn*- and *anti*- diastereoisomers as previously mentioned. Due to the different solubilities of *syn*-**oCB-(L2)$_2$** and *anti*-**oCB-(L2)$_2$**, they can be separated during work-up from the synthesis. Only *syn*-**oCB-(L2)$_2$** was used in the following synthesis.

A macrocyclic dimer **PdCl$_2$(oCB(L2)$_2$)$_2$** is formed by mixing *syn*-**oCB-(L2)$_2$** and [PdCl$_2$(MeCN)$_2$] in DMF under air at ambient temperature (Scheme 3.4-2). Crystallization over a period of 2-4 days gave a yellow crystalline solid for **PdCl$_2$(oCB(L2)$_2$)$_2$** in high yield (82 %). Unlike in the case of the related 2-pyridylalcohol ligand **oCB-(L1)$_2$** (Chapter 3.3.1), palladium pincer complex formation did not occur with *syn*-**oCB-(L2)$_2$**. This is due to the position of the nitrogen atoms with respect to the boron cluster, farther away in the 3-pyridylalcohol ligand, and this does not allow BH activation and pincer formation. Therefore, the *syn*-**oCB-(L2)$_2$** ligand acts as a bridging ligand, and form a macrocyclic dimer as shown in Scheme 3.4-2.

Scheme 3.4-2: Synthetic scheme of the palladium macrocycle PdCl$_2$(*o*CB(L2)$_2$)$_2$.
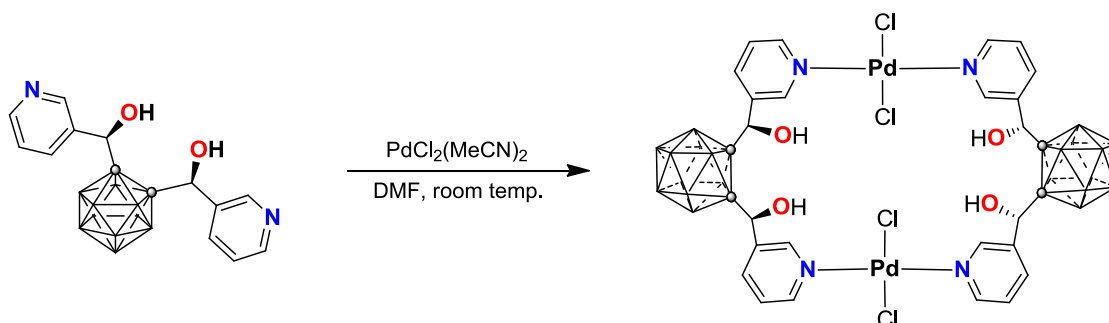
The new dimeric complex **PdCl$_2$(oCB(L2)$_2$)$_2$** has been fully characterized by NMR spectroscopy, single crystal and powder XRD and thermogravimetric analysis (TGA). As shown in the ^{1}H NMR spectra of the corresponding ligand and **PdCl$_2$(oCB(L2)$_2$)$_2$** (Figure 3.4-1), a clear downfield shift of the peaks have been observed on complex formation. In the ^{11}B NMR spectra, compared to the free ligand

syn-oCB-(L2)₂, further broadening of the signal is observed, which is probably due to the fluxional behaviour of **PdCl₂(oCB(L2)₂)₂** in solution.
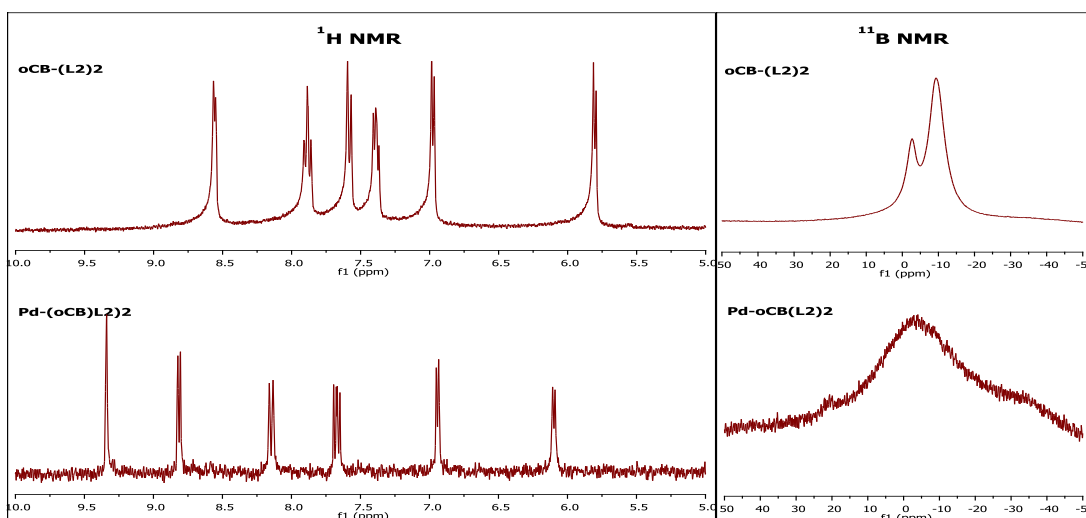

Figure 3.4-1: ¹H NMR spectra (left) and ¹¹B NMR spectra (right) of the complex **PdCl₂(oCB(L2)₂)₂** (bottom) and the corresponding *syn-oCB-(L2)₂* ligand (top) in DMSO-D₆.

The structure for **PdCl₂(oCB(L2)₂)₂·DMF** has been unequivocally established by X-ray crystallography (Figure 3.4-2). Analysis of the structure shows an inclusion compound, where the host (Pd-dimer) interact with the guest (DMF) by O-H···O and C-H···O hydrogen bonds (*vide infra*).
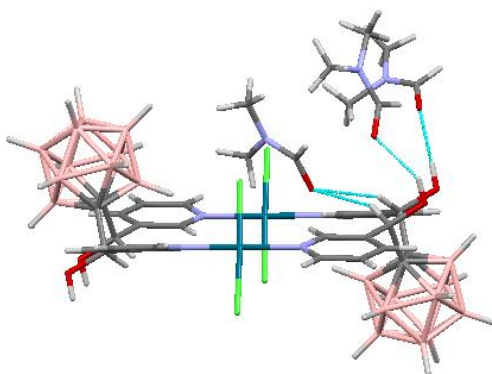
Figure 3.4-2: Structure of **Pd-oCB-(L2)₂·DMF**. Color code: B pink; C grey; H white; O red; N blue; Cl green; Pd prussian blue.

Figure 3.4-3 shows a molecule of the host from the structure where it can be seen the disposition of the carborane clusters and the hydroxyl moieties. As shown in Figure 3.4-3A, palladium is coordinated in square planar mode, where two pyridines coordinate to the Palladium in the *trans* fashion and two chloride ions complete the coordination. Besides, *syn-oCB-(L2)₂* coordinates with palladium with bite angle = 0° and the plane of pyridine rings is perpendicular to Cl-Pd-Cl. Moreover, the positions of carborane moieties are pointing opposite to each other (Figure 3.4-3B).
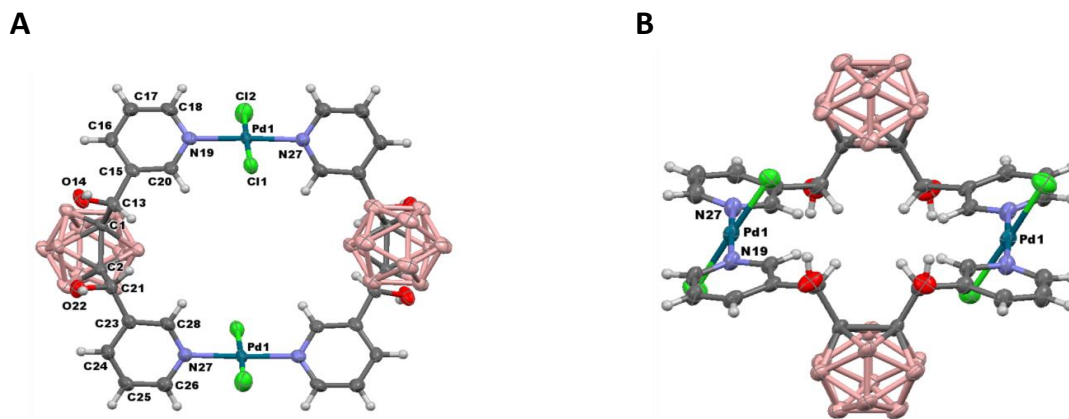
A

B

Figure 3.4-3: Labelled ORTEP diagrams for two different views of **Pd-oCB-(L2)₂**·DMF. The thermal ellipsoids are shown at the 80% probability level and the H atoms as fixed-size spheres of 0.18 Å. The DMF molecules and the H atoms attached to borons (pink) are omitted for clarity.

PXRD spectra of the **PdCl₂(oCB(L2)₂)₂**·DMF is shown in Figure 3.4-4. The experimental result fits with the calculated pattern of **PdCl₂(oCB(L2)₂)₂**·DMF from the crystal structure. This clearly proves that only a dimer is formed but no formation of other macrocycles or polymers in this system.

Pd-oCB(L2)₂ · DMF

Simulated **Pd-oCB(L2)₂** · DMF
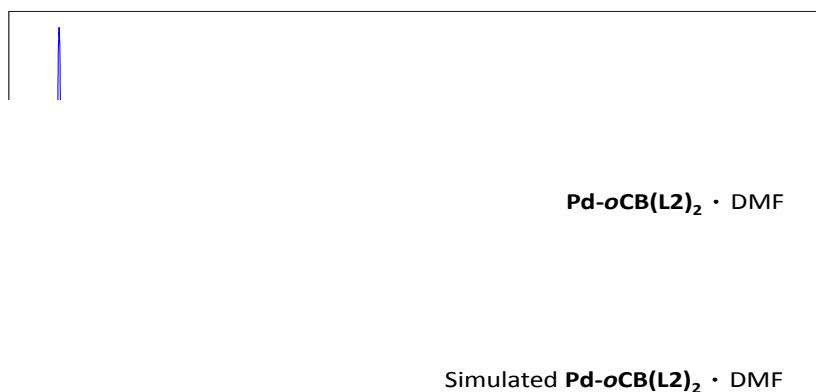
Figure 3.4-4: PXRD spectra of **Pd-oCB(L2)₂**·DMF (top) and the calculated **Pd-oCB(L2)₂**·DMF (bottom) from the crystal structure.

3.4.1.2 Inclusion Studies

The solid state structure for **PdCl₂(oCB(L2)₂)₂**·DMF constitutes an example of lattice inclusion compounds with small molecular guests.[3] Since the macrocyclic dimer possesses four hydroxyl groups that are not involved in the complex formation, it was expected that complex **PdCl₂(oCB(L2)₂)₂** shows inclusion behaviour. The macrocyclic dimer is insoluble in water, acetone, acetonitrile, 1,4-dioxane, diethyl ether, dichloromethane or n-hexane. It is however slightly soluble in very polar organic solvents such as DMF, DMSO, THF and EtOAc. Thus, six different inclusion

compounds were obtained by changing the solvent system that used for crystallization. In a typical crystallization experiment, the host **PdCl$_2$(oCB(L2)$_2$)$_2$** (c.a. 50 mg) was dissolved in 2-5 mL of solvent (guest) and the clear solution was allowed to evaporate slowly over a period of 2-4 days. This procedure afforded crystals for six inclusion compounds: **PdCl$_2$(oCB(L2)$_2$)$_2$**·SOLV (SOLV = DMF, DMSO-I, DMF/DMSO, EtOAc, THF). The structures for all inclusion compounds have been unequivocally established by X-ray crystallography. Crystallization solvent, host/guest stoichiometry, space group and calculated density (*D*) are given in Table 3.4-1. Figure 3.4-5 shows the molecular structures for all inclusion compounds.

Table 3.4-1. Details for crystallization solvent, Host:Guest Stoichiometry,

Space Group and Calculated Density (*D*; mg/m^3).

Inclusion Compound	Solvent of crystallization	Host/guest	Space Group	*D*
2·DMF-I	DMF	1:6	*P*-1	1.454
2·DMF-II	DMF	1:6	*P*2$_1$/*n*	1.390
2·DMSO-I	DMSO	1:8	*P*-1	1.490
2·DMF/DMSO	DMF + DMSO	1:2:4^a	*P*-1	1.470
2·EtOAc	EtOAc	1:7^a	*P*-1	1.360
2·THF	THF	1:6	*P*2$_1$/*c*	1.441

^{a} Olex2 was used to remove the electronic contribution of disordered solvent molecules per host:

5 DMSO molecules in **2**·DMSO-II, 2 DMSO molecules in **2**·DMF/DMSO and 3 EtOAc molecules in **2**·EtOAc.

A comparison of the crystal structures of the inclusion compounds of **PdCl$_2$(oCB(L2)$_2$)$_2$** revealed a remarkably constant conformation of the host molecule in all the structures. The solid state structures for the six inclusion compounds constitute examples of lattice inclusion compounds. Due to the presence of four alcohol moieties per host guests (Figure 3.4-3A), O-H···O and C-H···O hydrogen bonding play a dominant role in the molecular recognition and packing. One remarkable point is the host/guest stoichiometric ratios of 1:6 and 1:7, which are exceptionally high respect to the guest component.[3] The later indicates a high efficiency of guest accommodation. Detail analysis shows that the solvent molecules can be divided into two types: *in-guest* and *out-guest* (Figure 3.4-5, bottom right). The *out-guest* solvent molecules are hold by O-H···O or C-H···Cl hydrogen bonds and act as linkers to bridge two macrocyclic dimers together, whereas the in-guest solvent molecules are hold by C-H···O hydrogen bonds and located in the pores. This result is in good agreement with the TGA data for the **Pd-oCB-(L2)$_2$**·6DMF as shown below, in which two different types of solvents present in the materials. This host-guest system with various solvents is summarized and categorized as shown in Figure 3.4-5.

The inclusion compound **PdCl$_2$(oCB(L2)$_2$)$_2$**·DMF/DMSO deserves some comments as it contains two guest molecules of different nature. As shown in Table 3.4-1, the inclusion compound contains two DMF molecules and four DMSO ones (two were removed with Olex2) per host molecule. In this

particular structure, DMF and DMSO are acting as *out-guest* and *in-guest*, respectively. This means that the more polar and better hydrogen bond acceptor DMSO guest is occupying the site dominated by weak hydrogen bonding, whereas a somewhat worse hydrogen bond acceptor such as DMF is occupying the moderate hydrogen bonding sites.
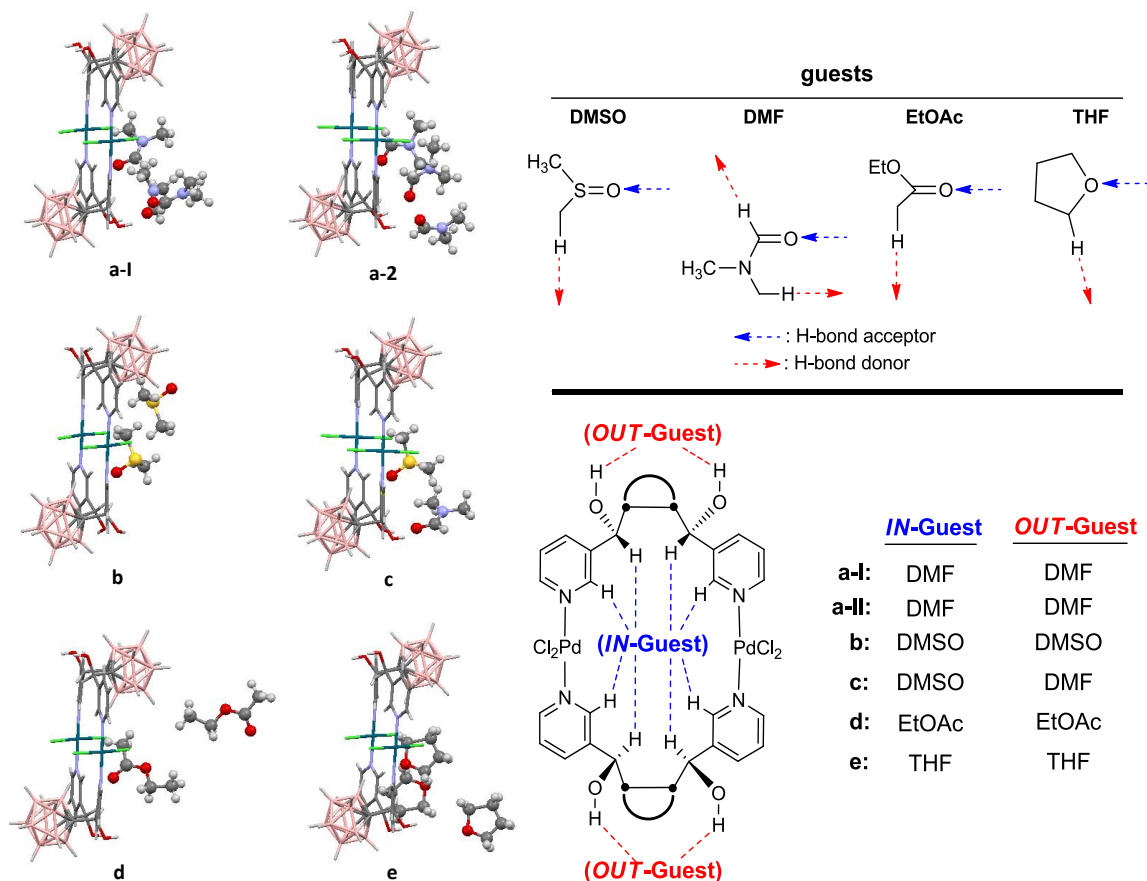

Figure 3.4-5: **Pd-oCB-(L2)₂** with the guest solvent (left): DMF (**a-1** and **a-2**), DMSO (**b**), DMSO/DMF (**c**), EtOAc (**d**) and THF (**e**); The illustration of the out-guest and in-guest of **Pd-oCB-(L2)₂** and the category of the corresponding guest molecules (right). Color code: B pink; C grey; H white; O red; N blue; S yellow; Cl green; Pd prussian blue.

Thermal analysis is a useful tool for the study of inclusion compounds. TGA is one of the most common techniques used. Figure 3.4-6 shows the thermogravimetric traces for the inclusion compounds **PdCl₂(oCB(L2)₂)₂**·DMF. It can be seen a 29.08 % weight loss from room temperature to around 250°C, that can be attributed to the removal of six DMF molecules (calc.: 29.04 %). Melting point measurement reveals however that this compound decomposes without melting in the range 170 − 180 °C. Further analysis of the TGA trace for **PdCl₂(oCB(L2)₂)₂**·DMF by establishing the derivative thermogravimetric analysis (DTG) curve (dashed trace in Figure 3.4-6) clearly shows three peaks at 155, 180 and 205 °C. It can be explained that a first loss of some DMF molecules occurred close to the DMF boiling point (153 °C), followed by other DMF molecules at 180 °C which leads to the decomposition. This scenario would be consistent with a first loss of *in-guest* DMF molecules

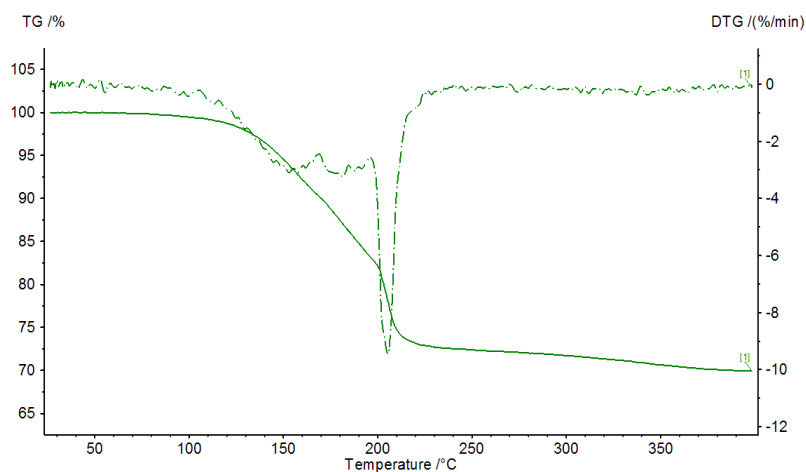(weakly hydrogen bonded), followed by the loss of *out-guest* DMF molecules (stronger hydrogen bonded).

Figure 3.4-6: TGA (solid line) and DTG (dotted line) curves of **Pd-oCB-(L2)$_2$** · 6DMF are shown in weight % vs temperature, heating rate: 10°C/min under nitrogen atmosphere.

TGA curves for five of the inclusion compounds are shown in Figure 3.4-7. Heating of the inclusion compounds showed chemical decomposition of the host on guest released. Melting point measurement and TGA analyses reveal that weight loss starts in the range 100 – 150 ^{o}C, followed by decomposition without melting in all cases in the temperature range 150 – 250 ^{o}C.
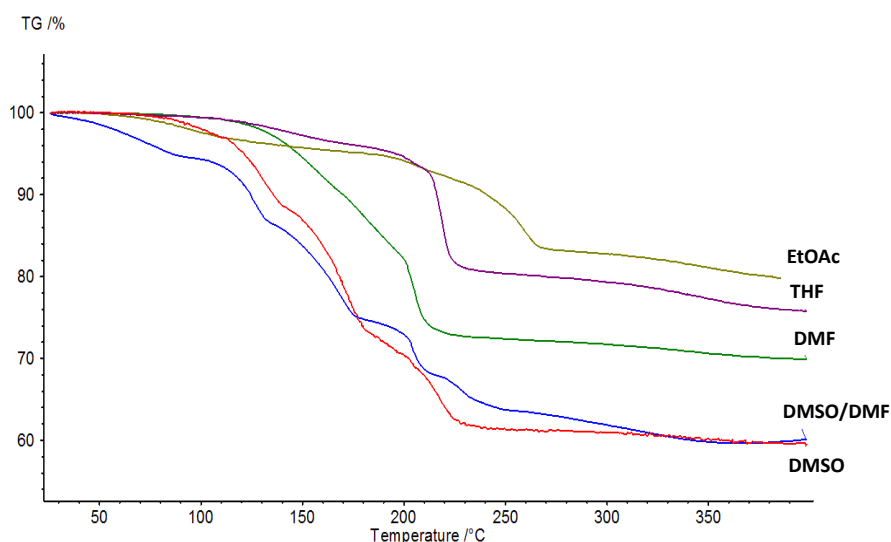
Figure 3.4-7: TGA curves of the five inclusion compounds with guest molecules EtOAc (olive green), THF (violet), DMF (green), DMSO (blue) and DMSO/DMF (red).

The preliminary results show that due to the presence of the alcohol groups, solvents that contain donor atom (*e.g.* S, O, N) are observed as guest molecules and form hydrogen bonds with the alcohol moieties.

3.4.2 Zinc (II) and Cobalt (II) Coordination Polymers: Preliminary Results

Zinc and cobalt are some of the most studied transition metals upon coordination chemistry because of the relatively low cost, various coordination geometries and applications on biological studies as well as material science. Zinc has various coordination number, although commonly found to form tetrahedral or octahedral complexes. In case of Cobalt, Cobalt (II) and (III) are normally found and mostly possess tetrahedral or octahedral geometry. In order to further study the coordination chemistry of the ditopic **CB-(L2)₂** and **CB-(L3)₂** ligands, 3-pyridylalcohol ligands *syn-o***CB-(L2)₂** and zinc/cobalt complexation have been performed. Different than the palladium dimer complex in Section 3.4.1, one dimensional (1D) coordination polymers **Zn-o*CB(L2)₂** and **Co-o*CB(L2)₂** have been formed.

3-pyridylalcohol ligands *syn-o***CB-(L2)₂** and ZnSO₄·7H₂O (1:1 ratio) were mixed in DMF under air at ambient temperature, slow evaporation of solvent afforded colourless square crystals that correspond to 1D Coordination Polymer (**Zn-o*CB-(L2)₂**) (Scheme 3.4-3). The purity was proven by elemental analysis, and the structure has been confirmed by single-crystal XRD.

Scheme 3.4-3: Synthetic procedure of thecoordination polymer (**Zn-o*CB-(L2)₂**)
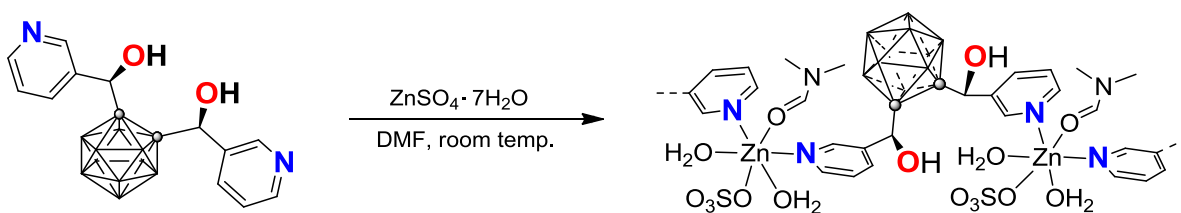
As illustrated in Figure 3.4-8, zinc ions show an octahedral geometry. Each zinc coordinates to two water molecules, one sulfate anion and one DMF molecule, and the ligand *syn-o***CB-(L2)₂** acts as a bridging linker to connect the zinc units. This 1D coordination polymer chain possesses an intramolecular O₃S-O···H-O hydrogen bond and an intermolecular O-H···O=C hydrogen bond between H₂O and DMF in each Zinc unit (Figure 3.4-8). The polymeric chains are connected through intermolecular O₃S-O···H-O hydrogen bonds as illustrate in Figure 3.4-9, giving a 3D structure.
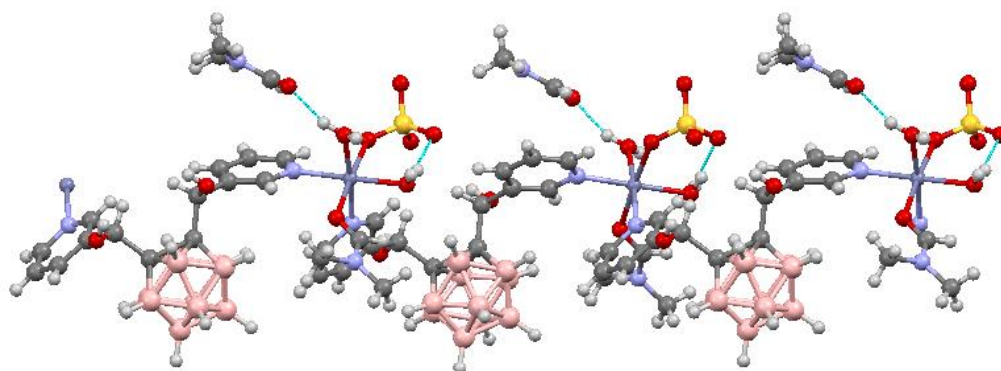

Figure 3.4-8: **Zn-o*CB-(L2)₂** 1D polymeric chain and illustration of the hydrogen bonds between the molecules and DMFs. Color code: B pink; C grey; H white; O red; N blue; S yellow; Cl green; Pd prussian blue.
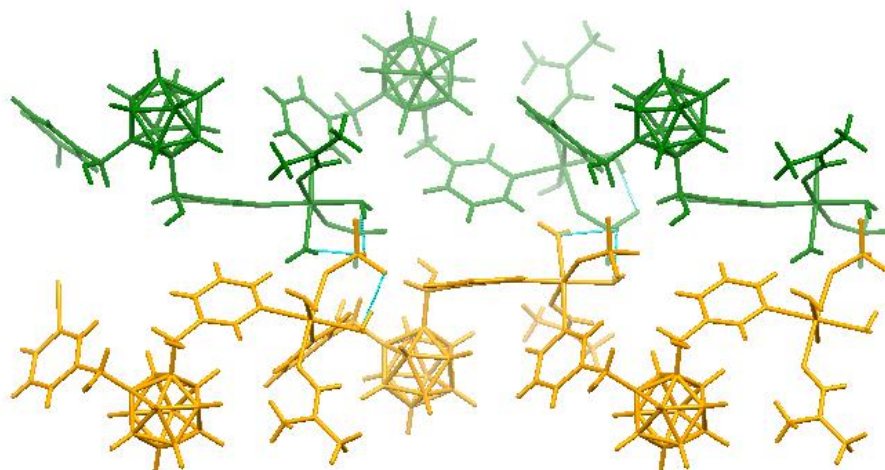
Figure 3.4-9: Illustration of **Zn-*o*CB-(L2)₂** of two polymeric chains (differentiated by green and yellow) that connected by O_3S-O⋯H-O hydrogen bonds.

TGA data of **Zn-*o*CB-(L2)₂** has been measured and is shown in Figure 3.4-10. The TGA shows three step weight loss. The first step weight loss (100 – 150°C) corresponds to the loss of water. The second step (150 – 250°C) corresponds to the release of DMF and further heating causes the decomposition of **Zn-*o*CB-(L2)₂**.
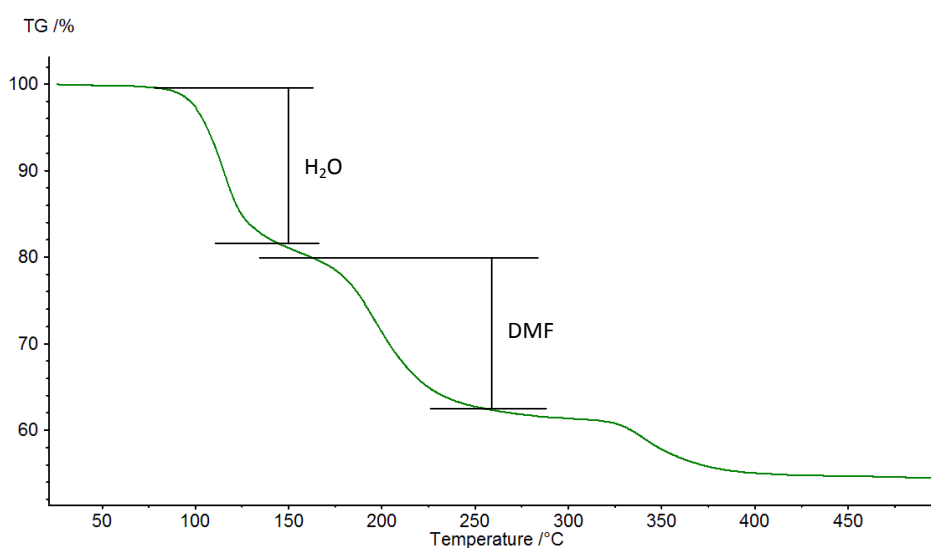

Figure 3.4-10: The TGA graph (weight % loss vs. temperature) of **Zn-*o*CB-(L2)₂**; heating rate: 10°C/min under N₂.

Further trial has been done with cobalt, following the same reaction procedure employed above. Thus, the reaction of $CoSO_4 \cdot 7H_2O$ with *syn-*o*CB-(L2)₂** in a 1:1 ratio in DMF afforded a violet crystalline solid that is tentatively assigned as **Co-*o*CB-(L2)₂**. Unfortunately, the crystals obtained were not of high quality and so the structure could not be solved by single-crystal XRD. However, the power diffraction pattern for the crystalline **Co-*o*CB-(L2)₂** (Figure 3.4-11, top) is similar to the simulated pattern to that of the zinc coordination polymer **Zn-*o*CB-(L2)₂** (Figure 3.4-11, bottom). The

remarkable similarities of the powder patterns suggest that the cobalt coordination polymer **Co-*o*CB-(L2)₂** has the same structure as the zinc coordination polymer.
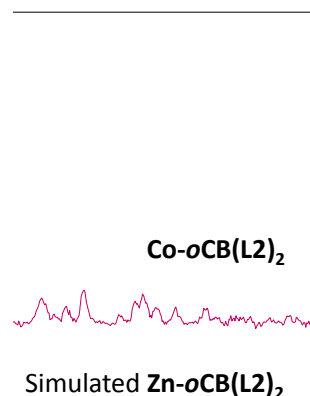

Co-*o*CB(L2)₂

Simulated **Zn-*o*CB(L2)₂**

Figure 3.4-11: Comparison of PXRD patterns of cobalt coordination polymer (**Co-*o*CB-(L2)₂**) (top) and the simulated **Zn-*o*CB-(L2)₂** pattern (bottom).

In summary, by using the same carborane-based 3-pyridylalcohol *syn-*o*CB-(L2)₂* ligand, and due to the rotational flexibility of the pyridine rings as well as the different coordination geometry of the metals (palladium: square planar; zinc, cobalt: Octahedral), different complexes (macrocyclic dimer **Pd-*o*CB-(L2)₂** and coordination polymers **Zn-*o*CB-(L2)₂** and **Co-*o*CB-(L2)₂**) can be obtained. The different coordination mode of the ligands from the corresponding complexes is extracted from the structures and shown in Figure 3.4-12. These results are the proof of concept that the *syn-*o*CB-(L2)₂* can be potentially applied as a good linker for further extension to 2D/3D networks.
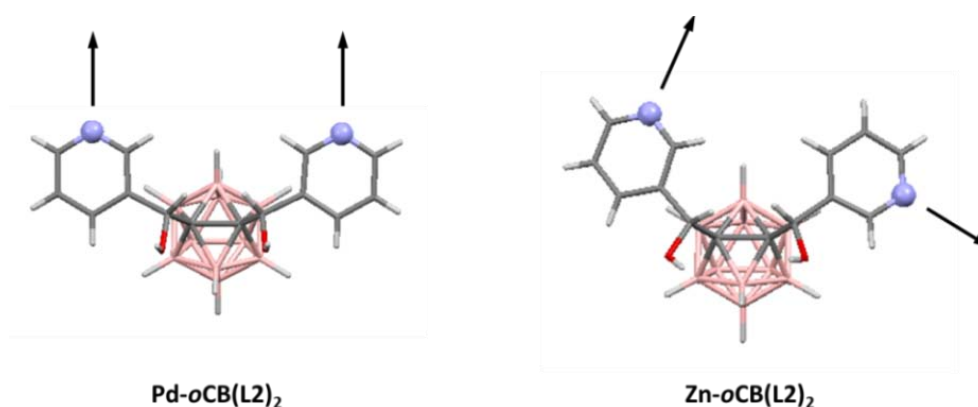

Pd-*o*CB(L2)₂　　　　**Zn-*o*CB(L2)₂**

Figure 3.4-12: The extracted coordination modes of the *syn-*o*CB-(L2)₂* from **Pd-*o*CB(L2)₂** (left) and **Zn-*o*CB(L2)₂** (right) from the corresponding crystal structures.

References

[1]   (a) Q. Zhang, Li, He, J-M. Liu, W. Wang, J. Zhang, C-Y. Su. *Dalton Trans*, **2010**, *39*, 11179 (b) F. Maharaj, R. Bishop, D. C. Craig, P. Jensen, M.L. Scudder, N. Kumar, *Cryst. Growth & Des.***2009**, *9*, 1334 (c) L. Dobrzanska, G. O. Lloyd, H. G. Raubenheimer, L. J. Barbour *JACS*, **2005**, *127*, 13134 (d) L. S. Shimizu, A. D. Hughes, M. D. Smith, M. J. Davis, B. P. Zhang, H-C zur Loye, K. D. Shimizu, *JACS*, **2003**, *125*, 14972.

[2]   (a) Y. Li, L. Liang, S. Zhang, X. Su, J. Lan; *Chem. Commun.***2010**, *46*, 3938 (b) P. Liao, B. W. Langloss, A. M. Johnson, E. R. Knudsen, F. S. Tham, R. R. Julian, R. J. Hooley, *Chem. Commun.***2010**, *46*, 4932. (c)

[3]   E. Weber, S. Nitsche, A. Wierig, I. Csoregh, *Eur. J. Org. Chem.*, **2002**, 856.

3.5 N,O-Type *ortho*- and *meta*-Carborane-Based Metal-Organic Frameworks

Metal-organic frameworks (MOFs) have received intense studies for decades because of the rigid skeletons and various potential applications as previously mentioned. Introduction of carborane into the backbone is expected to significantly enhance the chemical and thermal stability of MOFs (Chapter 1.3.3). The mixed-ligand methodology to synthesize MOFs presents several advantages over those using only one ligand as shown in Chapter 1.3. One of the most important benefits of this method is that the resultant MOFs in the mixed linker approach is neutral and their porosity (if present) are not blocked by counter ions. Furthermore, the combination of different types of ligands allows more decorative abilities, such as functionalizing the internal surface and tuning the pore size or surface area of the MOFs by using linkers with different sizes and/or lengths.[1] However, some drawbacks remain challenges as explained earlier (Chapter 1.3.2) such as the water stability or gas selectivity.

The focus in the present chapter is on the design, synthesis, structural variation and topologies of MOFs composed of mixed linkers (one anionic carboxylate and the other neutral pyridylalcohol ligands) system. Incorporating the flexible carborane-based pyridylalcohol ligands (*o*CB-(L2)$_2$, *m*CB-(L2)$_2$ and *m*CB-(L3)$_2$) (see Chapter 3.4) with different carboxylic acids by solvothermal method, several mixed-ligand MOFs have been successfully synthesized. Characterizations and structural studies will be reported in this chapter. Moreover, the water stability and the gas sorption of some of the MOFs will be discussed thereafter.

### 3.5.1 *ortho*-Carborane-Based Mixed Ligand MOFs

3.5.1.1 Synthesis with *ortho*-Carborane-Based 3-Pyridylalcohol Linker

The initial studies have been done by introducing 1,4-benzenedicarboxylate (BDC) as the anionic linker in combination with the *anti*-*o*CB-(L2)$_2$ and Zn(NO$_3$)$_2$·6H$_2$O in 2 mL solvent. Solvothermal strategy was used for screening by mixing the ligands and metal salt in different ratio and heat for 24 to 48 hours in DMF, DMF/EtOH or DMF/H$_2$O/EtOH as the reaction media. FTIR-ATR was used as a preliminary analysis to verify whether the carborane cluster was present in the raw materials (typical B-H stretching peak in the range of 2600 – 2400 cm^{-1}), followed by PXRD measurement to identify the crystalline materials. The obtained crystals were measured by X-ray diffraction to determine the structure, and the phase purity of the bulk material can then be confirmed by comparing with the simulated pattern from the corresponding crystal structures.

The formation of *anti*-*o*CB-MOF-1 is confirmed by synchrotron single-crystal XRD and the optimal condition to get the *anti*-*o*CB-MOF-1 were found to be Zn(NO$_3$)$_2$·6H$_2$O, *anti*-*o*CB-(L2)$_2$, and 1,4-BDC in 2:1:1 ratio in 2mL of DMF/ethanol (1:1) by heating at 85 °C for 48 hours. However, a mixture was found to be formed in the bulk material, which contained the desired product *anti*-*o*CB-MOF-1 and the well-known MOF-5 (components: zinc ions and 1,4-BDC)[2] (Scheme 3.5-1; top). Although the

formation of MOF-5 is thermodynamically favoured, it is not stable in aqueous media or presence of acid or base.[3] Therefore, different trials have been done by addition of water, benzoic acid, 0.1M dilute HCl or 2-methylimidazole (2-Hmim) as additives. The result showed that 2-Hmim can significantly reduce the formation of MOF-5. Optimized condition was found by using 2 equivalent of 2-methylimidazole to get the *anti-o***CB-MOF-1** in a pure phase. Therefore, by mixing $Zn(NO_3)_2 \cdot 6H_2O$, *anti-o***CB-(L2)₂**, 2-Hmim and 1,4-BDC in the same solvent mixture and followed by heating at 85 °C for 48 hours, crystalline solid *anti-o***CB-MOF-1** (24.3 mg, yield 56 %) can be obtained (Scheme 3.5-1; bottom).

Scheme 3.5-1: Synthetic scheme of *anti-o***CB-MOF-1** without 2-Hmim (top) and with 2-Hmim (bottom).
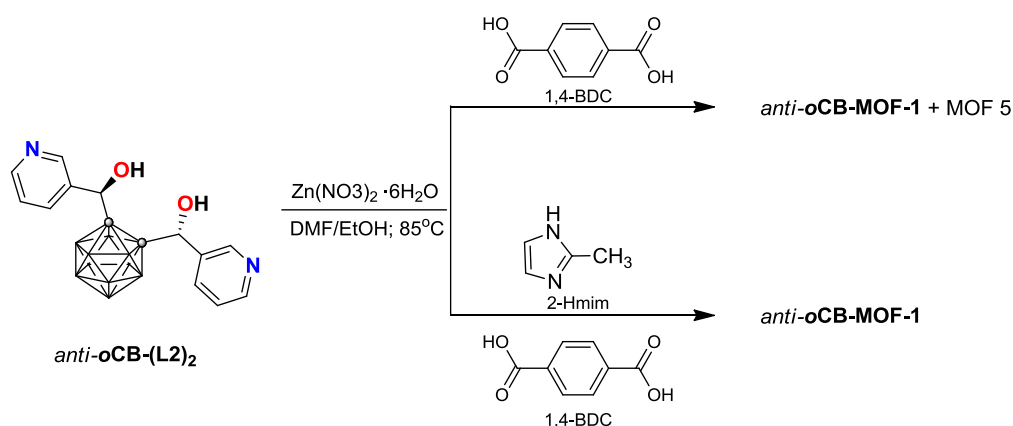
The phase purity is confirmed by PXRD as shown in Figure 3.5-1. Peaks from MOF-5 can be observed (highlighted in red) in the resulting product from the synthesis in the absence of 2-Hmim (green). Those are however totally suppressed by addition of 2-Hmim during the synthesis in the presence of 2-Hmim (blue).
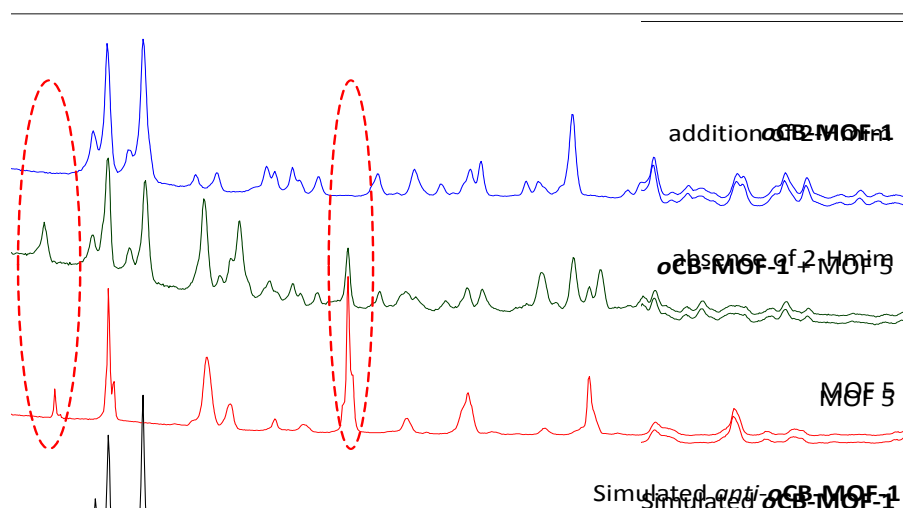

Figure 3.5-1: Synthetic scheme of *anti-o***CB-MOF-1** without 2-Hmim (top) and with 2-Hmim (bottom).

The suppression of MOF-5 formation during the synthesis of *anti-o*CB-MOF-1 by adding 2 equivalence of 2-Hmim, can be explained by several mechanisms.[4] Most likely, the basicity of 2-Hmim (p*Ka* (H_2O) = 14.2) plays a key role in the mechanism as it is a stronger base than the pyridylalcohol ligands (p*Ka* (H_2O) for pyridine derivatives oscilates between 5-7). Notice that no base was added to deprotonate the carboxylic acid, so that the pyridylalcohol ligands *anti-o*CB-(L2)$_2$ and/or the 2-Hmim might act as the base. This could explain that in the absence of 2-Hmim, the *anti-o*CB-(L2)$_2$ ligands are protonated at the nitrogen atoms of the pyridine, therefore avoiding the coordination to the metal. In this context, MOF-5 will be formed by the reaction of Zn and anionic BDC. On the contrary, the presence of more basic 2-Hmim will preferentially deprotonate the carboxylic acid, leaving the pyridyl units of *anti-o*CB-(L2)$_2$ ready for coordination to the Zn metal atoms. Consistently with this, addition of less than 2 equiv. of 2-Hmim cannot totally suppress the MOF-5 formation. On the other hand, overdose of 2-Hmim (> 3 eq.) would block the formation of the desired product *anti-o*CB-MOF-1 because the excess of 2-Hmim would act as competitive ligands to bind to the metal ion centers.[4] Therefore, appropriate amount of 2-Hmim is necessary in this reaction.

3.5.1.2 Structural Analysis and Characterizations

Complete characterizations have been done by FTIR-ATR, PXRD, SEM, elemental analysis, TGA, Brunauer, Emmett and Tellar (BET) surface area and gas sorption (N_2, CO_2 and CH_4). Figure 3.5-2 shows the crystal structure of *anti-o*CB-MOF-1 and its three dimensional structure.

*anti-o*CB-MOF-1 is a porous 3D structure built on rhombus-shaped [$Zn_4O_2(CO_2)_4$] tetra-nulcear Zinc clusters that are connected through four BDC^{2-} ligands (Figure 3.5-2A), the [$Zn_4O_2(CO_2)_4$] clusters containtwo tetrahedral (green circled) and two octahedral (black circled) Zn^{2+} ions, and two μ_3-oxo moieties (O^{2-}). Coordination of the 1,4-BDC ligands to the Zn clusters form a 2D layer as shown in Figure 3.5-2B, and the *anti-o*CB-(L2)$_2$ act as bridging linkers to connect the 2D layer and form the 3D network (Figure 3.5-2C). Figure 3.5-2D shows the accessible pores of the 3D framework of *anti-o*CB-MOF-1 alone the *c* axis.

As mentioned, FTIR-ATR is a useful technique as a screening tool for determining the presence of carborane in the raw materials of the MOFs before further processing and analyses. The spectrum of *anti-o*CB-MOF-1 shows a typical B-H stretching from carborane cluster at around 2530 cm^{-1}, the similar position of the B-H stretching as the free ligand *anti-o*CB-(L2)$_2$ (c.a. 2540 cm^{-1}) also an indication of no degradation of the *closo*-carborane to an *nido*-cluster. Moreover, the intense C=O stretching of the carboxylic acid can be observed near 1590 cm^{-1} as well as the corresponding CO band for the DMF solvent moelcules at 1647 cm^{-1} (Figure 3.5-3).
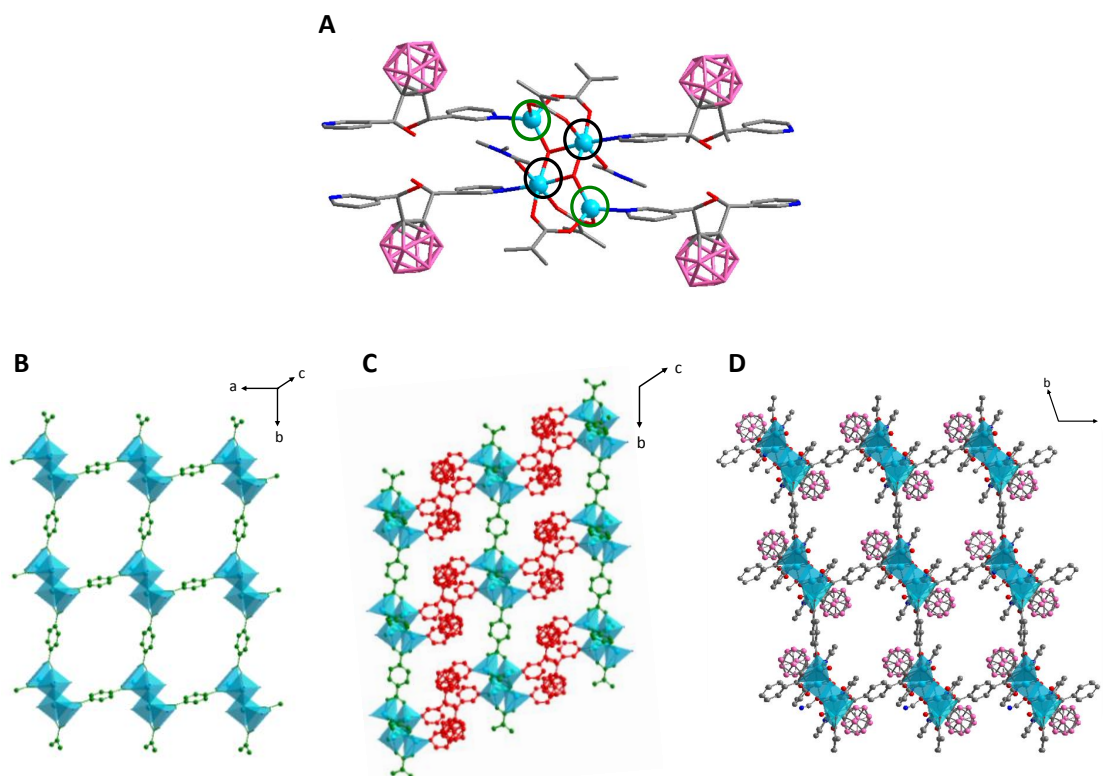
Figure 3.5-2: Structure of *anti-o*CB-MOF-1. A: The organization of the *anti-o*CB-(L2)$_2$around the tetranuclear Zn clusters. B: 2D-Zn (II)-based layer. C: 3D Zn (II) framework by *anti-o*CB-(L2)$_2$bridging linkers. D: 3D network, in which the carborane cages are pointed towards the accessible pores along the *c*-axis.
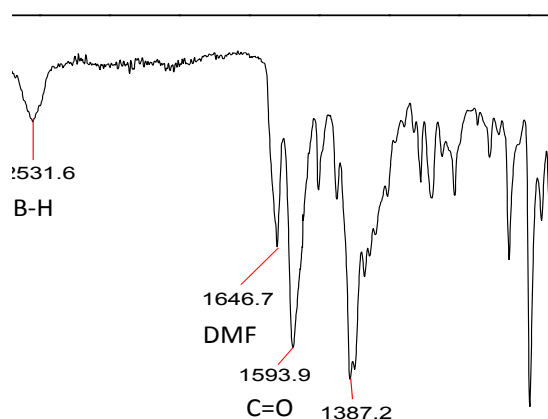

Figure 3.5-3: FTIR-ATR spectrum of *anti-o*CB-MOF-1

A reasonable agreement is found between the PXRD pattern of the as-made *anti-o*CB-MOF-1 and that calculated from the XRD (Figure 3.5-4). Combined synchrotron PXRD and elemental analysis measurements suggest the presence of amorphous domains (5 – 10 %) in the crystalline bulk material.
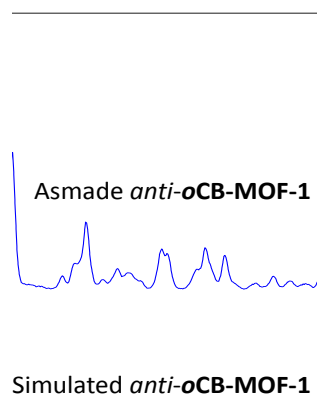
Asmade *anti-o*CB-MOF-1

Simulated *anti-o*CB-MOF-1

Figure 3.5-4: PXRD patterns of as-made *anti-o*CB-MOF-1 (top) and simulated *anti-o*CB-MOF-1 (bottom)

SEM images of the as-made *anti-o*CB-MOF-1 at 200 μm and 50 μm magnifications are shown in Figure 3.5-5. The material crystalized as micrometer size blocks. The magnified image (Figure 3.5-5b) shows the intergrown of the crystalline phase and the amorphous or semicrystalline phase, which is in a good agreement with the PXRD data of the as-made *anti-o*CB-MOF-1.
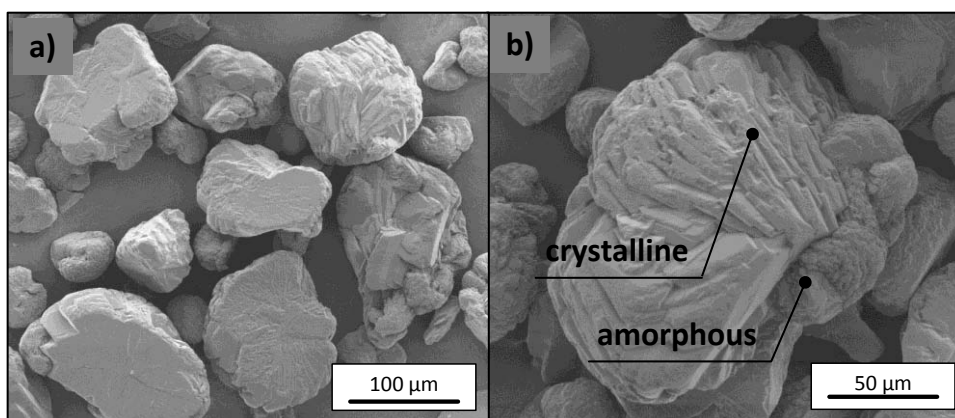

Figure 3.5-5: SEM images of the as-made *anti-o*CB-MOF-1 in (a) 200 μm and (b) 50 μm.

TGA data of the as-made *anti-o*CB-MOF-1 (Figure 3.5-6, black) shows around 24 % weight loss between 150 to 250 $^{\circ}$C corresponding to the DMF (b.p.: 153 $^{\circ}$C) solvent molecules. This result is in good agreement with the elemental analysis data, where the amount of the DMF molecules from the proposed formula $[Zn_4(C_8H_4O_4)_2(C_{14}B_{10}N_2O_2H_{22})_2(\mu\text{-}O)_2(DMF)_2]\cdot(DMF)_4$ is around 24.5 %.

MOFs are attractive due to many properties, especially permanent microporosity and large internal surface areas. For most of the applications, it is necessary to remove guest solvent molecules from the pores of the MOF without the loss of porosity, a process termed 'activation'. Traditional activation is done by heating the MOF material under vacuum. The activation of *anti-o*CB-MOF-1 was done by conventional heating at 100°C for 15 hours under high vacuum (10^{-3} mbar) and is proven by the TGA data as shown in Figure 3.5-6 (blue).

Figure 3.5-6: TGA data of asmade *anti-o*CB-MOF-1 (black) and activated *anti-o*CB-MOF-1(blue) in weight loss (%) vs. temperature (^{o}C)

The BET surface area of the activated *anti-o*CB-MOF-1 was measured under N_2 at 77K. The result shows a type II isotherm which is an indication of a non-porous material (Figure 3.5-7A). However, when applying CO_2 at 195 K, a type I isotherm is obtained, which is a typical isotherm for microporous materials and it is in good agreement with the crystal structure (accessible pore diameter of *anti-o*CB-MOF-1 = c.a. 6.5 Å). The resulting BET surface area for *anti-o*CB-MOF-1 under CO_2 is 296 m^2g^{-1} (Figure 3.5-7B). The pore volume is 0.18 cm^3g^{-1} (calculated by using the D-R equation[5] (eq. 3.5-1), which is slightly smaller than the calculated pore volume from the single crystal structure (0.21 cm^3g^{-1}, calculated by PLATON).

$$ln(V_a) = ln(V_o) - \frac{kR^2T^2}{\beta^2}[\ln(p_o/p)]^2 \qquad (3.5\text{-}1)$$

Where:

V_a = adsorbed volume of adsorbate; (cm^3/g STP)

V_o = micropore volume; (cm^3/g STP)

k = constant

R = gas constant; (kJ/mol K)

T = temperature; (K)

β= affinity constant of adsorbate relative to saturation pressure

p_o = saturation pressure of adsorbate; (mmHg)
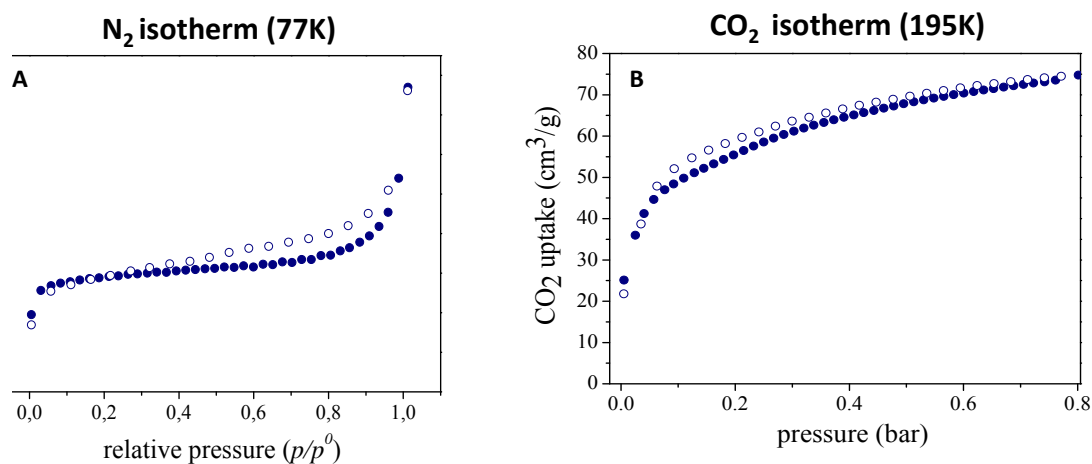
p = pressure of adsorbate; (mmHg)

N₂ isotherm (77K) A — relative pressure (*p/p⁰*)

CO₂ isotherm (195K) B — CO_2 uptake (cm³/g) — pressure (bar)

Figure 3.5-7: BET surface area measurement. A: N_2 isotherm at 77K and B: CO_2 isotherm at 195K.

The dominant factors for gas sorption are depending on the size/shape of the accessible pore, the surface character of the MOFs and the diffusion rate of the gas molecules.[6] The kinetic diameter of N_2 and CO_2 are 3.64 Å and 3.30 Å respectively.[7] The kinetic diameters for small gases are widely quoted in gas adsorption studies as they offer a very useful guideline in considering gas selectivity by size sieving.
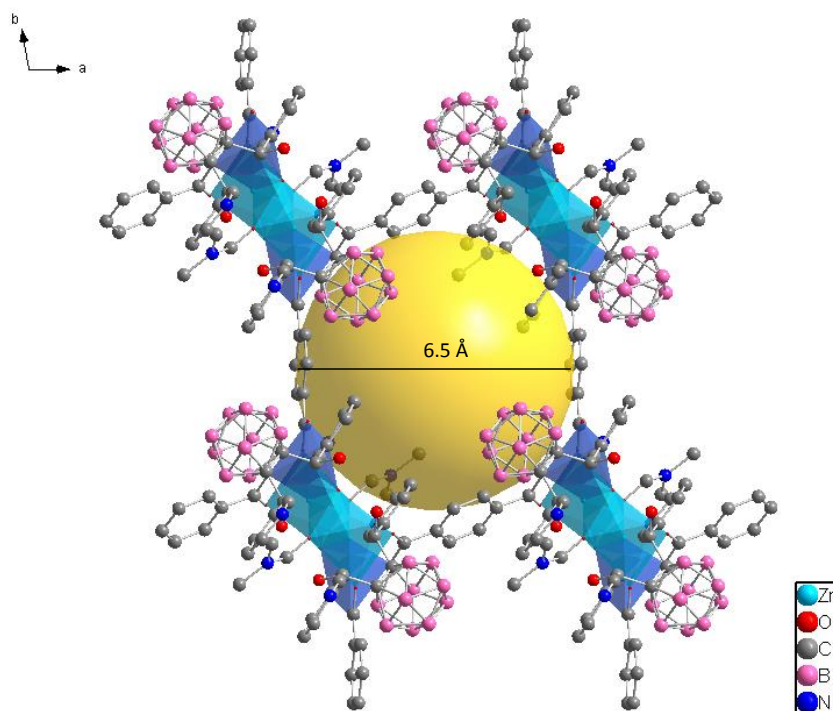

Figure 3.5-8: Representation image of the cavity (yellow ball) of*anti-o*CB-MOF-1 along *c* axis. Estimated diameter of the pore is approximately 6.5 Å. Octahedral zinc is represented by light blue polyhedral, and unsaturated tetrahedral zinc is represented by dark blue polyhedral.

Although the size of N_2 is bigger than CO_2, the measured accessible pore size of *anti-o*CB-MOF-1 is around 6.5 Å, so the influence of the pore size towards the gas sorption can be ruled out. However, as illustrates in Figure 3.5-8, the unsaturated zinc ions from the metal clusters (dark blue polydedra)

are exposed towards the pore, which enhance the CO_2 adsorption due to its large quadrupole moment (CO_2: 13.4 x 10^{-40} Cm^2; N_2: 4.7 x 10^{-40} $Cm^{2[6]}$). In addition, the polar alcohol groups from the *anti-o*CB-(L2)$_2$ ligand that are exposed to the pore also enhance the affinity towards CO_2 due to the higher polarizability over N_2 (CO_2: 29.1 x 10^{-25} cm^3; N_2: 17.6 x 10^{-25} $cm^{3[6]}$).

The sorption of CO_2 and CH_4 has been measured at 273K and 298K respectively (Figure 3.5-9A). The result shows *anti-o*CB-MOF-1 has both CO_2 and CH_4 uptake abilities. As explained, the adsorption of CO_2 in the materials is due to its large quadrupole moment and high polarizability. The adsorption of CH_4 can be explained by the presence of the hydrophobic carborane clusters in the pore which enhance the intermolecular interaction to CH_4 through Van der Waals forces, and also the opened-metal sites from the zinc clusters which increase the binding strength through Coulomb interactions due to the high polarizability (CH_4: 26.0 x 10^{-25} cm^3).[8]

Isosteric heat of adsorption (*Qst*) is a commonly used determining factor to describe the binding strength between the gas and the porous materials, that is, the higher the *Qst* value, the stronger the binding strength. Figure 3.5-9B shows *Qst* of both CO_2 and CH_4 versus the gas uptakes, where the *Qst* is calculated using the virial-type equation and the adsorption isotherm (273K and 298K) of CO_2 and CH_4 respectively (eq. 3.5-2 and 3.5-3).[9]

$$\mathrm{In}P = \mathrm{In}N + \frac{1}{T}\sum_{i=0}^{m} a_i N^i + \sum_{i=0}^{n} b_i N^i \qquad (3.5\text{-}2)$$

The isosteric heat of adsorption (Qst) is then calculated by using the following expression.

$$Qst = R \sum_{i=0}^{m} a_i N^i \qquad (3.5\text{-}3)$$

Where:

P: pressure of the adsorption at T_1 = 273K and T_2 = 298K

N: quantity of gas adsorbed

T: temperature

a_1 and b_1: virial coefficients

m and n: the number of coefficients required to describe the isotherm

R: gas constant

The *Qst* for CO_2 lies in a range of 28 kJmol^{-1} to 32 kJmol^{-1}, so that it is moderate when compared to the reported MOFs (12 − 96 kJmol$^{-1[9]}$). On the other hand, the *Qst* for CH_4 at zero-coverage is 20kJmol^{-1}and gradually increase to 23 kJmol^{-1}, this result shows the *anti-o*CB-MOF-1 has high affinity to CH_4 even at 1 bar compare to the reported materials (3.9 − 30 kJmol^{-1} at 35 bar[8]). However, a higher *Qst* of CO_2 over CH_4 in *anti-o*CB-MOF-1 is observed. It is known that CO_2 and CH_4 can interact with the pore surface differently depending on their nature (quadrupole moment and polarizability). As the polarizability of CO_2 and CH_4 are comparable, it might be explained by the stronger interaction

between the unsaturated opened-metal sites with CO_2 due to its large quadrupole moment, whereas the quadrupole moment of CH_4 is zero.
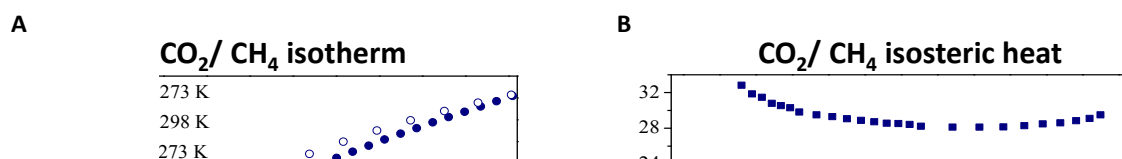
A

CO_2/ CH_4 isotherm

273 K
298 K
273 K

B

CO_2/ CH_4 isosteric heat

32
28

Figure 3.5-9: A: Sorption of CO_2 and CH_4 at 273 K (blue) and 298 K (red), and B: the corresponding isosteric heat of adsorption (Qst) that calculated by virial-type equation and the adsorption of CO_2 and CH_4 isotherms.

As explained, *anti-o*CB-MOF-1 is porous to CO_2 but not N_2, and also shows good CO_2 and CH_4 affinity because of the unique features of the pores. It is worth mention that, although the gas uptake capacity is rather small due to the low surface area, the presence of the hydrophobic carborane clusters induces a high CH_4 binding strength (Qst = 20 − 23 kJmol^{-1}). This result creates a positive alternative to incorporate carborane clusters for the development of high CH_4 storage materials.

3.5.1.3 Stability in Water, Organic Solvents, Acidic and Basic Media

As previously mentioned, one of the drawbacks of MOFs is their low stability towards humidity. By introducing the hydrophobic carborane clusters in the backbone of MOFs, enhancement of the water stability of *anti-o*CB-MOF-1 is expected. Herein, the water resistance of *anti-o*CB-MOF-1 will be demonstrated by a combination of PXRD, water vapour sorption and contact angle measurements. In addition, stability in different solvents (methanol, acetone and $CHCl_3$) and also in different pH solutions (pH 2, 4, 6, 8, 10 and 12) will be shown in the following.

The shape of the water vapour isotherm can provide direct information on the hydrophobicity or hydrophilicity of the material.[10] Thus, the water vapour sorption of *anti-o*CB-MOF-1 was measured at 298K (Figure 3.5-10). The water uptake (0.025 g per 1 g of sample) and the shape of the isotherm (typical Type II isotherm for nonporous materials) clearly show a strongly hydrophobic material that adsorbs very little water over the entire relative pressure range. This resulting water vapour sorption behavior of *anti-o*CB-MOF-1 is comparable to that of the hydrophobic **ZIF-8** (0.02 gg^{-1}), shown in Figure 3.5-10B.[11]
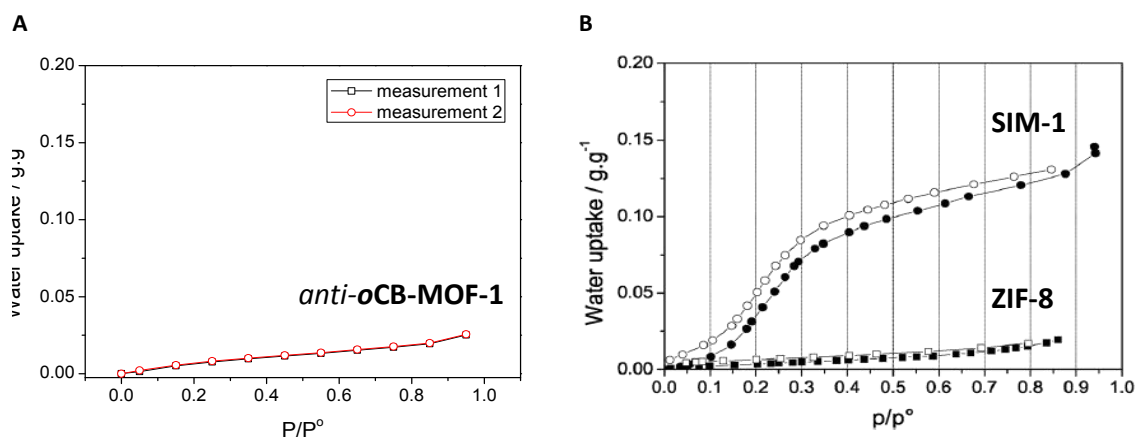
Figure 3.5-10: A: water vapour uptake of *anti-oCB-MOF-1* and B: water uptake of the reported ZIF-8 and SIM-1 which is isoreticular to ZIF-8.[11]

The contact angle, θ_c, measurement is a useful tool to indicate the wettability of the materials by a liquid, in this case, water. It is defined geometrically as the angle formed by a liquid at the three-phase boundary where a liquid, gas and solid intersect (Figure 3.5-11). Materials with contact angle (θ_c) lower than 90° are defined as hydrophilic. Hydrophobic materials on the other hand, have θ_c higher than 90°, and when contact angles are over 150°, these material are defined as super hydrophobic.
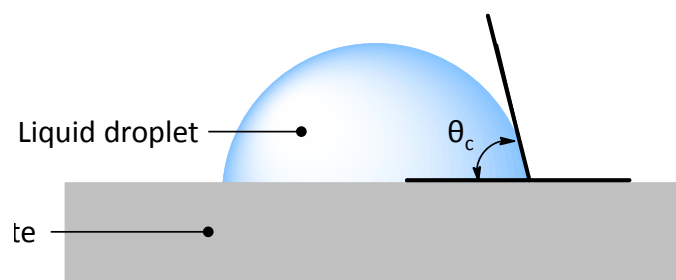
Figure 3.5-11: Illustration of contact angle (θ_c) measurement.

The as-made *anti-oCB-MOF-1* was grinded to fine powder and packed by a glass slide to create a flat surface. θ_c of *anti-oCB-MOF-1* has been measured with 1 µm of water droplet (Figure 3.5-12). The result shows *anti-oCB-MOF-1* has θ_c = 138°, and therefore *anti-oCB-MOF-1* is a clear hydrophobic material.
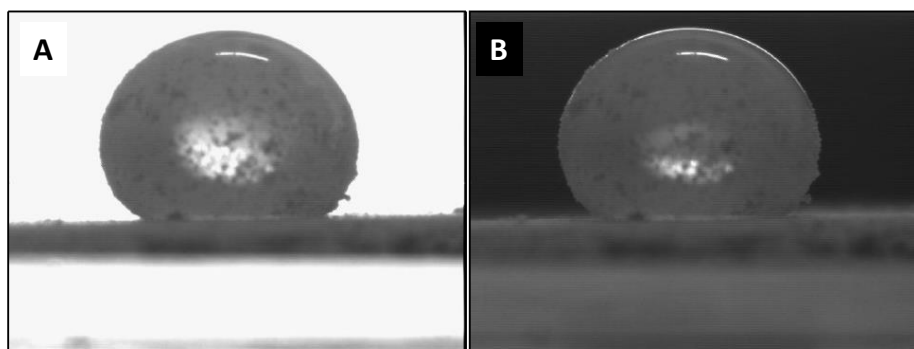

Figure 3.5-12: Contact angle of *anti-oCB-MOF-1* a): bright background and b): dark background.

Further proof for the hydrophobicity of *anti-o*CB-MOF-1 was done by a simple experiment in a pipette. As shown in Figure 3.5-13, the *anti-o*CB-MOF-1 powder was packed on the top of a piece of cotton as shown in picture a. A pink CH_2Cl_2 layer coloured by Rhodamine B was added first, followed by a water layer (1:1 ratio) on top of the packed *anti-o*CB-MOF-1 and the interface was marked as pointed by the red arrow in the figure. The level of the CH_2Cl_2 layer was monitored and recorded through time (Figure 3.5-13, top). As observed, the level of the CH_2Cl_2 layer is reducing during 2.5h, when all CH_2Cl_2 layer passed through the *anti-o*CB-MOF-1.
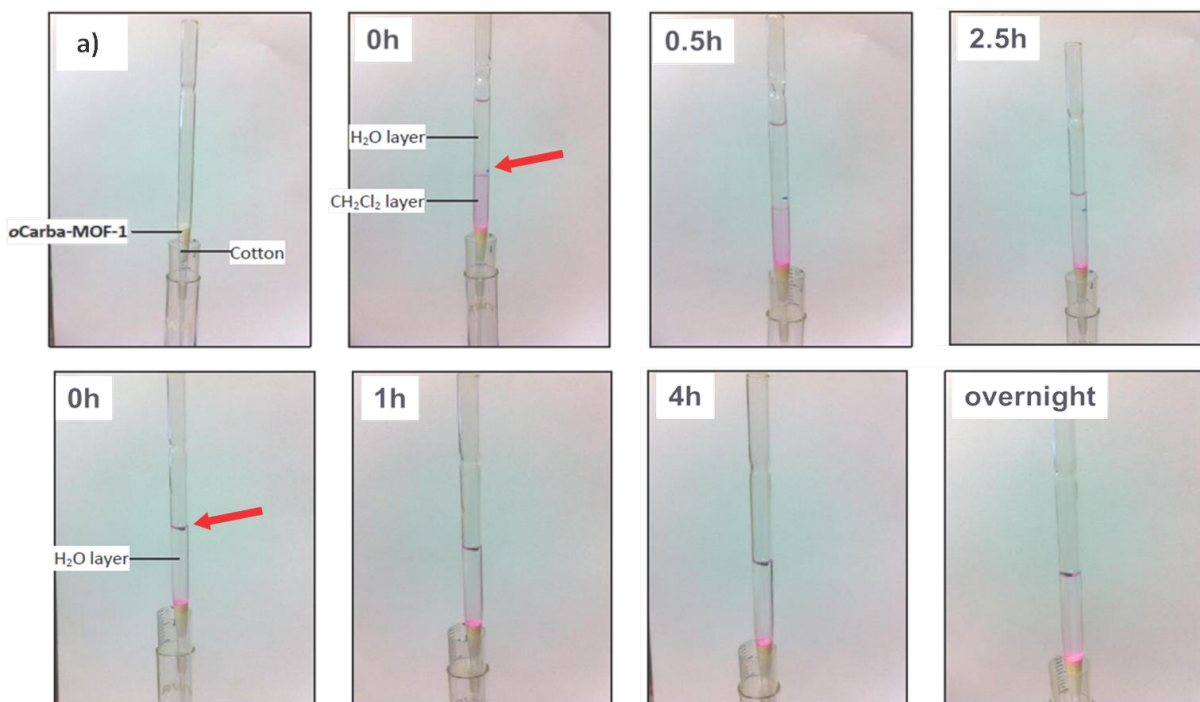

Figure 3.5-13: hydrophobicity test with H_2O/CH_2Cl_2 coloured by Rhodamine B layers. (a) Packed powder of *anti-o*CB-MOF-1 in the pipette. The level of CH_2Cl_2 layer at 0h, and after 0.5h and 2.5h (top); and the level of H_2O layer at 0h, after 1h, 4h and overnight (bottom). Red arrows indicate the initial level of CH_2Cl_2 and H_2O at 0h.

A new line was then drawn to mark the initial level of the water layer (Figure 3.5-13, bottom). As can be seen in the figure, the water level remained unchanged overnight (more than 24h), indicating that the water cannot pass through *anti-o*CB-MOF-1. Since the kinetic diameter of CH_2Cl_2 is larger than water (CH_2Cl_2: 4.89 Å; H_2O: 2.64 Å), so the influence of the size can be ruled out, thus, this result can be explained by the hydrophobic property of *anti-o*CB-MOF-1.

Water resistance of the *anti-o*CB-MOF-1 has been also studied by PXRD (Figure 3.5-14). In an initial experiment, a sample of as-made *anti-o*CB-MOF-1 was immersed in water for 15h at room temperature. The PXRD of the solid sample after being in water (red) showed a crystalline phase very similar to the one of the as-made sample (black) but with clear differences in the peak displacements. Interestingly, immersion of the water treated sample in DMF for 15h showed a complete conversion to the as-made phase (blue). These results clearly show that the *anti-o*CB-MOF-1 is water resistant

for at least 15h. This makes of *anti-o*CB-MOF-1 a thermodynamically water stable MOF, according to the classification by Walton and coworkers.[10]
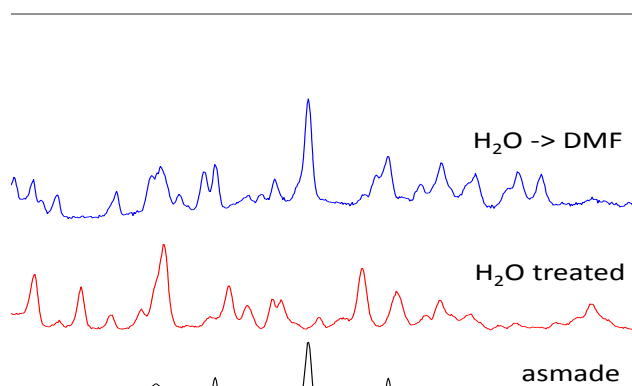

Figure 3.5-14: PXRD of as-made *anti-o*CB-MOF-1 (black), water treated *anti-o*CB-MOF-1 (red) and the re-addition of DMF to the water treated *anti-o*CB-MOF-1 (blue) at room temperature.

Further test for water stability has been done by boiling the as-made *anti-o*CB-MOF-1 in water for 30 minutes, followed by re-addition of DMF to investigate the reversibility of the material. Figure 3.5-15 shows the PXRD of as-made *anti-o*CB-MOF-1 (black), boiling water treated *anti-o*CB-MOF-1 (red), re-addition of DMF for 15h (green) and for 3 days (blue) to the boiling water treated *anti-o*CB-MOF-1. In this case, a new peak appears at higher angle after boiling water treatment, and addition of DMF can only partially reverse the structure to the original one. This indicates that the *anti-o*CB-MOF-1 is only partially stable in boiling water.
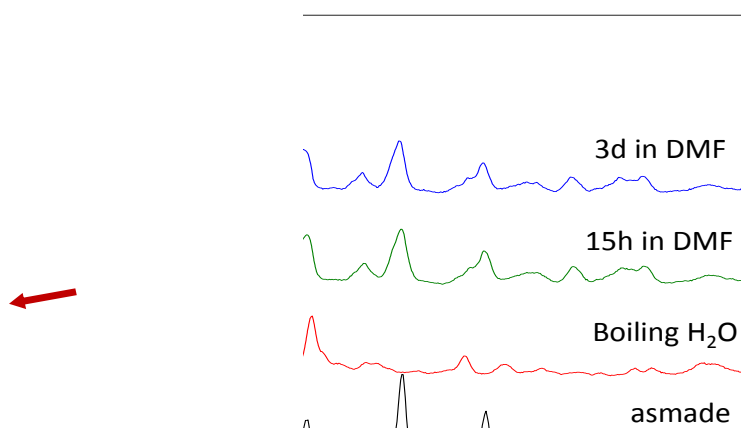

Figure 3.5-15: PXRD of as-made *anti-o*CB-MOF-1 (black), boiling water treated *anti-o*CB-MOF-1 (red) and the re-addition of DMF to the water treated *anti-o*CB-MOF-1for 15h (green) and for 3 days (blue).

In addition, different solvents (methanol, acetone and CHCl$_3$) have been introduced in order to study the influence of solvents towards the *anti-oCB-MOF-1* structure. As shown in Figure 3.5-16, compare to the as-made *anti-oCB-MOF-1* (black), the CHCl$_3$ treated *anti-oCB-MOF-1* remains unchanged because of the low polarity of CHCl$_3$. However, a slight shift of the PXRD pattern is observed for the acetone treated sample. A bigger shift of the PXRD pattern is observed for the methanol treated sample, similar to the one observed for the water treated PXRD of *anti-oCB-MOF-1* (Figure 3.5-14). This may due to the possible formation of the hydrogen bonding between the additional protic solvents (in this case methanol) and the DMF solvents in the pore and/or with the surface of the materials.

methanol

acetone

CHCl$_3$

asmade

Figure 3.5-16: PXRD of as-made *anti-oCB-MOF-1* (black), CHCl$_3$ treated *anti-oCB-MOF-1* (blue), acetone treated *anti-oCB-MOF-1* (green) and methanol treated *anti-oCB-MOF-1* (red).

pH 12

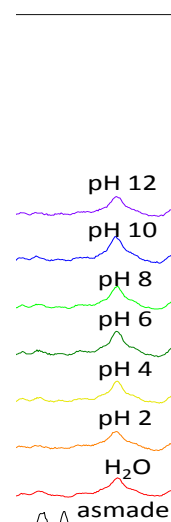pH 10

pH 8

pH 6

pH 4

pH 2

H$_2$O

asmade

Figure 3.5-17: PXRD of as-made (black), water treated (red), pH 2 treated (orange), pH 4 treated (yellow), pH 6 treated (green), pH 8 treated (light green), pH 10 treated (blue) and pH 12 treated (purple) *anti-oCB-MOF-1*.

Furthermore, preliminary result of the stability in acidic solution (dilute HCl) and basic solution (dilute NaOH) have been performed and the results are summarized in Figure 3.5-17. The pH solutions were calibrated by pH meter, followed by immersing the *anti-o*CB-MOF-1 powder into the corresponding pH solutions for 15h. The *anti-o*CB-MOF-1 is unstable in pH 0 and pH 14 solutions as the samples are totally dissolved. However, *anti-o*CB-MOF-1 is stable in solution between pH 2 to 12 solutions as the structures are maintained.

By introducing carborane-based ligand for MOF syntheses can significantly enhance the water stability of MOF due to the presence of hydrophobic character of carborane clusters. Additional stability towards acidic and basic conditions (pH 2 – 12) of *anti-o*CB-MOF-1 has been observed as well. The water stability and the extra acidic and basic stability of *anti-o*CB-MOF-1 can be achieved not only because of the presence of the hydrophobic carborane clusters, but also the location of the *anti-o*CB-(L2)₂ ligands, which coordinate around the tetra-nuclear zinc clusters, providing extra protection from the attack of water, acid or base to the zinc ions (Figure 3.5-18). These extraordinary results open a new route by introducing carborane for material development that requires stability towards aqueous conditions.
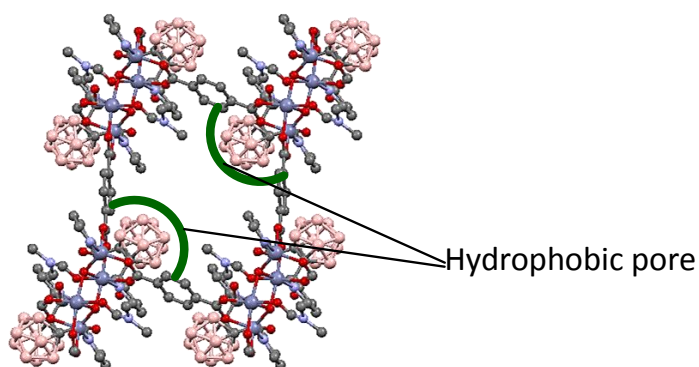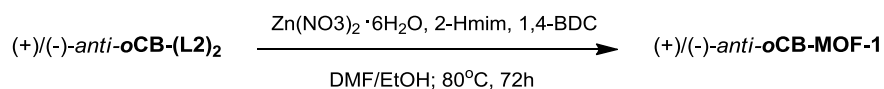

Figure 3.5-18: image of the accessible pore of *anti-o*CB-MOF-1 and the indication of the hydrophobic pore.

3.5.1.4 Formation of enantiopure *anti-o*CB-MOF-1 and meso *syn-o*CB-MOF-1 isomer

As mentioned previously (Chapter 3.1.1), the disubstituted ligands *o*CB-(L2)₂ contain *syn-* and *anti-*isomers. All the ligands contain two chiral carbon centres that can adopt the *R* or *S* configuration, therefore the two diastereoisomers: meso compound (*RS*; OH groups in a *syn-*orientation; non chiral) and racemic compound (mixture of *SS* and *RR*; OH groups in an *anti-*orientation, chiral). A recent report shows the influence of enantiopure ligand and the racemic ligand towards the formation of MOFs, in which different architectures can be obtained by applying racemic ligand or enantiopure ligand.[12] The *anti-o*CB-MOF-1 described above has been synthesized by using the racemic *anti-o*CB-(L2)₂ ligand. It is interesting to study the possible influence of racemic versus enantiopure *anti-o*CB-(L2)₂ ligand in this carborane-based MOF system as well as the influence of using the meso (non-chiral) *syn-o*CB-(L2)₂ ligand. In order to investigate whether the chirality affects the formation of *anti-o*CB-MOF-1, the enantiopure ligands of *anti-o*CB-(L2)₂ were separated by chiral column (Chiralcel OD-3) with hexane/ethanol (8:2) as eluent. The obtained (+)-*anti-o*CB-(L2)₂ and

(-)-*anti*-*o*CB-(L2)$_2$ were then used to synthesize the corresponding enantiopure MOF (+)-*anti*-*o*CB-MOF-1 and (-)-*anti*-*o*CB-MOF-1 by slight modification of solvothermal condition (Scheme 3.5-2). In addition, the syn-*o*CB-(L2)$_2$ was also applied for the MOF synthesis by following the same procedure to study whether there is any influence of the isomers for MOF construction.

Scheme 3.5-2: synthetic condition of (+)/(-)-*anti*-*o*CB-(L2)$_2$.

$$(+)/(-)\text{-}anti\text{-}o\textbf{CB-(L2)}_2 \xrightarrow[\text{DMF/EtOH; 80}^{\circ}\text{C, 72h}]{\text{Zn(NO3)}_2 \cdot 6\text{H}_2\text{O, 2-Hmim, 1,4-BDC}} (+)/(-)\text{-}anti\text{-}o\textbf{CB-MOF-1}$$

The formation of the three new MOFs, *syn*-*o*CB-MOF-1, (+)-*anti*-*o*CB-MOF-1 and (-)-*anti*-*o*CB-MOF-1 have been confirmed by FTIR-ATR and PXRD. The resulting PXRD patterns are all the same as *rac*-*anti*-*o*CB-MOF-1, indicating that the diastereoisomer or the chirality of the *o*CB-(L2)$_2$ ligand does not affect the MOF construction (Figure 3.5-19B).

A
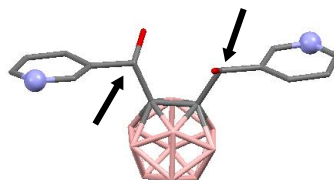
B

Figure 3.5-19A: coordination mode of *anti*-*o*CB-(L2)$_2$ in the structure of *anti*-*o*CB-MOF-1, the chiral carbon centers are pointed by black arrows. B: PXRD of *syn*-*o*CB-MOF-1 (green), rac-*anti*-*o*CB-MOF-1 (black), (+)-*anti*-*o*CB-MOF-1 (red) and (-)-*anti*-*o*CB-MOF-1 (blue).

The coordination mode of ligand *anti*-*o*CB-(L2)$_2$ is illustrated in Figure 3.5-19A which is extracted from the structure of racemic *anti*-*o*CB-MOF-1. Due to the rotational flexibility of the pyridine rings, the chirality of the carbon centres do not affect the pyridine ring coordination, so that there is no influence of the position of the alcohol groups towards the formation of *o*CB-MOF-1 in this system.

This is in contrast with the above mentioned report[12] where the chiral groups of the organic ligands employed are directly bonded to the metal atoms and are therefore affecting the MOF structure.

The successful synthesis by mixed-ligand approach with carboxylic acid (1,4-BDC) and the **oCB-(L2)₂** linker, has result in a unique 3D porous skeleton with unusual zinc clusters units. Also, the hydrophobic feature of the pores, induced by the carborane clusters, gives rise to high CH_4 affinity and significant enhancement of the water stability. The successful synthetic methodology opened a new path to develop potential materials for application by various combination of carboxylic acids and this family of carborane-based ligands **CB-(L)₂**. To further explore the possibility to introduce **CB-(L)₂** in the MOF systems, in the following section, *meta*-carborane-based pyridylalcohol ligands **mCB-(L2)₂** and **mCB-(L3)₂** will be introduced for the mixed-ligand MOF syntheses.

3.5.2 *meta*-Carborane-Based Mixed Ligand MOFs

3.5.2.1 Co/BDC MOFs: Influence of *meta*-carborane-based 3- and 4-Pyridylalcohol Linkers

As previously explained (Chapter 3.1.1), the flexibility of the *meta*-carborane-based ligand **mCB-(L2)₂** and **mCB-(L3)₂** are higher than those for the related *ortho*-carborane derivatives. The same synthetic methodology as **oCB-MOF-1** is applied for the *meta*-carborane-based MOF series.

$Co(NO_3)_2 \cdot 6H_2O$, **mCB-(L2)₂** and 1,4-BDC (3:1:3 ratio) were mixed in a capped vial with DMF/ethanol (1:1) solvent mixture (Scheme 3.5-3) for 48h at 85°C. Violet flake liked crystalline solid **mCB-MOF-2** has been obtained in high yield (68.5 %).

Scheme 3.5-3: Synthetic scheme of **mCB-MOF-2**
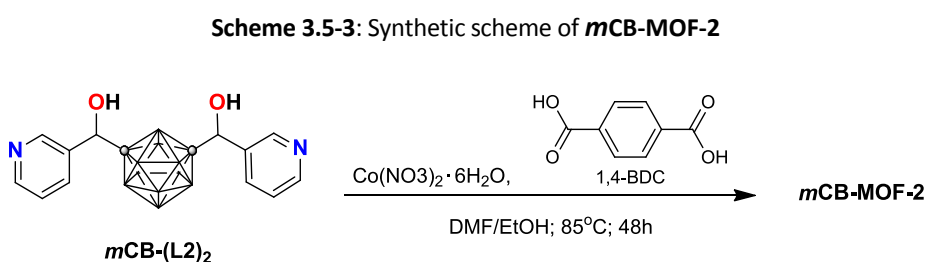
The MOF **mCB-MOF-2** is fully characterized by FTIR-ATR, PXRD and SEM. The structure is confirmed by synchrotron single-crystal XRD. **mCB-MOF-2** shows a 3D structure that is built on tri-nulcear Co clusters $[Co_3O_2(COO)_6N_2]$ secondary building unit (SBU). Figure 3.5-20A illustrates the coordination environment of the Co atoms. The SBU contains a linear array of three Co atoms, all showing an octahedral coordination. Each trinuclear SBU is then connected to six BDC units to form a 2D layer (Figure 3.5-20B). Hence, this 2D layer is pillared by **mCB-(L2)₂** giving rise to the observed 3D framework (Figure 3.5-20C and D).
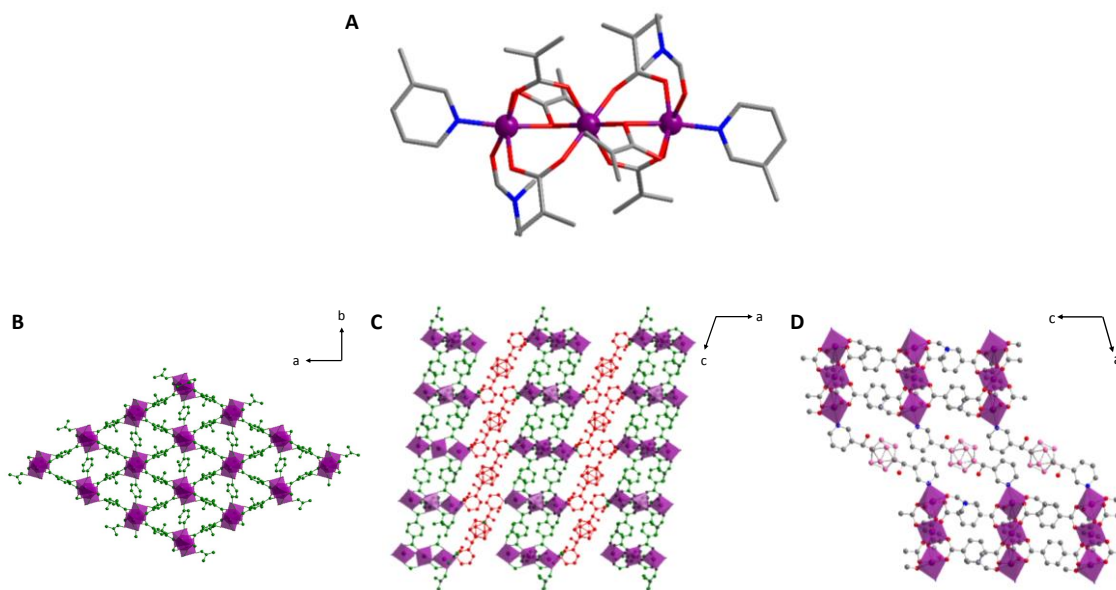
Figure 3.5-20: Structure of *m*CB-MOF-2. A: The trinuclear Co clusters. B:2D-Co(II)-based layer. C: 3D Co(II) framework by *m*CB-(L2)₂ bridging linkers. D: 3D network, in which the carborane ligands act as pillars.

The new pillared *m*CB-MOF-2 is densely pack and giving a calculated void volume only around 13% of its unit cell. In Figure 3.5-21A, A schematic representation of *m*CB-MOF-2 is shown, illustrating the coordination of the *m*CB-(L2)₂ bridging linkers. It is reasoned by using 4-pyridylalohol ligand *m*CB-(L3)₂, a related pillared MOF but with increased porosity is expected to obtain (Figure 3.5-21B).
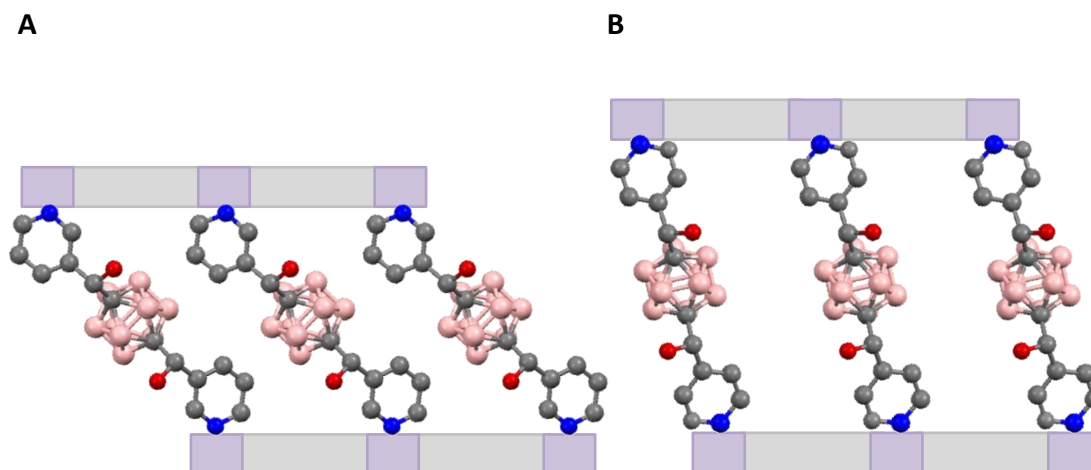

Figure 3.5-21: Illustration of the influence of pyridine position towards the pore size/shape. A: 3-pyridine in *m*CB-MOF-2; B: 4-pyridine in *m*CB-MOF-2B

By following the same synthetic procedure as in *m*CB-MOF-2, a similar violet crystalline solid *m*CB-MOF-2B has been obtained and characterized by FTIR-ATR, SEM and PXRD. As shown in the SEM images in Figure 3.5-22, for both *m*CB-MOF-2 and *m*CB-MOF-2B, flake liked single crystals are formed, which indicate similar crystal morphologies in both structures.
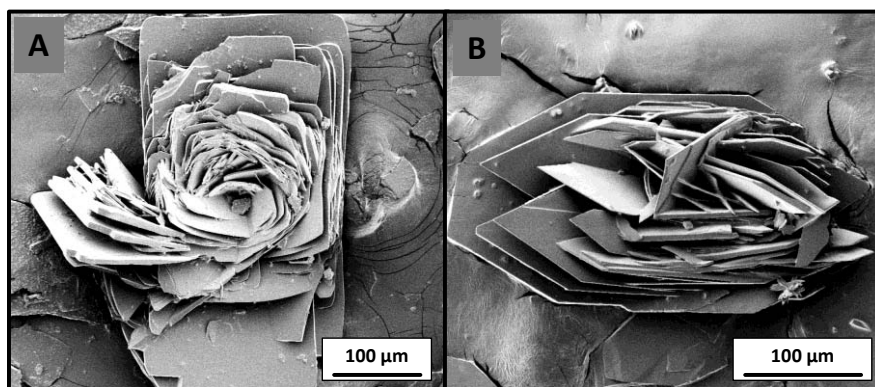
Figure 3.5-22: SEM images of the (A) as-made *m*CB-MOF-2 in 100 µm and (B) as-made *m*CB-MOF-2B in 100 µm.

A comparison of experimental PXRD patterns for *m*CB-MOF-2 and *m*CB-MOF-2B and the calculated one from the former is shown in Figure 3.5-23. The phase purity of bulk *m*CB-MOF-2 is proven by comparison of the experimental PXRD (blue) with the calculated from the X-ray structure (black). Since the crystal structure of *m*CB-MOF-2B could not be solved by single-crystal XRD, its PXRD (Figure 3.5-23, red) was compared to *m*CB-MOF-2. As it can be seen in the Figure, the PXRD pattern of *m*CB-MOF-2B is very similar to that of *m*CB-MOF-2. It is important to note that the peak at around 4° (highlighted in green) shows lower angle than the one from *m*CB-MOF-2 (c.a. 5°). Since the scattering angle 2θ of PXRD is a reflection of the unit cell of the materials, thus, lower angle indicates the presence of larger spacing.
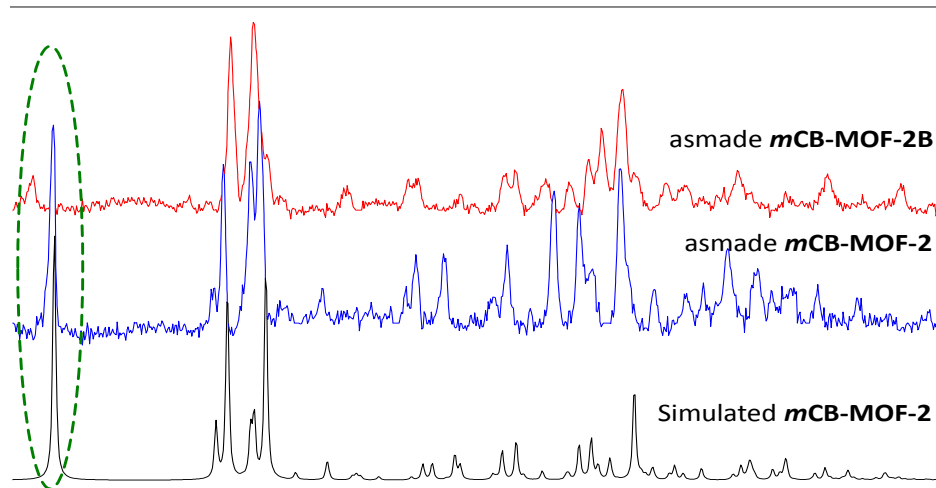

Figure 3.5-23: PXRD of as-made *m*CB-MOF-2B (red), as-made *m*CB-MOF-2 (blue)
and simulated *m*CB-MOF-2 (black).

Le Bail fit with Pawley method was applied to estimate the unit cell of *m*CB-MOF-2B, assuming that it crystallized in the same space group as *m*CB-MOF-2. As shown in Table 3.5-1, the estimated unit cell of *m*CB-MOF-2B has similar dimension in β angle and *b* and *c* axes as *m*CB-MOF-2, but in *a* axis, *m*CB-MOF-2B is about 2 Å larger than *m*CB-MOF-2. This result fit to the hypothesis (illustrated in

Figure 3.5-21) that the accessible pore size can be increased as expected by replacing **_m_CB-(L3)₂** as pillar ligand to connect the cobalt cluster layers.

Table 3.5-1: Space groups and Lattice parameters comparison of refined **_m_CB-MOF-2** and La Bail fit by Pawley method of **_m_CB-MOF-2B**.

|	**_m_CB-MOF-2**	**_m_CB-MOF-2B**
Space group	C2/c	C2/c
Lattice parameters		
a (Å)	35.1297198	37.9073841
b (Å)	9.6852316	9.0666823
c(Å)	18.1992216	17.4203574
β(°)	96.69028	95.13517

The preliminary results show that by replacing the pillar linker from **_m_CB-(L2)₂** to **_m_CB-(L3)₂** can increase the size of the unit cell, implying a possible magnification of the pore size or shape of the corresponding MOF. More studies on both **_m_CB-MOF-2** and **_m_CB-MOF-2B** are still on-going. BET surface areas are crucial in order to prove the sorption enhancement by increasing the accessible pore size/shape with **_m_CB-(L3)₂** in comparison with **_m_CB-(L2)₂**.

3.5.2.2   M (Zn, Co)/LCOOH (BTB, TCPB) MOFs: Impact of _m_CB-(L2)₂ and _m_CB-(L3)₂ Linkers

As mentioned previously, the flexibility of the _meta_-carborane-based ligand provides various possibilities to form different motifs. In order to study the influence of different parameters to the MOFs formation, in the following part, syntheses of caborane-based MOFs by changing the carboxylic acid to 1,3,5-tris(carboxylphenyl)benzene (BTB) and 1,2,4,5-tetrakis(4-carboxyphenyl) benzene (TCPB) will be discussed.

_m_CB-MOF-3 is formed by mixing Zn(NO₃)₂·6H₂O, **_m_CB-(L3)₂** and BTB in the optimized ratio (4:1:2) in a capped vial with DMF/ethanol/H₂O (2:1:1) solvent mixture (Scheme 3.5-4) for 48h at 85 °C. Transparent square crystals **_m_CB-MOF-3** has been obtained in high yield (c.a. 90 %).

Scheme 3.5-4: Synthetic scheme of **_m_CB-MOF-3**
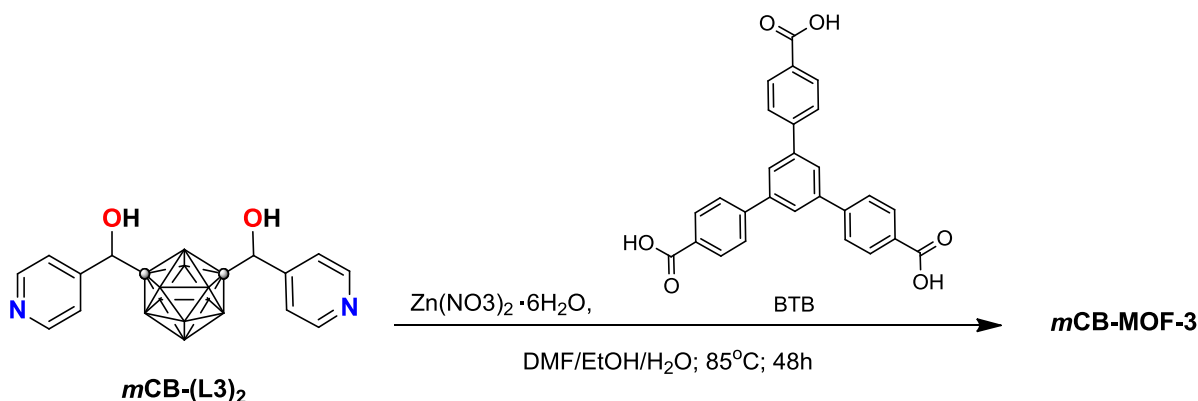
Several trials were done in order to replace zinc by Cobalt in **mCB-MOF-3**, however, the obtained crystals were of low quality for XRD measurement.

The structure is confirmed by single-crystal XRD (Figure 3.5-24). As shown in Figure 3.5-24A, tetra-nuclear zinc clusters are formed in two different coordination modes: tetrahedral (highlighted in green) and octahedral (highlighted in black). The honeycomb like channels are formed with BTB (Figure 3.5-24B) and the **mCB-(L3)₂** ligands are connected within the channel between two zinc clusters as shown in Figure 3.5-24C and resulting in hemisphere channels in **mCB-MOF-3** (Figure 3.5-24D).
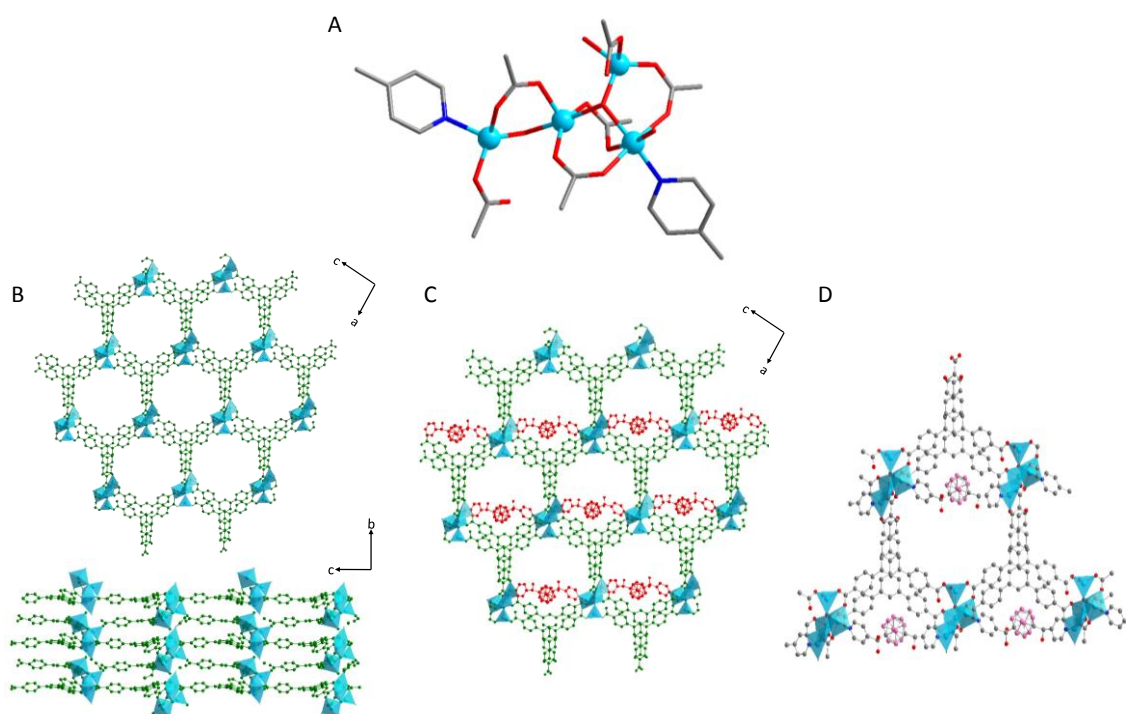

Figure 3.5-24: The tructure of **mCB-MOF-3**: A: tetranuclear Zn (II) clusters; B: formation of hexagonal void with BTB by stacking; C: coordination of **mCB-(L3)₂** in the hexagonal void; D: close-up of one of the accessible pores.

When the tetra-carboxylic acid TCPB was used instead of tricarboxylic acid BTB, **mCB-MOF-4** is formed. Following the same procedure, **mCB-MOF-4** was synthesized by mixing $Zn(NO_3)_2 \cdot 6H_2O$, **mCB-(L3)₂** and TCPB in the optimized ratio (2:1:1) in a capped vial with $DMF/ethanol/H_2O$ (2:1:1) solvent mixture (Scheme 3.5-5) for 72h at $80^{\circ}C$. **mCB-MOF-4** was obtained as transparent rectangular crystals.

Scheme 3.5-5: Synthetic scheme of *m*CB-MOF-4
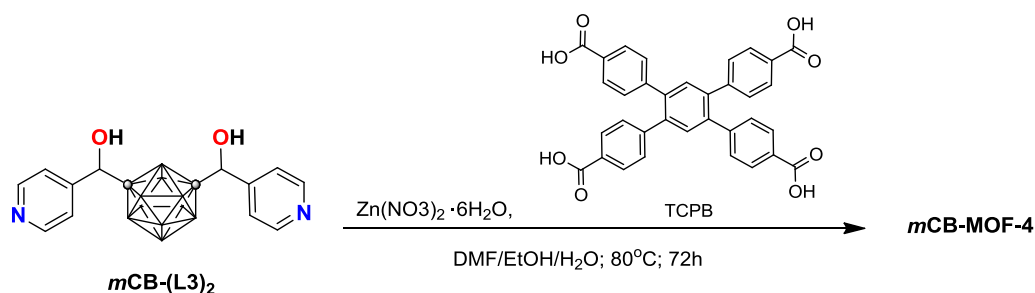
The structure for *m*CB-MOF-4 is confirmed by single-crystal XRD (Figure 3.5-25). Different to the above MOFs, the structure for *m*CB-MOF-4 is composed of typical dinuclear zinc unit [Zn$_2$(COO)$_4$] (Figure 3.5-25A), which are connected by the TCPB ligands to form a 2D framework (Figure 3.5-25B). This framework is further bridged by the ditopic *m*CB-(L3)$_2$ ligands at 180° via their nitrogen atoms, resulting in a 3D framework (Figure 3.5-25C). Interpenetration of the 3D networks occur and resulting in the formation of *m*CB-MOF-4 (Figure 3.5-25D).
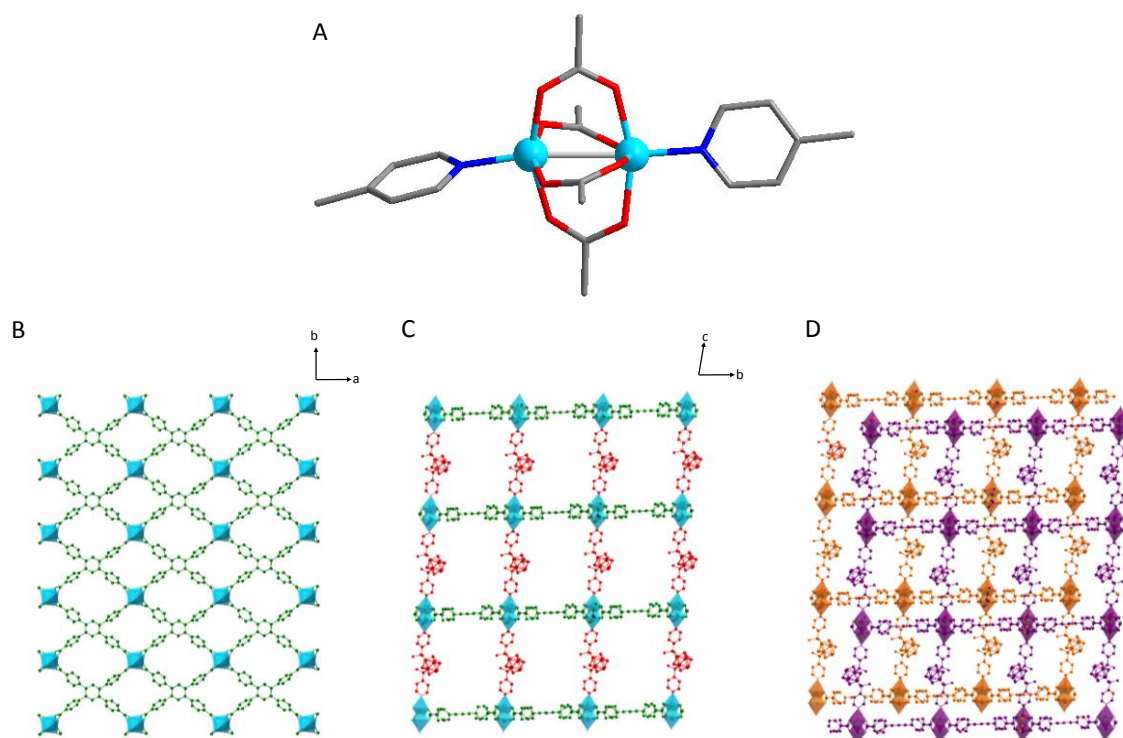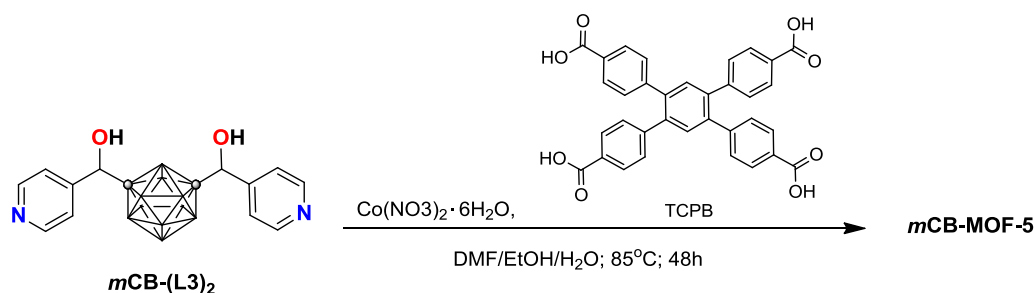

Figure 3.5-25: The structure of *m*CB-MOF-4: A: dinuclear Zn (II) clusters; B: formation of 2D layers with TCPB; C: *m*CB-(L3)$_2$ act as pillar linkers to connect the 2D layers to form a 3D cubic networks; D: Interpenetration of the 3D networks.

Next, cobalt was used instead of zinc with the carboxylic acid TCPB and *m*CB-(L3)$_2$. In this case, Co(NO$_3$)$_2$·6H$_2$O, *m*CB-(L3)$_2$ and TCPB in the optimized ratio (2:1:1) were mixed in a capped vial with DMF/ethanol/H$_2$O (2:1:1) solvent mixture (Scheme 3.5-6) for 48h at 85 ^{o}C and resulting in pink needle liked crystals *m*CB-MOF-5.

Scheme 3.5-6: Synthetic scheme of *m*CB-MOF-5

The structure of *m*CB-MOF-5 has been solved by single-crystal XRD which exhibits a 3D framework based on a dinuclear Co^{2+} cluster (Figure 3.5-26A). Two Co^{2+} sites are bridged by two TCPB carboxylates and by an oxygen atom. The coordination sphere at each six-coordinate cobalt site is completed by two monodentate TCPB carboxylate, one water molecule and one DMF molecule. The cobalt clusters are connected by TCPB to form 2D layers (Figure 3.5-26B) and the *m*CB-(L3)$_2$ link to the clusters through TCPB in a zig-zag style (Figure 3.5-26C). These 2D layers are stacked together along the *c* axis by hydrogen bonding between the alcohol groups of *m*CB-(L3)$_2$ ligands to form 3D networks (Figure 3.5-26D).
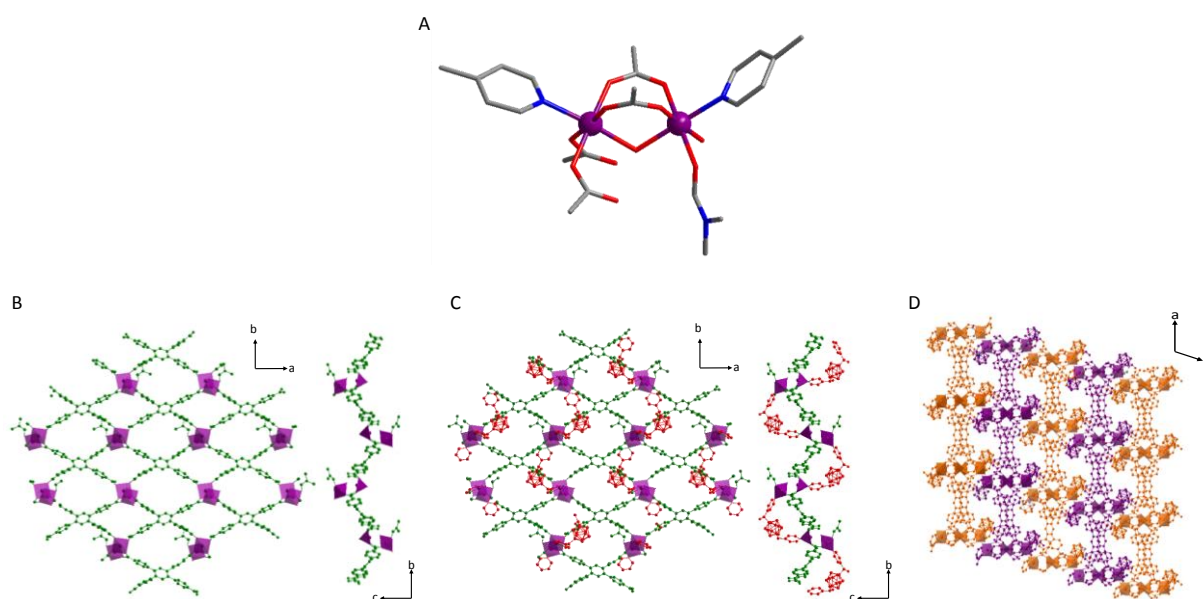

Figure 3.5-26: The structure of *m*CB-MOF-5: A: dinuclear Co (II) clusters; B: formation of 2D layers with TCPB; C: *m*CB-(L3)$_2$ ligands link to the cobalt clusters in zig-zag style; D: 2D layers stack together by hydrogen bonding to form 3D networks.

Conclusively, three new MOFs have been synthesized and fully characterized by FTIR-ATR, PXRD, SEM, elemental analysis and single-crystal XRD. By changing the carboxylic acid from BTB to TCPB, very different motifs of the MOF can be obtained, which is not only the result of the highly flexible feature of the *meta*-carborane-based ligand *m*CB-(L3)$_2$, but also a certain degree of influence may exist from the three dimensional bulkiness of the carborane clusters. Besides, the use of transition metals

(cobalt, zinc) also gives rise to inevitable impact to the formation of carborane-based MOFs due to the different reactivity and final metal clusters formed. Detail studies on the influence of various parameters are still undergone in order to understand the formation mechanism, as well as the water stability tests, and therefore could design a desire water stable MOFs with high gases capacity and/or selectivity.

3.5.2.3 Incorporation of Carborane-Based Linkers: Unique Architecture versus Water Stability

Compared to conventional MOFs with aromatic linkers,[13] introduction of *ortho-* and *meta*-carborane based pyridylalcohol ligands *o*CB-(L2)$_2$, *m*CB-(L2)$_2$ and *m*CB-(L3)$_2$ in the mixed-ligand syntheses results in unique architectures with uncommon metal ion clusters. This is for example the case of *o*CB-MOF-1, *m*CB-MOF-3 and *m*CB-MOF-5. But common architectures are also found in some of the carborane ligands, such as in *m*CB-MOF-2 and *m*CB-MOF-4, where they are acting as pillared ligands. These results clearly show the versatility of these new disubstituted ligands for the construction of MOFs without restriction from the rigidity of the ditopic ligands. As an example, the coordination motifs of *m*CB-(L3)$_2$ extracted from the three of the new *m*CB-MOF structures are shown in Figure 3.5-27.
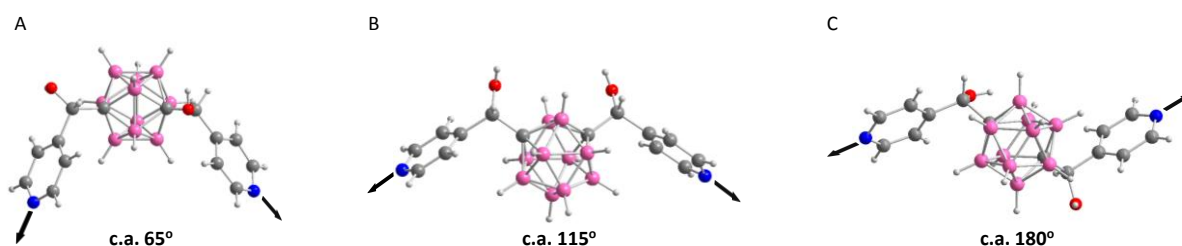

Figure 3.5-27: coordinating angles of ligand *m*CB-(L3)$_2$ from A: *m*CB-MOF-5, B: *m*CB-MOF-3 and C: *m*CB-MOF-4 structures.

The complete study on *o*CB-MOF-1 shows high thermodynamic water stability (Section 3.5.1.3). The preliminary results show that *m*CB-MOF-3 is stable in bulk water as well (Figure 3.5-28B). However, in the case of *m*CB-MOF-2, the MOF is destroyed after water treatment (Figure 3.5-28A).
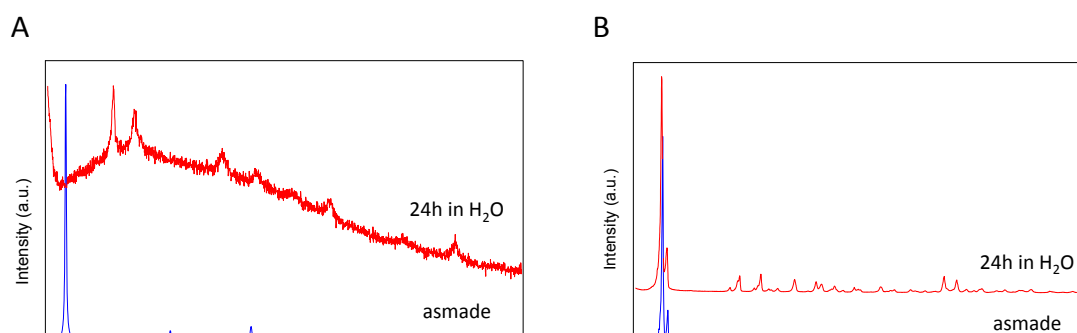

Figure3.5-28: PXRD before (bottom) and after (top) water treatment of A: *m*CB-MOF-2 and B: *m*CB-MOF-3.

As explained earlier (Chapter 1.3.2), the water molecules can attack the metal clusters and replace the coordinated ligands, resulting in the structure of the MOFs collapse in humid environment. The incorporation of the flexible carborane-based pyridylalcohol ligands presumably can enhance the stability towards humid conditions or even in bulk water due to the hydrophobic character of carborane clusters. However, such stability also depends on the construction of the ligands around the metal ion clusters. The preliminary results of these carborane-based MOFs show that the water stability does not fully rely on the introduction of these ligands **CB-(L)₂**, but rather *how* the **CB-(L)₂** coordinate around the metal clusters, in which creates a hydrophobic environment around the metal clusters that prevent the attack from water molecules. The MOFs *o***CB-MOF-1** and *m***CB-MOF-3** contain protected zinc clusters that surrounded by hydrophobic carborane clusters and/or the aromatic groups from the carboxylic acid, thus, water molecules are repelled to access to the metal centres and resulting in high water stability. However, the cobalt clusters in *m***CB-MOF-2** have coordinated DMF molecules that expose to the pores and generate polar surroundings. Also, the cobalt clusters are not protected by carborane moieties, therefore, immersion of *m***CB-MOF-2** into bulk water possibly resulting in migration of water molecules towards the cobalt clusters and disassociate the ligands from the clusters. The water stability of *m***CB-MOF-4** and *m***CB-MOF-5** are still under investigations, although structure collapse may occur due to the polar environments of the surroundings and the unprotected metal clusters that may be accessible by water.

Combination of these flexible **CB-(L)₂** ligands with carboxylic acids for MOF syntheses can induce the formation of unique architectures under certain circumstances and independently giving water stable properties according to the hydrophobicity of the metal cluster surroundings that *how* the carborane ligands locate. The studies on water stabilities of these MOF systems are still on-going. The incorporation of **CB-(L)₂** ligands in the mixed-ligand approach undoubtedly gives rise to unique motifs with high water stabilities in some occasions. The flexibility and hydrophobicity of these **CB-(L)₂** ligands definitely are potential candidates to develop new types of MOFs. Detail investigations are currently continued in order to understand the dominant factors and the formation mechanism which will be the key to design the desired water resistant MOFs with this carborane-based system for different applications.

References

[1]   (a) Y-S. Bae, K. L. Mulfort, H. Frost, P. Ryan, S. Punnathanam, L. J. Broadbelt, J. T. Hupp, R. Q. Snurr, *Langmuir*, **2008**, *24*, 8592. (b) H. J. Park, M. P. Suh, *Chem. Eur. J.*, **2008**, *14*, 8812. (c) A. D. Burrows, *CrystEngComm*, **2011**, *13*, 3623. (d) P. Deria, J. E. Mondloch, O. Karagiaridi, W. Bury, J. T. Hupp, O. K. Farha, *Chem. Soc. Rev.*, **2014**, *43*, 5896.

[2]   (a) H. Li, M. Eddaoudi, M. O'Keeffe, O. M. Yaghi, *Nature*, **1999**, *402*, 276. (b) D. J. Tranchemontagne, J. R. Hunt, O. M. Yaghi, *Tetrahedron*, **2008**, *64*, 8553.

[3]   (a) J. A. Greathouse, M. D. Allendorf, *JACS*, **2006**, *128*, 10678. (b) M. D. Toni, R. Jobchiere, P. Pullumbi, F-X. Coudert, A. H. Fuchs, *ChemPhysChem*, **2012**, *13*, 3497.

[4]   (a) J. Cravillon, S. Munzer, S-J. Lohmeier, A. Feldhoff, K. Huber, M. Wiebcke, *Chem. Mater.*, **2009**, *21*, 1410. (b) J. Cravillon, R. Nayuk, S. Springer, A. Feldhoff, K. Huber, M. Wiebcke, *Chem. Mater.*, **2011**, *23*, 2130.

[5]   a) D. W. Breck, *Zeolite Molecular Sieves: Structure, Chemistry and Use*. John Wiley & Sons, Inc.: New York, 1974. b) N. Mehio, S. Dai, D. Jiang, *J. Phys. Chem. A* **2014,** *118*, 1150-1154

[6]   J. R. Li, R. J. Kuppler, H-C. Zhou, *Chem. Soc. Rev.*, **2009**, *38*, 1477.

[7]   R. K. Vyas, S & S Kumar, *Indian J. Chem. Technol.*, **2004**, *11*, 704.

[8]   Y. He, W. Zhou, G. Qian, B. Chen, *Chem. Soc. Rev.*, **2014**, *43*, 5657.

[9]   K. Sumida, D. L. Rogow, J. A. Mason, T. M. McDonald, E. D. Bloch, Z. R. Herm, T-H. Bae, J. R. Long, *Chem. Rev.*, **2012**, *112*, 724.

10]   N. C. Burtch, H. Jasuja, K. S. Walton, Chem. Rev., 2014, 114, 10575

[11] J. Canivet, J. Bonnefoy, C. Daniel, A. Legrand, B. Coasne, D. Farrusseng, *New. J. Chem.*, **2014**, *38*, 3102.

[12] I. Burneo, K. C. Stylianou, I. Imaz, D. Maspoch, *Chem. Commun.*, **2014**, *50*, 13829.

[13] (a) N. Klein, I. Senkovska, I. A. Baburin, R. Grunker, U. Stoeck, M. Schlichtenmayer, B. Streppel, U. Mueller, S. Leoni, M. Hirscher, S. Kaskel., *Chem. Eur. J.*, **2011**, *17*, 13007. (b) D. Han, F-L. Jiang, M-Y. Wu, L. Chen, Q-H. Chen, M-C. Hong, *Chem. Commun.*, **2011**, *47*, 9861. (c) A. D. Burrows, L. C. Fisher, D. Hodgson, M. F. Mahon, N. F. Cessford, T. Duren, C. Richardson, S. P. Rigby, *CrystEngComm*, **2012**, *14*, 188.